Scattering of Alpha Particles*

R. M. EISBERG

School of Physics, University of Minnesota, Minneapolis 14, Minnesota

AND

C. E. PORTER

Brookhaven National Laboratory, Upton, New York

CONTENTS

I. INTRODUCTION

INVESTIGATION of the scattering of alpha particles was a very active and important field of research in the early years of this century. In fact, the experiments on alpha-particle scattering by Geiger and Marsden and and their interpretation by Rutherford actually constituted the discovery of the nucleus. After about 1935 this subject was essentially dormant, but within the past few years it has become active again. This article describes briefly the early work and then discusses in more detail the modern developments.

The motivation of research in this field has been to use the scattering of alpha particles as a probe to measure the strength and spatial extent of the interaction potential between the alpha particle and the nucleus. Quantitative information about the potential has been obtained by interpreting the recent experimental data in terms of an optical model which expresses the interaction between the alpha particle and the nucleus as a complex potential with a diffuse edge. However, an adequate theoretical interpretation came only after a succession of interesting, but much cruder, optical models had been considered at various stages while the data were being accumulated.

Here the modern experimental data are summarized, descriptions are given of the several optical models which have been used to interpret the data, the predictions of these models are compared with the experiments and the models are compared. In order to bring out the interplay which took place in the experimental and theoretical developments of this field, these developments are presented in approximately chronological order. The theoretical discussion includes both the elastic scattering and total reaction cross sections. Although almost no data currently exist on the latter, the cross sections for both these entrance channel phenomena can be predicted from the optical model.

II. EARLY EXPERIMENTAL AND THEORETICAL WORK

Geiger and Marsden were investigating the scattering of low-energy (4 to 8 Mev) alpha particles, obtained from radioactive sources, by thin foils of various elements (17).[1] They observed multiple small angle scattering, a phenomenon which could be understood on the basis of the then current theories of atomic structure (54); however, they also observed an occasional scattering at large angles. In order to explain this large angle scattering, Rutherford found he had to assume that all the positive (or negative) charge of the atom was concentrated in a small region at the center (47). Providing that the hyperbolic trajectory of the scattered alpha particle does not pass through the nuclear region, so that the alpha particle is acted upon by a Coulomb force at all times, Rutherford showed that the cross section for the elastic scattering of alpha particles is

$$d\sigma_c/d\Omega = (Z'Ze^2/4E)^2[1/\sin^4(\theta/2)],$$

where $Z'e$ and Ze are the charge of the incident alpha particle and the target nucleus, E is the kinetic energy of the alpha particle, and θ is its scattering angle. It is assumed that the nucleus remains at rest during the

* This work supported in part by the U. S. Atomic Energy Commission.

[1] References in parentheses are given in numerical order in the Bibliography.

collision. This formula describes what is called Coulomb scattering. It has been experimentally verified for a wide range of elements, energies, and scattering angles (18).

In applying Rutherford's model to the scattering of alpha particles by light nuclei, it is necessary to take into account the recoil of the nucleus (8). But even after this correction was made, serious disagreements were found when the predicted Coulomb cross sections were compared to the experimental cross sections for the scattering of alpha particles by hydrogen (48). Departures from Coulomb scattering were also found in the scattering of alpha particles from He (49) and in the scattering at large angles from Mg and Al (2). These departures were interpreted as a result of penetration of the alpha-particle trajectory into the nuclear region, resulting in a departure from the Coulomb force. Penetration of the nuclear region becomes significant only when the scattering of the low-energy alpha particles used in these experiments takes place from light elements in which the Coulomb repulsion is weak due to the small nuclear charge.

By using the formulas appropriate to Coulomb scattering, Rutherford calculated the distance from the center of the nucleus to the point of nearest approach to the trajectory under the various experimental conditions. From this he was able to estimate the radius of the nuclear region. He found that whenever the Coulomb scattering formula was obeyed, the distance of nearest approach—called the apsidal distance—was greater than about 10^{-12} cm (47). For smaller apsidal distances, departures from Coulomb scattering were observed. The obvious implication is that the radius of the nuclear region is about 10^{-12} cm.

An attempt was made by Hardmeier to interpret the experimental data on the scattering from Mg and Al (24). He assumed that the alpha particle induces an electric dipole moment in the nucleus of magnitude:

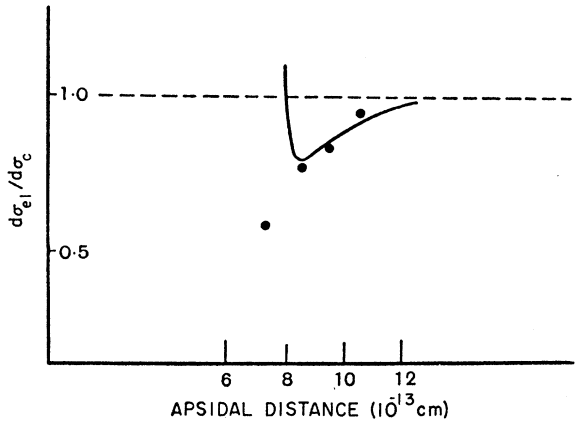

FIG. 1. Typical early data showing departures from pure Coulomb scattering. Points give the ratio of the observed cross section to the Coulomb cross section for the 90° scattering from Al of alpha particles from several radioactive sources plotted as a function of apsidal distance. The solid curve shows the result of the polarization theory of Hardmeier.

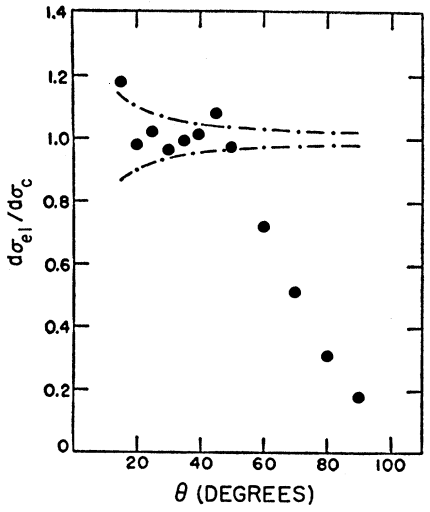

FIG. 2. Experimental data for elastic scattering of 27.5-Mev alpha particles by Au. Dashed lines indicate limits within which pure Coulomb scattering points would fall based on experimental uncertainty of ±0.5° in angular measurements.

$P=a(Z'e/r^2)$, where r is the distance from the center of the nucleus to the alpha particle and $Z'e$ is the charge of the alpha particle. The induced dipole moment contributes to the potential acting on the alpha particle an attractive term proportional to r^{-4}. This term dominates the r^{-1} Coulomb repulsion at small distances but is negligible at large distances. Approximate agreement between the predictions of this model and the data for the scattering of relatively low-energy alpha particles by Mg and Al was achieved when the polarizability a was given the value $a\simeq 0.4\times 10^{-36}$ cm^3; however, this model was not able to explain the scattering of higher-energy alpha particles from Mg and Al, nor could it explain any of the results observed in the scattering of alpha particles from H or He. Figure 1 presents some typical early data showing departures from Coulomb scattering. The points give the ratio of the observed cross section to the Coulomb cross section for the 90° scattering from Al of alpha particles from several radioactive sources. The data are plotted as a function of the apsidal distance. The solid curve is the result of the calculation of Hardmeier.

A summary written by Pollard (42) in 1935 shows that by that time data existed on the elastic scattering of alpha particles from most of the light elements through Al. In each case departures from Coulomb scattering were observed. By making the assumption that the onset of the departure from Coulomb scattering takes place when the probability of barrier penetration for S-wave alpha particles equals 10%, Pollard was able to use these data to make quantitative estimates of the nuclear radii. He showed that the data can be interpreted by this assumption if the radius of the nuclear potential is given by $R=r_0A^{\frac{1}{3}}$, where $r_0=1.4$ to 1.5×10^{-13} cm.

It was clearly realized at that time that it would be

desirable to investigate departures from Coulomb scattering for a range of elements throughout the periodic table. Such data should be able to provide information concerning the extent and strength of the potential acting between the alpha particle and the nucleus. However, in order to observe departures from Coulomb scattering in nuclei other than the very lightest, it is necessary to have more energetic alpha particles than are produced by radioactive sources. Thus the extension of this field awaited the development of high-energy cyclotrons producing external beams of alpha particles.

III. FIRST CYCLOTRON EXPERIMENTS

A considerable amount of experimental work has been done on the elastic scattering of high-energy alpha particles by He, and also by lighter nuclei (or the inverse process); however, such experiments have not usually been interpreted on the basis of an optical model. (It might be, however, that interpretations of this sort will be suggestive.) Since optical models form the theme of this article, these experiments are not discussed.

The first of the modern experiments which is of interest here, in consideration of this limitation, was performed in 1950 by Gove at the M.I.T. cyclotron. The experiment consisted in measuring the angular distribution for the elastic scattering of 27.5-Mev alpha particles from a thin (26 mg/cm^2) foil of Au. The scattered particles were detected by a proportional counter range telescope adjusted to respond only to elastically scattered alpha particles. The angle of scattering of the alpha particles was measured with an accuracy of $\pm 0.5°$. A thin ionization chamber at the entrance to the evacuated scattering chamber was used to provide an absolute measurement of the incident beam intensity to accuracy $\pm 10\%$.

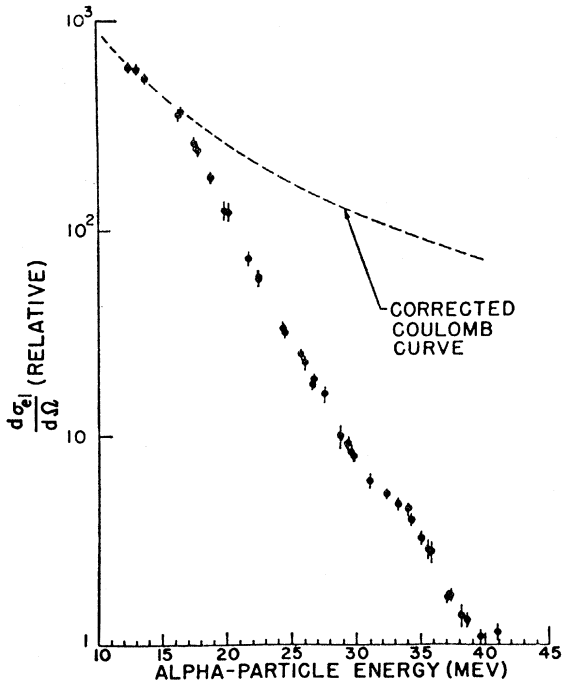

FIG. 3. Differential cross section for the elastic scattering of alpha particles by Ag at an angle of 60° as a function of alpha particle energy. Dashed curve is a Coulomb scattering curve corrected for angular variation arising from the fringing field of the cyclotron.

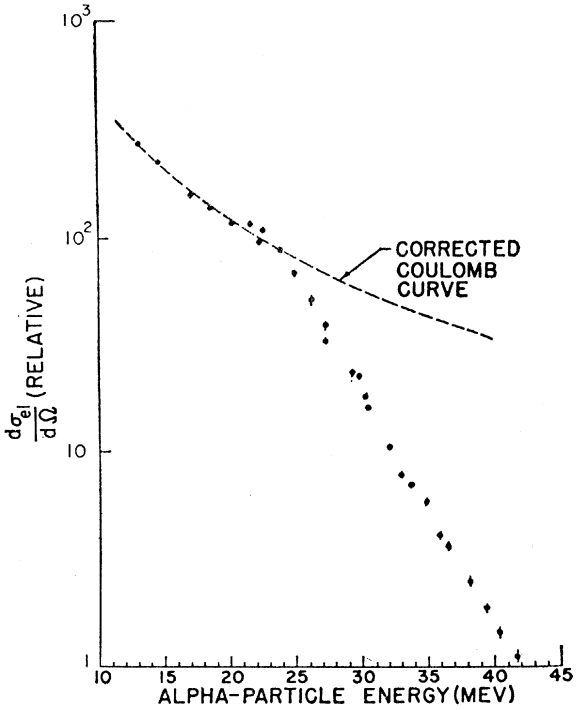

FIG. 4. Differential cross section for the elastic scattering of alpha particles by Ta at 60° as a function of alpha-particle energy.

Figure 2 shows the experimental results, plotted as the ratio of the measured cross section to the Coulomb cross section, for various scattering angles. The two dotted curves indicate the limits within which data from a measurement of pure Coulomb scattering would be found in consideration of the experimental uncertainty of $\pm 0.5°$ in the angular measurements. To within experimental uncertainty, the measured cross section is equal to the Coulomb cross section at scattering angles less than about 50°. At larger angles the measured cross section drops rapidly below the Coulomb cross section.

Gove's work was described in unpublished M.I.T. progress reports dated 1951 and, prior to publication in 1955 (20), was not widely known. In 1953 a set of experiments on the elastic scattering of high-energy alpha particles was performed by Farwell and Wegner at the University of Washington cyclotron (12). This work was followed by a period of renewed experimental and theoretical activity in the field.

The experiments of Farwell and Wegner involved measuring the energy dependence of the cross section for the elastic scattering of alpha particles from several heavy elements over the energy range 13 to 43 Mev.

The energy variation was accomplished by passing the external cyclotron beam through absorbers of variable thickness before the beam impinged on the thin scattering target. Elastically scattered alpha particles, emitted from the target at angles of about 60° or 95°, were detected in a proportional counter range telescope. Experimentally the contribution to the counting rate by inelastically scattered alpha particles, or other particles, was always less than 5%. The beam passing through the scattering target was monitored with a Faraday cup; however, only relative cross sections were measured. The entire experimental apparatus was located in the fringing field of the cyclotron. Consequently the alpha particles followed curved trajectories, with the curvature depending on their energy. Since the geometry of the apparatus was fixed, the actual scattering angle was a function of the energy of the alpha particle. For the "60°" case, the scattering angle ranged from 62° at 10 Mev to 59° at 40 Mev.

Figures 3–6 show the cross sections for the scattering from Ag, Ta, Pb, and Th measured at a scattering angle of about 60°. The dashed curves represent the energy dependence of pure Coulomb scattering, with a correction having been made for the variation in scattering angle which enters into the experiment. The experimental data have been normalized to the corrected Coulomb curves at small energies. In these data the measured cross sections agree with the Coulomb cross sections at low energies; however, above a certain critical energy, the measured cross sections drop rapidly below the Coulomb cross sections. Except for the kink

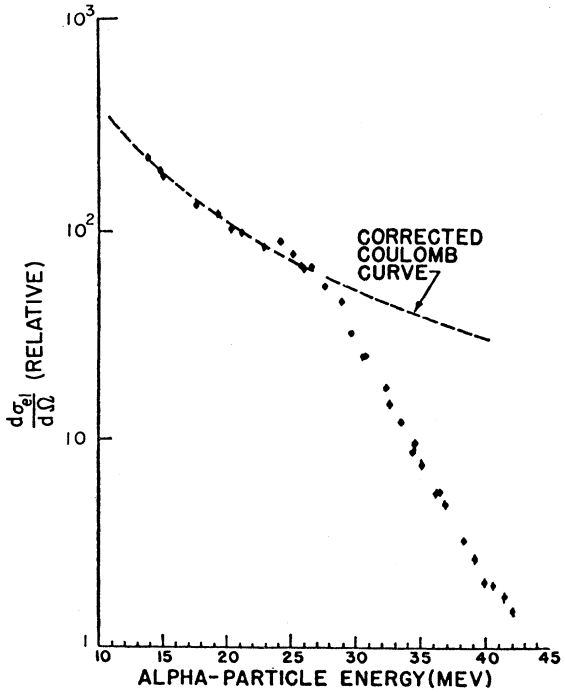

FIG. 5. Differential cross section for the elastic scattering of alpha particles by Pb at 60° as a function of the alpha-particle energy.

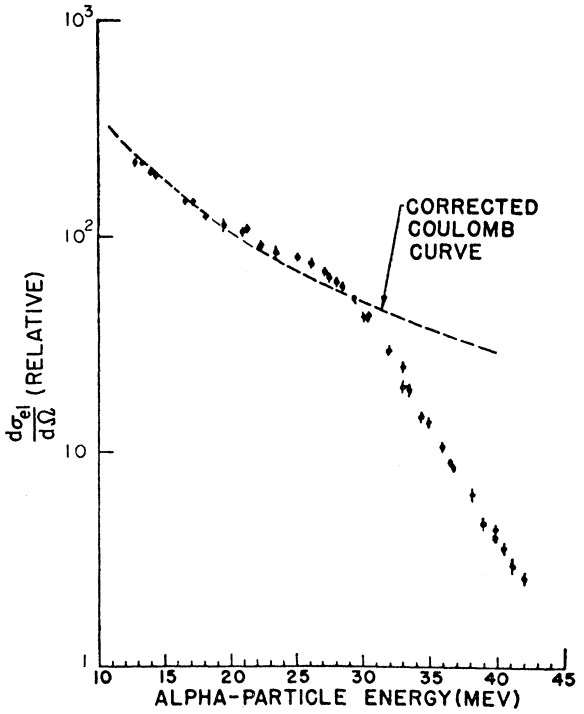

FIG. 6. Differential cross section for the elastic scattering of alpha particles by Th at 60° as a function of the alpha-particle energy.

in the Ag data, the energy dependence of the cross section in the falling region is given quite accurately by an exponential. There is a slight increase before the exponential decrease in the energy dependence of the cross section for the scattering from Th.

In the following year, additional experimental work was done by Wall, Rees, and Ford at the Indiana University cyclotron (59). They measured the angular distribution for the elastic scattering of 22-Mev alpha particles from Ag, Au, and Pb. A NaI scintillation counter was used to detect the scattered particles. The incident beam of alpha particles was monitored by a Faraday cup, but absolute values for the measured cross sections were obtained by normalizing to the Coulomb cross section at small scattering angles. The energy resolution of the detector was 8% (full width at half-maximum). The experimental procedure was to count all pulses larger than 85% of the pulse height of elastically scattered alpha particles. For the experiments on Au and Pb, this relatively poor energy resolution was adequate to provide discrimination against the alpha particles scattered by target contaminents such as carbon or oxygen. Adequate resolution of contaminent scattering was not possible in the experiment on Ag, so it was stated that the "Ag data represent at worst an upper limit." The question of the contribution to the measured counting rate from inelastically scattered alpha particles, or other particles, was not thoroughly discussed; however, subsequent work of various

experimental groups indicates that these effects are not serious in the experiments of Wall, Rees, and Ford.

Figures 7–9 show the ratio of the measured cross section to the Coulomb cross section for Ag, Au, and Pb at an energy of 22 Mev, plotted against scattering angle. Indicated errors were compounded from the statistical counting errors and the effect of a 0.5° uncertainty in the angular position of the detector. The departure of the two smallest angle Au points from the Coulomb cross section was considered to be purely experimental. These data are similar to the 27.5-Mev angular distribution in Fig. 2. At small angles the measured cross sections are equal to the Coulomb cross section. As the scattering angle increases, the Au and Pb data show an increase of about 10% in the ratio of the measured to Coulomb cross sections and then a smooth drop of this ratio to values of about 0.3. For Ag this ratio drops monotonically to values around 0.01.

Work at the Indiana cyclotron has continued. In a recent publication, Rees and Sampson (45) report measurements on the elastic scattering of 22-Mev alpha particles from Ta, Au, Bi, and U. On using a somewhat improved experimental technique, and with better statistical accuracy, they observe angular distributions in good agreement with Wall, Rees, and Ford.

IV. AKHIEZER-POMERANCHUK-BLAIR MODEL

The first modern interpretation of the alpha scattering data was given by Blair (4) on the basis of a model

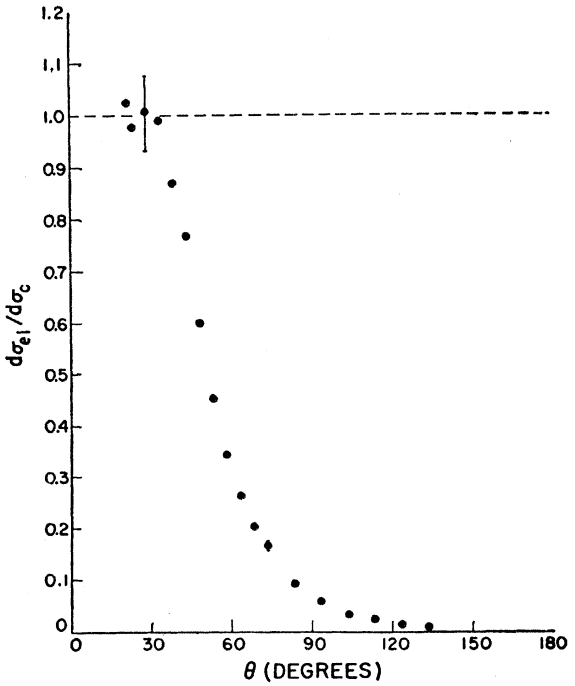

FIG. 7. Ratio to the Coulomb cross section of the differential cross section for the elastic scattering of 22-Mev alpha particles by Ag as a function of the scattering angle. Indicated errors arise from statistical counting errors and a 0.5° detector angle uncertainty.

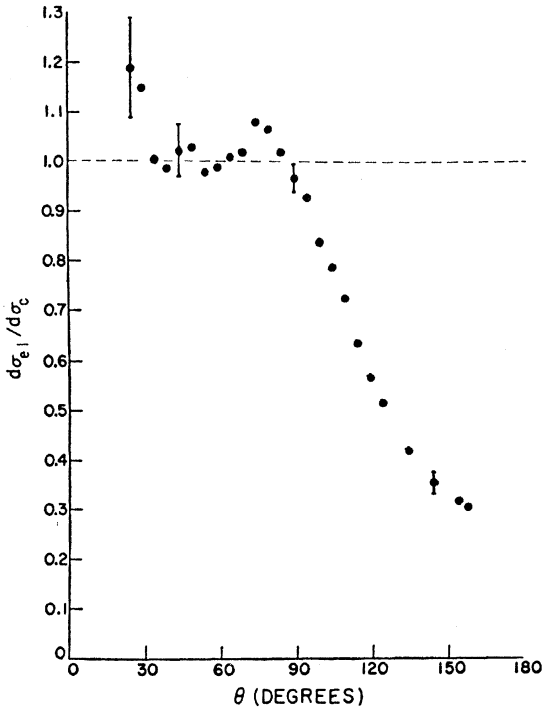

FIG. 8. Ratio to the Coulomb cross section of the differential cross section for the elastic scattering of 22-Mev alpha particles by Au as a function of the scattering angle.

proposed by Akhiezer and Pomeranchuk (1) which was originally developed to extend the ideas of Bohr, Peierls, Placzek, and Placzek and Bethe (41) to the small-angle scattering of charged particles. An essentially classical approximation is made. The justification is that in most of the applications the deBroglie wavelength λ is approximately an order of magnitude smaller than the interaction radius R, as shown in Fig. 10. The nucleus is considered to have a sharp spherical surface, specified by the radius R_A, and the incident alpha particle is also considered to have a sharp spherical surface, specified by the radius R_α. The sum of the two radii is equal to the interaction radius R. Since a classical approximation is being made, the incident particle is considered to follow a well-defined trajectory which, because of the nuclear charge and the charge of the alpha particle, is hyperbolic in the case illustrated in the figure in which the particle does not have enough energy to reach the nuclear surface. Also shown is the apsidal distance of closest approach D which for classical point Coulomb scattering is given by

$$D=(ZZ'e^2/2E)[1+\csc(\theta/2)]. \quad (1)$$

The orbital angular momentum L is directly expressed in terms of the scattering angle as

$$L=(ZZ'e^2/v)\cot(\theta/2). \quad (2)$$

Here Ze is the nuclear charge, $Z'e$ that of the incident particle, E and θ are the energy and scattering angle in

the center of mass system, and v is the relative velocity. Equation (1) shows that for constant angle the apsidal distance decreases as the energy increases and for constant energy the apsidal distance decreases as the scattering angle is increased. The APB model assumes that the target nucleus is completely opaque to the incident particle. This is expressed by saying that if the apsidal distance $D \leqslant R$, the incoming particle is removed from the incident beam by the nucleus and is therefore not elastically scattered. Thus from a strictly classical point of view we can easily sketch the behavior of the cross section for elastic scattering and also the absorption factor entering into the cross section for compound formation. From Eq. (1) we see that the maximum scattering angle θ_M, which is defined by $D=R$, is given as

$$\sin(\theta_M/2)=[(2ER/ZZ'e^2)-1]^{-1}$$
$$=\{[2E/V(R)]-1\}^{-1}. \quad (3)$$

Thus from Eq. (3), when E is greater than $V(R)$, there is a maximum scattering angle which is less than 180°. When E is less than $V(R)$, the apsidal distance D is always greater than the interaction radius R so that the entire scattering is elastic Coulomb scattering. We can write then

$$E<V(R): \ (d\sigma_{el}/d\Omega)(\theta)=(d\sigma_c/d\Omega)(\theta),$$

$$E>V(R): \ (d\sigma_{el}/d\Omega)(\theta)=\begin{cases}(d\sigma_c/d\Omega)(\theta), & 0<\theta<\theta_M \\ 0, & \theta_M<\theta<\pi.\end{cases} \quad (4)$$

This result is sketched in Fig. 11 for the case of $E>V(R)$.

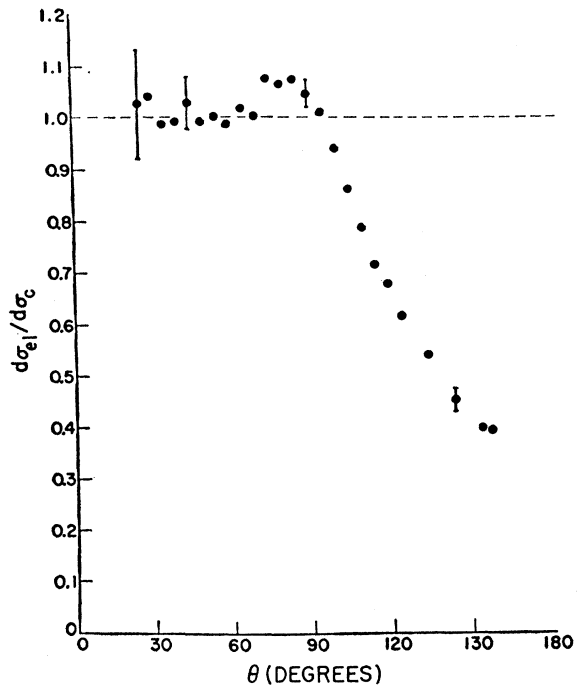

FIG. 9. Ratio to the Coulomb cross section of the differential cross section for the elastic scattering of 22-Mev alpha particles by Pb as a function of the scattering angle.

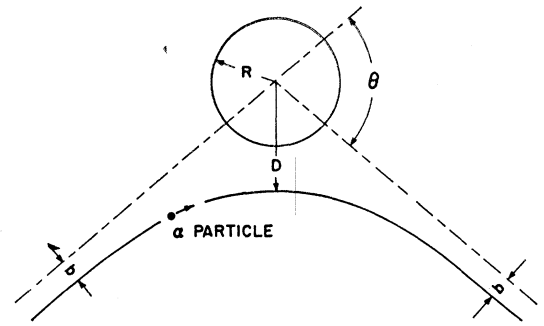

FIG. 10. Alpha-particle scattering showing the impact parameter b, the interaction radius R, the apsidal distance D, and the scattering angle θ.

We now consider the cross section for the removal of alpha particles from the incident beam, which is called the compound formation cross section σ_c. Figure 10 indicates the impact parameter b. Since the incident beam is assumed to be uniformly distributed with respect to impact parameter, it is easiest to formulate the compound formation cross section by using b. The expression one obtains for σ_c is

$$\sigma_c=\int_0^\infty db 2\pi b[1-T(b)], \quad (5)$$

where $T(b)$ is the fractional transmission for the orbit with impact parameter b. In principle, T can depend also on the energy of the incident particle, but we have not explicitly indicated this dependence here. Equation (5) can be expressed equivalently in terms of the angular momentum L of Eq. (2), since L is directly expressed in terms of the incident momentum p and the impact parameter b

$$L=pb. \quad (6)$$

By combining Eqs. (5) and (6) it is a simple matter to express σ_c as an integral over angular momentum which makes the correspondence with the quantum-mechanical formulas more obvious.

By applying the idea of an opaque nucleus to the transmission factor in Eq. (5), we can quite easily

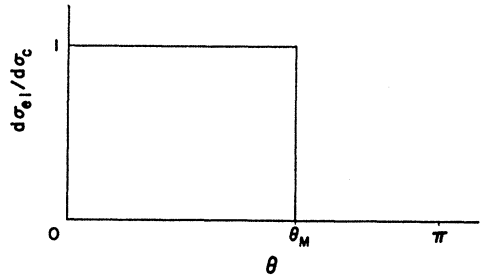

FIG. 11. Classical ratio to Coulomb scattering of the differential elastic scattering cross section for a completely absorbing sharp surface interaction region as a function of scattering angle. For Coulomb orbits leading to scattering angles $\theta>\theta_M$, complete absorption occurs.

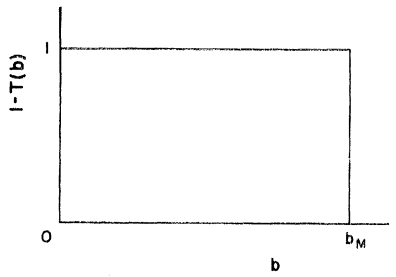

FIG. 12. Plot of $1-T(b)$ as a function of impact parameter b. For $b>b_M$, the Coulomb orbits miss the nucleus, $T(b)$ becomes 1, and $1-T(b)$ becomes zero.

calculate σ_c. We first need an expression for the transmission factor T as a function of the impact parameter b. When E is less than $V(R)$, T is 1; that is, all incident particles are elastically scattered. For E greater than $V(R)$, T is zero (the nucleus is opaque) for those orbits which hit the nucleus, and T is 1 for those orbits which do not hit the nucleus. In order to determine the maximum impact parameter b_M, which is such that smaller impact parameters correspond to orbits which hit the nucleus and larger impact parameters correspond to orbits which miss, we use Eqs. (2), (3), and (6). This gives

$$b_M=R[1-V(R)/E]^{\frac{1}{2}}. \tag{7}$$

Figure 12 shows $(1-T)$ as a function of b for the assumed opaque nucleus.

On combining these results, using Eqs. (5) and (7), we obtain (3, p. 346)

$$\sigma_c=\begin{cases}0, & E<V(R)\\ \pi R^2[1-V(R)/E], & E>V(R).\end{cases} \tag{8}$$

Figure 13 shows the compound formation cross section as a function of the energy. This summarizes the classical results, and provides the point of departure for the Akhiezer-Pomeranchuk-Blair model.

The arguments for the quantum-mechanical modification of the classical model, in an approximate way so that numerical calculations can be carried out fairly simply, begin with an examination of the expressions for the differential cross section for elastic scattering and the compound formation cross section. These can

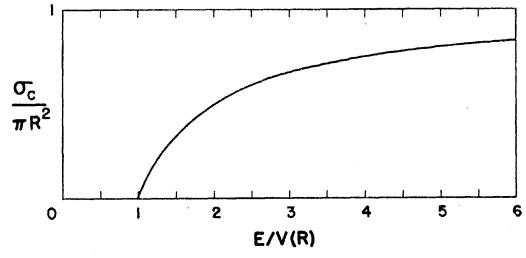

FIG. 13. Compound formation cross section σ_c divided by πR^2 as a function of the ratio of the incident energy E to the barrier height $V(R)$ for Coulomb scattering from a completely absorbing sharp surface interaction region.

be written

$$(d\sigma_{el}/d\Omega)(\theta)=|f(\theta)|^2, \tag{9}$$

where

$$f(\theta)=\frac{1}{2ik}\sum_{l=0}^{\infty}(\eta_l-1)(2l+1)P_l(\cos\theta), \tag{10}$$

and

$$\sigma_c=\pi\lambda\!\!\!^{-2}\sum_{l=0}^{\infty}(2l+1)(1-|\eta_l|^2). \tag{11}$$

Here $k=1/\lambda\!\!\!^{-}$ is the wave number of the incident alpha particle in the center of mass system, and η_l is the coef-

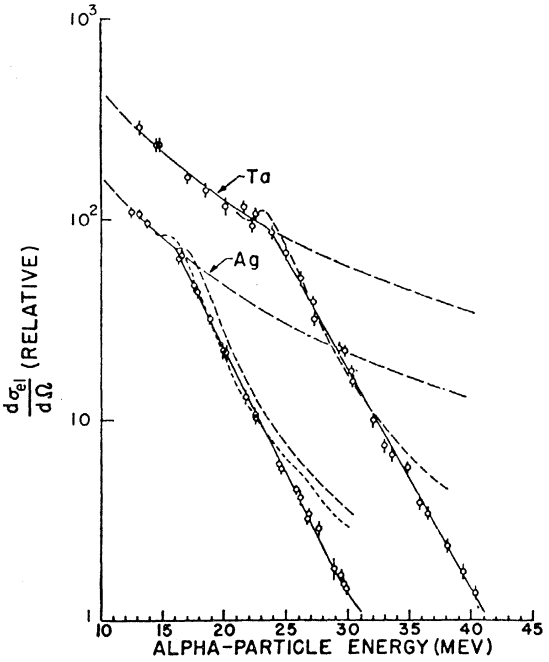

FIG. 14. Comparison of the differential cross section calculated from the APB model and experimental data for Ag and Ta. Experimental points were obtained from measurements at 60°. The broad dashed curve gives the Coulomb cross section and solid curves represent the experimental data of Farwell and Wegner. For Ag, two theoretical curves are shown; for the finer, $R=9.67\times10^{-13}$ cm; and for the coarser, $R=8.84\times10^{-13}$ cm. For Ta, the finer dashed curve gives the theoretical cross section for $R=10.54\times10^{-13}$ cm.

ficient of the lth outgoing spherical partial wave when the coefficient of the ingoing spherical wave is taken to be unity. The arguments leading to the APB model are of a quasi-classical type. Classically [from Eqs. (2) and (3)] there is defined an angular momentum l_M corresponding to θ_M that corresponds to a cutoff of the effects of nuclear opaqueness (trajectories with $l>l_M$ simply miss the nucleus). This is illustrated in Fig. 12 [see also Eq. (6)]. The quantum-mechanical formalism is thus modified by introducing a classical notion. For angular momenta larger than l_M the amplitude is set equal to the amplitude one would obtain for pure Coulomb scattering, while for l less than or equal to l_M there is no outgoing wave, since everything that comes

in is absorbed by the target nucleus; therefore, for l less than or equal to l_M, the amplitude of the outgoing wave must vanish. One thus obtains in some approximation a one-parameter (l_M) model for the scattering problem. [Classically, this l_M is measured directly by measuring σ_c. See Eqs. (6)–(8). Quantum mechanically the situation is not so simple, and l_M is used as a free parameter in fitting the data.] Thus we write

$$\eta_l=\begin{cases}0, & l<l_M\\ \eta_l^{\text{Coulomb}}, & l>l_M\end{cases}, \tag{12}$$

where the transition from the classical angular momentum L_M to the quantum-mechanical partial wave index l_M has been made via the connection $L_M=\hbar l_M$. From Eqs. (6) and (7) we readily find

$$l_M=kR[1-V(R)/E]^{\frac{1}{2}}. \tag{13}$$

For l larger than l_M, the incident particle has negative kinetic energy which is not a possible situation for particles described by classical mechanics.

By imposing the conditions of Eq. (12) on Eq. (10), one obtains

$$f(\theta)=\frac{n}{2ik}\frac{1}{\sin^2(\theta/2)}\exp[-in\ln\sin^2(\theta/2)+2i\sigma_0]$$
$$-\frac{1}{2k}\sum_{l=0}^{l_M}(2l+1)\exp(2i\sigma_l)P_l(\cos\theta), \tag{14}$$

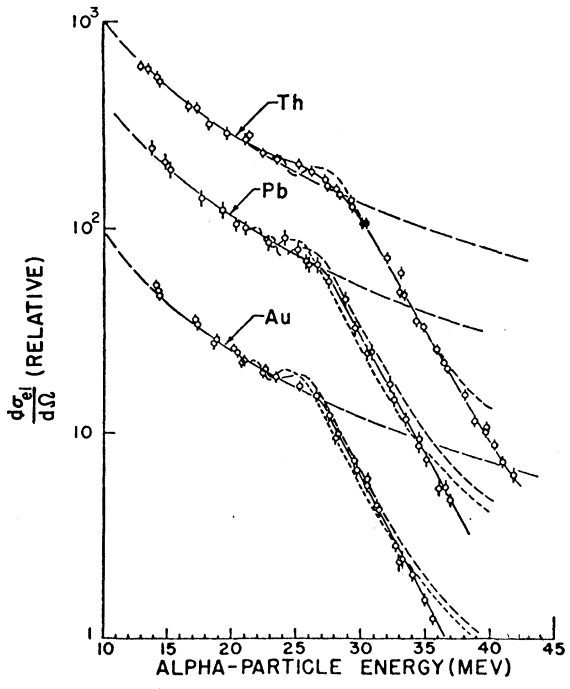

FIG. 15. Similar graphs for Au, Pb, and Th. For Au, the finer theoretical curve corresponds to $R=10.58\times10^{-13}$ cm and the coarser to $R=10.3\times10^{-13}$ cm. For Pb, the finer curve corresponds to $R=10.87\times10^{-13}$ cm and the coarser to $R=10.42\times10^{-13}$ cm. For Th, the dashed curve corresponds to $R=11.01\times10^{-13}$ cm.

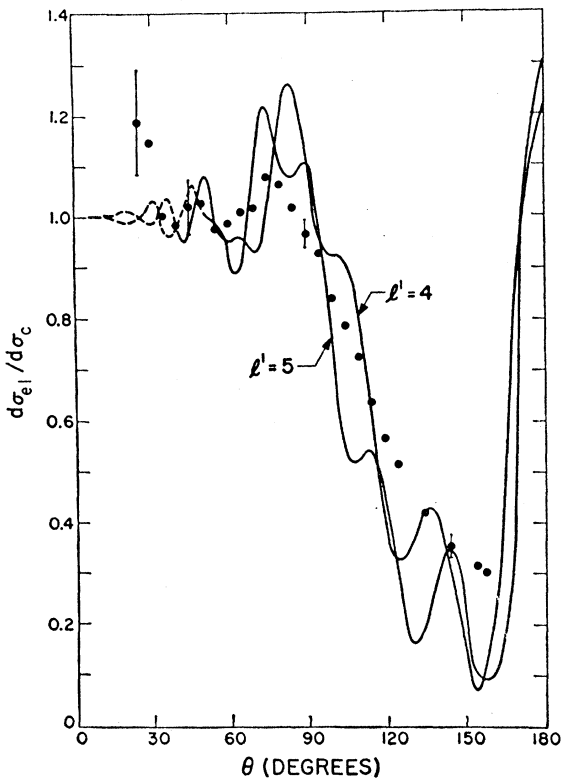

FIG. 16. Comparison of the Wall-Rees 22-Mev data for Au with the APB model.

where $n=ZZ'e^2/\hbar v$, and $\exp(2i\sigma_l)=\eta_l^{\text{C}}$ with

$$\sigma_l=\arg\Gamma(l+1+in). \tag{15}$$

The model also makes a prediction for the compound formation cross section which can be obtained from Eqs. (11) and (12) and reads

$$\sigma_c=\pi\lambda\!\!\!^{-2}\sum_{l=0}^{l_M}(2l+1)$$
$$=\pi\lambda\!\!\!^{-2}(l_M+1)^2$$
$$\simeq\pi R^2[1-V(R)/E],\quad E>V(R). \tag{16}$$

This is essentially the same as the classical result of Eq. (8).

The cross section for elastic scattering, $d\sigma_{el}/d\Omega=|f(\theta)|^2$, is evaluated by numerical computation from Eqs. (14) and (10). The result can be expressed as

$$d\sigma_{el}/d\Omega=(d\sigma_{el}/d\Omega)(Z,E,l_M,\theta).$$

In applying this model to the data of Farwell and Wegner, Z and θ are fixed by the conditions of the experiment. The value of l_M is found by trial which gives the best fit to the measured energy dependence. From this l_M the interaction radius R is calculated from Eq. (13). Figures 14 and 15 show a comparison of experiment and theory for the cross sections of five nuclei

from Ag to Th at a scattering angle of 60°. In several cases two theoretical curves are shown, corresponding to two different values of l_M. The interaction radii are obviously not determined unambiguously; however, they are in approximate agreement with the formula

$$R=(1.5A^{\frac{1}{3}}+2.0)\times 10^{-13} \text{ cm}.$$

The constant term is presumably related to the size of the alpha particle.

Curves of the cross section versus energy calculated from Eq. (14) actually show small amplitude oscillations. The theoretical curves shown in Figs. 14 and 15 have been averaged over these oscillations. This was justified by attributing the presence of the oscillations to the sharp boundary condition. Blair assumed that a more realistic and less sharp boundary condition would predict that these oscillations are damped.

Figures 16 and 17 show cross sections calculated from the APB model fitted to the experimental angular distributions of Wall, Rees, and Ford. The theoretical curves are those which come directly from the APB formulas. No averaging over the oscillations has been done.

The interaction radii which are calculated from the values of l_M producing the best fit to the angular distribution data are in approximate agreement with the values deduced from fitting the energy dependence data.

The APB model is thus quite successful in explaining the departure of the cross section from Coulomb scattering and also the drop from the Coulomb scattering cross section down to about 0.10 of the Coulomb scattering cross section. The inherent approximations begin to cause difficulty below this level and toward backward scattering angles; also, the theoretical cross sections have an oscillatory nature which appears to be difficult to remove, but which is not found experimentally.

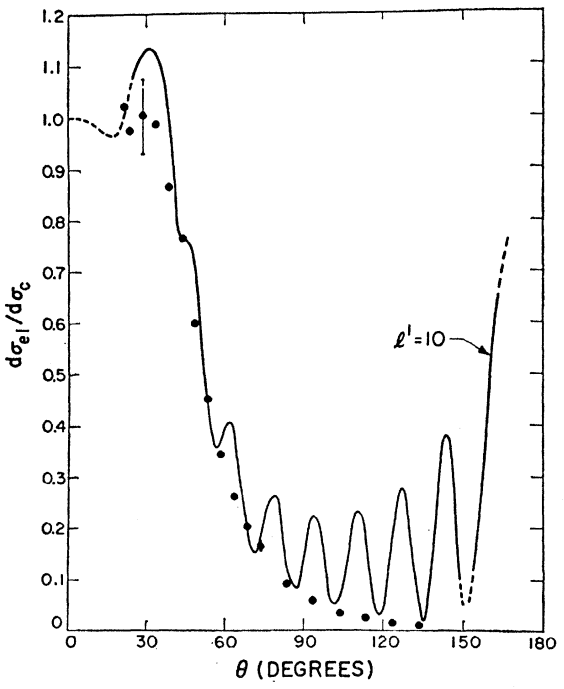

FIG. 17. Comparison of the Wall-Rees 22-Mev data for Ag with the APB model.

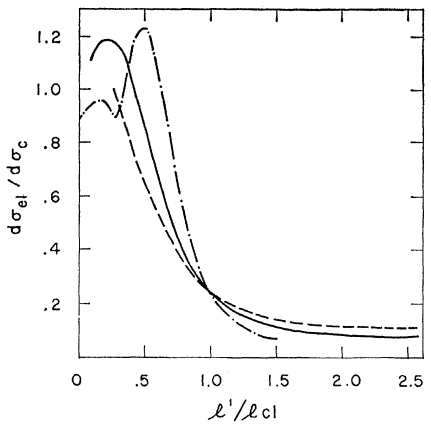

FIG. 18. Ratio of the differential cross section to the Coulomb cross section versus the ratio l'/l_{cl} of the cutoff angular momentum l' to the classical angular momentum $l_{cl}=n\cot(\theta/2)$ at a scattering angle of 90° for different values of the Coulomb parameter n. The curves intersect at a ratio value of about $\frac{1}{4}$, —·—·—·, $n=20$; ———, $n=10$; — — —, $n=7$.

In addition to proposing the APB model to explain angular distributions of elastically scattered alpha particles, Blair also suggested a criterion for determining radii from the data that differs from the simple adjustment of the interaction radius R. This method is called the "one-quarter-point recipe." The physical argument for this runs as follows. When the interaction radius is equal to the apsidal distance of the classical orbit, the quantum-mechanical Coulomb wave packet, which is centered about the classical trajectory, is considered to be half inside and half outside of the opaque region of the target nucleus-alpha particle interaction. Therefore, since the amplitude is reduced by one-half, the intensity drops by one-quarter, and the ratio of actual elastic scattering to pure Coulomb scattering is one-quarter. This effect is shown in Fig. 18 in which the ratio of the cross section to Coulomb cross section is plotted against the maximum l, l' ($\equiv l_M$) divided by the l obtained classically for scattering at 90° for particular values of the Coulomb parameter n. The curves intersect approximately at the point where the ratio to Coulomb is one-quarter. In order to obtain the interaction radius from the one-quarter-point recipe, use is made of (1), inserting the angle and energy for which the measured ratio to Coulomb is $\frac{1}{4}$. This apsidal distance is then called the one-quarter-point radius.

Kerlee, Blair, and Farwell (34) have used a slight modification of the one-quarter-point recipe which is called the "crossover-point recipe." This modification was necessitated by slight deviations from the idea behind the one-quarter-point recipe. The changed recipe is somewhat more empirical than the quarter-

point recipe in that the idea behind it arises from graphical results noticed in the course of numerical computations.

V. APSIDAL DISTANCE

After the experimental work of Wall, Rees, and Ford, data existed on the cross section as a function of energy at fixed angle and on the cross section as a function of angle at fixed energy. It was natural to try to make a direct comparison of these data by plotting the data as a function of some parameter common to both experiments. In doing this Wegner discovered an interesting fact (61, p. 56). He plotted $d\sigma_{el}/d\sigma_c$, the ratio of the observed cross section to the Coulomb cross section, as a function of the apsidal distance of the classical trajectory. From the energy and scattering angle the apsidal distance was calculated using the relation between these quantities for the case of pure Coulomb scattering. This comparison is shown in Fig. 19. At apsidal distances large compared to the nuclear radius, all the data coincide because $d\sigma_{el}/d\sigma_c$ must approach 1; however, the behavior of the data at small apsidal distances was surprising. The apsidal distance was calculated by assuming the formulas for Coulomb scattering, yet the data continue to coincide approximately when the Coulomb scattering formulas are not valid

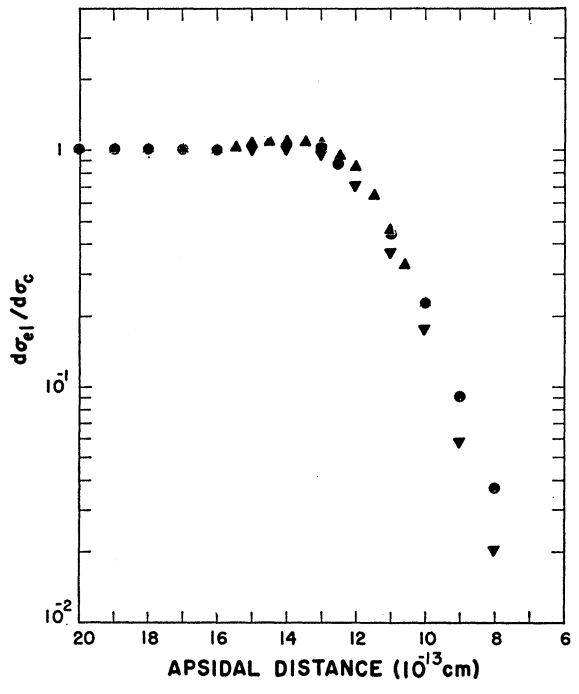

FIG. 19. Wegner plot of the experimental ratio of the differential cross section to the Coulomb cross section for the scattering of alpha particles by Au as a function of apsidal distance. Both angular data at fixed energy and energy data at fixed angle are shown. These data coincide for at least $(d\sigma_{el}/d\sigma_c) \geq 0.1$ suggesting that the major variation of the ratio for heavy nuclei enters primarily through the apsidal distance. ▲, α's on Au, 22 Mev, 20°–60°; ●, α's on Au, 13–44 Mev, 60°; ▼, α's on Au, 13–44 Mev, 95°.

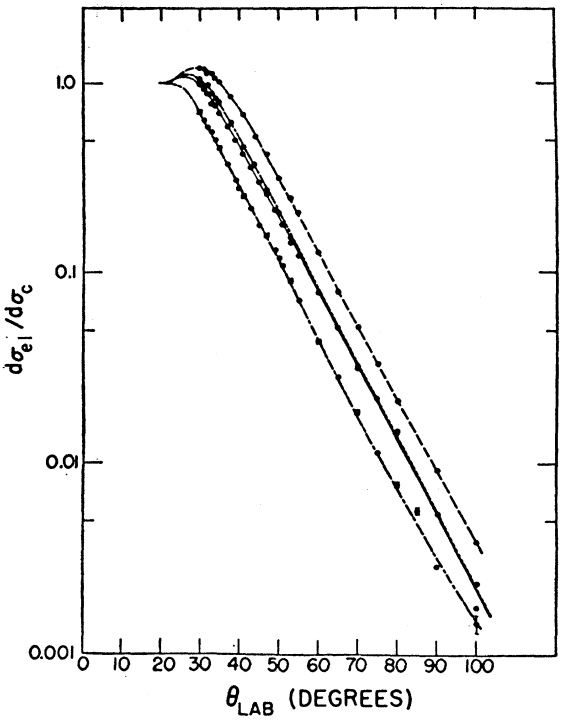

FIG. 20. Ratios of the experimental differential cross sections to the Coulomb cross section as a function of scattering angle for 40-Mev alpha particles on Ta, —·—·—; Au, ———; Pb, ------; and Th, — — —.

since $d\sigma_{el}/d\sigma_c < 1$. This qualitative dependence of $d\sigma_{el}/d\sigma_c$ on the apsidal distance alone was not easy to understand on the basis of the APB model.

VI. MEASUREMENTS ON HEAVY ELEMENTS AT HIGHER ENERGIES

The next development consisted of an extension to higher bombarding energies of the angular distributions for elastic scattering from heavy elements. This was studied to see whether $d\sigma_{el}/d\sigma_c$ would continue to decrease with increasing angle at higher energies, or whether it would eventually level off, as predicted by the APB model. It was also of interest to see whether over a wider range of parameters, $d\sigma_{el}/d\sigma_c$ was still approximately only a function of the apsidal distance.

These experiments were performed by Wegner, Eisberg, and Igo using a 40-Mev alpha particle beam from the Brookhaven cyclotron (62). Particles scattered in the angular range 20° to 160° were detected by a NaI scintillation counter. Elastically scattered alpha particles were separated from inelastic alphas and other particles by a technique combining pulse-height analysis and differential energy loss in thin absorbers. The beam was monitored by a second scintillation counter which detected alpha particles elastically scattered from the target at a fixed angle of 26°. As in earlier experiments, absolute cross sections were obtained by normalizing to the Coulomb cross section at small scattering angles; however, at 40 Mev the minimum angle of observation

of 20° was not quite small enough to allow a very convincing normalization to be made.

Figure 20 shows the results of measurements made on Ta, Pb, Au, and Th. The ratio $d\sigma_{el}/d\sigma_c$ is plotted as a function of scattering angle. In the region 20° to 30° smooth curves represent the experimental results; data points have been omitted for the sake of clarity. After an initial rise, similar to that observed in the earlier experiments, the ratio $d\sigma_{el}/d\sigma_c$ drops rapidly with increasing scattering angle to values approaching 10^{-3} at 100°. Beyond this angle the cross section could not be measured since the elastically scattered alpha particles were not resolvable. However, an upper limit to the cross section could be obtained. For Au, $d\sigma_{el}/d\sigma_c$ is less than 3×10^{-4} at scattering angles of 130° and 155°.

Figure 21 shows the Ta data and the cross section calculated for Ta by the APB model, using three different values of the parameter l'.

Comparison of the APB model with the 40-Mev data shows again that it can give a good fit in the region $d\sigma_{el}/d\sigma_c>0.1$; however, the experimental data are in complete disagreement with the predictions of the model when the ratio of the experimental cross section to the Coulomb cross section is less than about 0.1. The APB model predicts much too large a cross section at large angles. Subsequently Ellis and Schecter tried fitting similar data with an APB model in which the transition from complete absorption to no absorption was tapered over three or four partial waves (11). This does not appear to decrease the discrepancy between the APB model and the more stringent test presented by the higher-energy angular distribution. However, as discussed in the next section, there is some question regarding the numerical correctness of these computations.

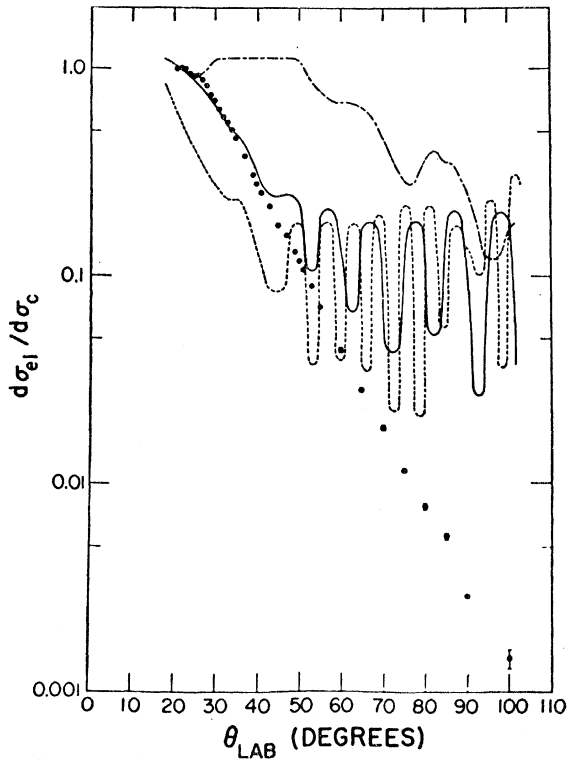

FIG. 21. Ta data at 40 Mev, with theoretical predictions of the APB model for three values of the cutoff angular momentum l' as indicated. ——·——, $l'=7$; ———, $l'=17$, -----, $l'=27$; ●, experiment.

VII. SMOOTHED AKHIEZER-POMERANCHUK-BLAIR MODEL

Although the calculations by Blair are successful in fitting the experimental alpha-particle data in the region of the departure from pure Coulomb scattering down to a level of about 10% of Coulomb scattering, they clearly begin to lose their meaning at backward angles, where the differential cross section drops many orders of magnitude below the Coulomb scattering level. In order to try to improve the Blair calculations, Wall, Rees, and Ford (59) suggested a modification in which the sharp cutoff of the scattering amplitude is smoothed out. Cheston and Glassgold (6), showed by plotting $\sigma_c^{(l)}/\pi\lambda^2(2l+1)$ against l, that the amplitude should be expected to fall off gradually in magnitude over a few l values.

It has been pointed out recently (11) that the numerical work associated with these and similar smoothed calculations is probably in error and that such an approach is more successful than had been thought originally. The smoothing procedure of McIntyre, Wang, and Becker (37), consists of introducing a semiempirical variation of both the magnitude and phase of the scattering amplitude A_l. The magnitude $|A_l|$ of A_l is varied by (arbitrarily) writing

$$|A_l|=\{1+\exp[-(l-l_A')/\Delta l_A]\}^{-1}, \qquad (17)$$

in which the transition of $|A_l|$ from 0 to 1 occurs over an interval of width Δl_A in the neighborhood of l_A'. Thus two parameters are introduced in Eq. (17).

In addition a real nuclear phase shift δ_l is introduced with a similar (arbitrary) formula

$$\delta_l=\delta\{1+\exp[(l-l_\delta')/\Delta l_\delta]\}^{-1}, \qquad (18)$$

in which the three parameters l_δ', Δl_δ, and δ are introduced. The first two of these have significance analogous to the parameters in Eq. (17), while δ determines the magnitude of the nuclear phase shift.

The ratio to Coulomb scattering is determined from Eqs. (17) and (18) from the standard formula

$$\frac{d\sigma_{el}}{d\sigma_c}=\left|-i\exp[-in\ln\sin^2(\theta/2)]-\frac{\sin^2(\theta/2)}{n}\sum_{l=0}^{\infty}(2l+1)(1-|A_l|e^{2i\delta_l})\times e^{2i(\sigma_l-\sigma_0)}P_l(\cos\theta)\right|^2, \qquad (19)$$

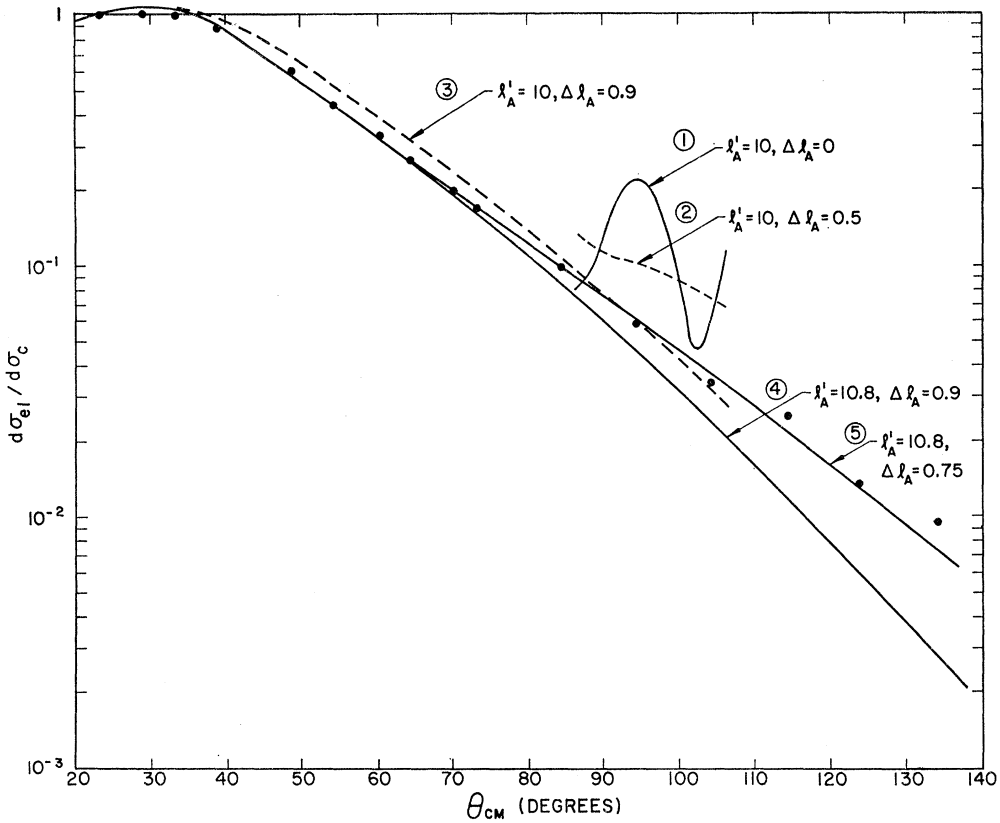

FIG. 22. Ratio of the experimental 22-Mev data for Ag to the Coulomb cross section, with a number of theoretical curves for the smoothed APB model.

in which $n=2Ze^2/\hbar v$, and σ_l is the usual Coulomb phase shift. Clearly, from Eq. (19) and the generality of Eqs. (17) and (18), this model constitutes an optical model in which the parameters enter directly into the amplitude according to Eqs. (17) and (18) rather than appearing as the parameters directly relevant to the form of a complex potential.

Figure 22 shows a series of curves labeled 1–5 with successive values of the parameters entering into $|A_l|$ chosen to approach a good fit to the 22-Mev Ag data and to illustrate the improvement over the sharp cutoff model ($\Delta l_A=0$). In this figure the smoothing is achieved completely through the imaginary part of the phase shift (or $|A_l|$), the real part of the phase shift being set equal to zero. Similar results occur in the optical model fitting of N–N elastic scattering for which the real part of the phase shift could be set equal to zero without appreciably altering the goodness of fit (44, see Fig. 10). Comparable results for alpha particles are discussed in the section on the optical model fits.

In order to fit the 40-Mev Ag data shown in Fig. 23, McIntyre *et al.* (37) find it necessary to include a nonzero value for the real part of the nuclear phase shift. Under the conditions $l_A'=l_\delta'$ but *not* $\Delta l_A=\Delta l_\delta$, satisfactory adjustment to the data can be obtained.

Perhaps the most significant feature of these results is the attempt to circumvent the known (32) elasticities in the features of the optical model potentials determined by detailed data fitting. Whether parametrizations of the form of Eqs. (17) and (18) will turn out to be related more easily than the optical model parameters to the fundamental features of the many-body problem remains to be seen. Some recent work (21) on high-energy neutron scattering approaches the problem from a similar point of view.

VIII. FORD-WHEELER MODEL

Ford and Wheeler (13) have developed a fairly complete analysis of the semiclassical description of scattering. Although most of this analysis is designed to be applicable to nonabsorptive scattering, they have modified their methods in some cases to try to take into account the major consequences of absorption. The major emphasis of the semiclassical analysis is to point out situations in which the semiclassical limit of the quantum-mechanical cross section does *not* approach uniformly the corresponding classical cross section, no matter how short is the wavelength of the incident particle. These nonuniform features are expected to be the rule rather than the exception for most potentials, although there are potentials (e.g., for the Coulomb potential, the quantum, semiclassical, and classical

cross sections are identical) for which these nonuniformities do not arise.

The quantum-mechanical differential scattering cross section $d\sigma_{qu}/d\Omega$ is expressed in terms of the quantum-mechanical scattering amplitude $f_{qu}(\theta)$ as

$$d\sigma_{qu}/d\Omega = |f_{qu}(\theta)|^2. \tag{20}$$

The amplitude $f_{qu}(\theta)$ is traditionally expressed as a sum of the amplitudes for the different partial waves:

$$f_{qu}(\theta) = \frac{\lambda\!\!\!^{-}}{2i}\sum_{l=0}^{\infty}(2l+1)(e^{2i\eta_l}-1)P_l(\cos\theta), \tag{21}$$

where η_l is the phase shift for the lth partial wave.

In order to obtain the semiclassical limit of Eqs. (20) and (21), the phase shift η_l is replaced by its JWKB approximation (40, p. 1102)

$$\eta_l = \int_{r_0}^{\infty}[k^2-U(r)-(l+\tfrac{1}{2})^2/r^2]^{\frac{1}{2}}dr - \int_{r_1}^{\infty}[k^2-(l+\tfrac{1}{2})^2/r^2]^{\frac{1}{2}}dr, \tag{22}$$

in which r_0 [the turning point in the presence of a potential $U(r)$] and r_1, are determined by the equations

$$\begin{aligned} k^2-U(r_0)-(l+\tfrac{1}{2})^2/r_0^2 &= 0, \\ k^2-(l+\tfrac{1}{2})^2/r_1^2 &= 0. \end{aligned} \tag{23}$$

The integral in Eq. (22) not involving $U(r)$ can be evaluated to give

$$\eta_l = \frac{\pi}{4}+\frac{l\pi}{2}-kr_0 + \int_{r_0}^{\infty}\{[k^2-U(r)-(l+\tfrac{1}{2})^2/r^2]^{\frac{1}{2}}-k\}dr. \tag{24}$$

This is independent of r_1. (The equivalent result for scattering in two dimensions is obtained by the replacement of $l+\frac{1}{2}$ by m.)

For θ not too near 0 or π (i.e., $\sin\theta \gtrsim 1/l$), the Legendre function in Eq. (21) can be replaced by (28, p. 297)

$$P_l(\cos\theta) \simeq \sin[(l+\tfrac{1}{2})\theta+\pi/4]/[(l+1)(\pi/2)\sin\theta]^{\frac{1}{2}}. \tag{25}$$

Under the circumstance that many partial waves contribute to the scattering and that η_l is given to a good approximation by Eq. (24) and P_l by Eq. (25), it is possible to replace the summation over partial waves in (21) by an integration. Combination of Eqs. (21), (24), and (25) under these conditions give the *semi-*

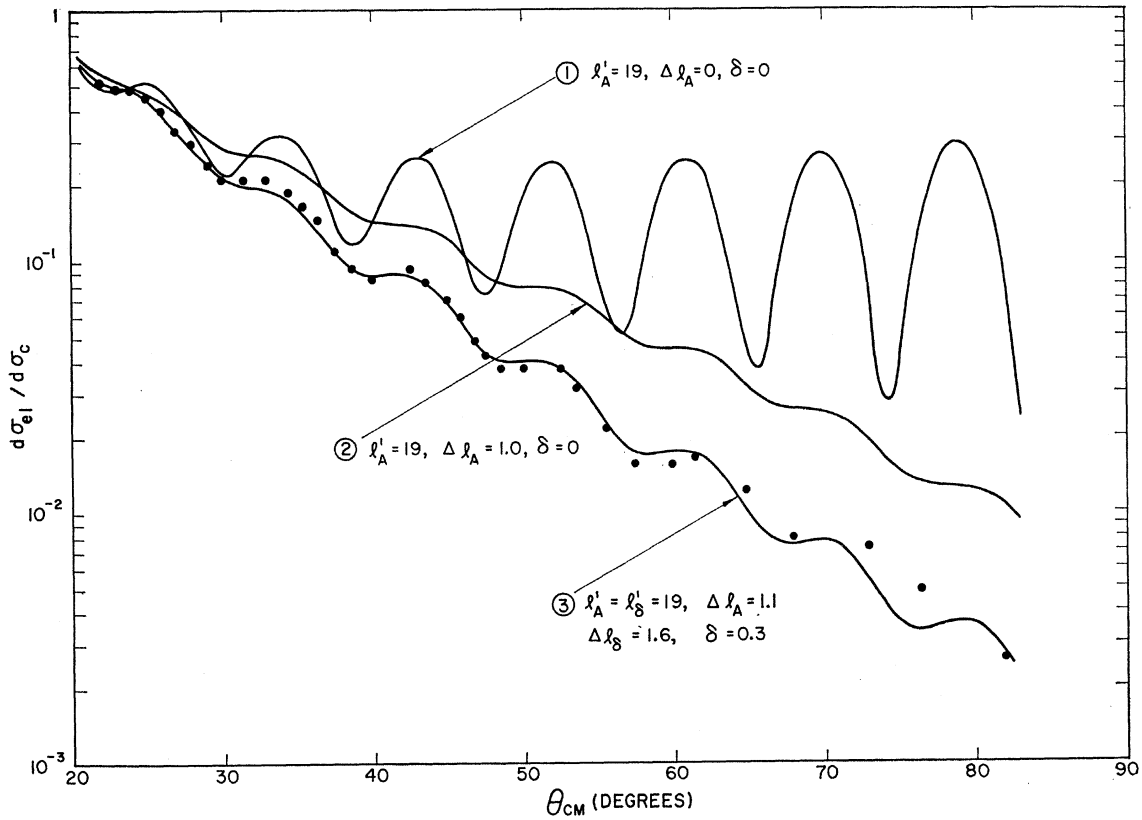

FIG. 23. Ratio of the experimental 40-Mev Ag data to the Coulomb cross section along with a number of theoretical curves for the smoothed APB model. Here it has been necessary to introduce a real part to the phase shift with the corresponding cutoff angular momentum l_δ' and transition width Δl_δ.

classical form of Eq. (21):

$$f_{sc}(\theta)=-\frac{\lambda}{(2\pi\sin\theta)^{\frac{1}{2}}}\int_0^\infty dl(l+\tfrac{1}{2})^{\frac{1}{2}}[e^{i\varphi_+}-e^{i\varphi_-}], \quad (26)$$

where

$$\varphi_\pm=2\eta_l\pm(l+\tfrac{1}{2})\theta\pm\pi/4. \quad (27)$$

Since we are concerned with nonforward angles in Eq. (26), the delta-function contribution in Eq. (21) has been dropped, i.e.,

$$\sum_{l=0}^{\infty}(2l+1)P_l(\cos\theta)=2\delta(1-\cos\theta), \quad =0, \quad \theta\neq 0. \quad (28)$$

The usual next step (39, p. 123) is to evaluate the integral in Eq. (26) by an approximate method, such as the method of stationary phase. An uncritical use of this method leads at once to $d\sigma_{sc}/d\Omega=d\sigma_{cl}/d\Omega$, i.e., equality between the *semi*classical and classical results. We seek a value l_θ of l such that $\varphi_\pm$ are stationary:

$$(d\varphi_\pm/dl)(l_\theta)=0. \quad (29)$$

It is then assumed that contributions to the integral in Eq. (26) come mainly from the region $l\simeq l_\theta$ and that an expansion of $\varphi_\pm$ to second order in $(l-l_\theta)$ is sufficient to approximate the integral. From Eqs. (24) and (27),

$$\frac{d\varphi_\pm}{dl}=\pi+2\int_{r_0}^\infty\frac{d}{dl}\{[k^2-U(r)-(l+\tfrac{1}{2})^2/r^2]^{\frac{1}{2}}-k\}dr\pm\theta. \quad (30)$$

The classical equation connecting the angular and radial positions along a scattering orbit is (19, p. 73)

$$\chi(r)=\int_{r_0}^r\frac{Ldr'}{r'^2[2m(E-V)-L^2/r'^2]^{\frac{1}{2}}}+\chi_0, \quad (31)$$

which can be written

$$\chi(r)=-\int_{r_0}^r\frac{d}{dL}[2m(E-V)-L^2/r'^2]^{\frac{1}{2}}dr'+\chi_0. \quad (32)$$

In Eqs. (31) and (32), V is the potential and L is the total angular momentum (*not* in units of $\hbar$). If we write $L=\hbar(l+\frac{1}{2})$, then Eq. (32) becomes

$$\chi(r)=-\int_{r_0}^r\frac{d}{dl}[k^2-U(r')-(l+\tfrac{1}{2})^2/r'^2]^{\frac{1}{2}}dr'+\chi_0. \quad (33)$$

If r_0 is the classical turning point, as defined in the first of Eqs. (23), the classical scattering angle $\Theta(l)$ is (see Fig. 24)

$$\Theta(l)=\begin{cases}\pi-2(\chi_\infty-\chi_0), & \chi_\infty-\chi_0<\pi/2\\ 2(\chi_\infty-\chi_0)-\pi, & \chi_\infty-\chi_0>\pi/2.\end{cases} \quad (34)$$

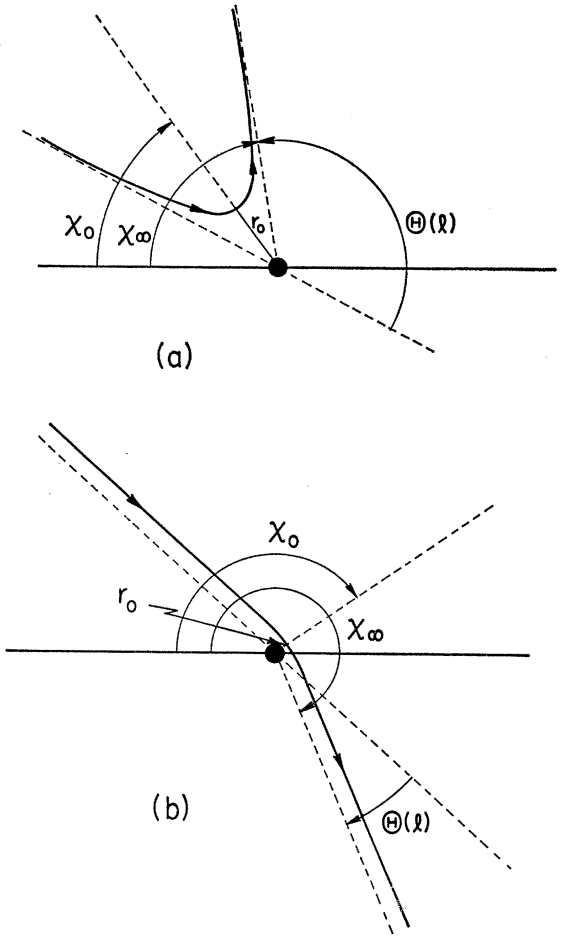

FIG. 24. Scattering geometry for (a) an attractive and (b) a repulsive potential. The classical turning point radius r_0 and angle χ_0 are shown along with the final asymptote angle χ_∞ and the deflection angle $\Theta(l)$.

From Eqs. (33) and (34) we find

$$\Theta(l)=\begin{cases}\pi+2\int_{r_0}^\infty\frac{d}{dl}[k^2-U(r)-(l+\frac{1}{2})^2/r^2]^{\frac{1}{2}}dr, & \chi_\infty-\chi_0<\pi/2\\ -2\int_{r_0}^\infty\frac{d}{dl}[k^2-U(r)-(l+\frac{1}{2})^2/r^2]^{\frac{1}{2}}dr-\pi, & \chi_\infty-\chi_0>\pi/2.\end{cases} \quad (35)$$

Comparison of Eqs. (30) and (35), with reference to Fig. 24, leads to the conclusion that in the semiclassical limit for a repulsive potential, φ_- is stationary for some value l_θ of l, and in the case of an attractive potential, φ_+ is stationary for some value l_θ of l. Both phases cannot be stationary simultaneously, so it is natural to assume that the contributions from the term containing the nonstationary phase is negligible. To see how the argument proceeds, we work out the case of a repulsive potential (φ_- stationary). This gives for the

semiclassical scattering amplitude

$$f_{sc}(\theta)\simeq\frac{\lambda\!\!\!^{-}}{(2\pi\sin\theta)^{\frac{1}{2}}}\int_0^\infty dl(l+\tfrac{1}{2})^{\frac{1}{2}} \times\exp\left\{i\left[\varphi_-(l_\theta)+\frac{d^2\varphi_-}{dl^2}(l_\theta)\frac{(l-l_\theta)^2}{2}\right]\right\}, \quad (36)$$

which can be written

$$f_{sc}(\theta)\simeq\lambda\!\!\!^{-}\left(\frac{l_\theta+\frac{1}{2}}{2\pi\sin\theta}\right)^{\frac{1}{2}}\exp[i\varphi_-(l_\theta)] \times\int_0^\infty dl\exp\left[i\frac{1}{2}\frac{d^2\varphi_-}{dl^2}(l_\theta)(l-l_\theta)^2\right]. \quad (37)$$

If l_θ is large, then

$$\int_0^\infty dl\exp\left[i\frac{1}{2}\frac{d^2\varphi_-}{dl^2}(l_\theta)(l-l_\theta)^2\right] \simeq\left[\frac{2}{|\varphi_-''(l_\theta)|}\right]^{\frac{1}{2}}\int_{-\infty}^{+\infty}d\xi\exp[i\xi^2(\varphi_-''/|\varphi_-''|)], \simeq\left[\frac{2}{|\varphi_-''(l_\theta)|}\right]^{\frac{1}{2}}\pi^{\frac{1}{2}}\exp[i(\pi/4)(\varphi_-''/|\varphi_-''|)]. \quad (38)$$

Thus

$$f_{sc}(\theta)\simeq\lambda\!\!\!^{-}\left(\frac{l_\theta+\frac{1}{2}}{\sin\theta|\varphi_-''(l_\theta)|}\right)^{\frac{1}{2}} \times\exp\{i[\varphi_-(l_\theta)+(\pi/4)(\varphi_-''/|\varphi_-''|)]\}, \quad (39)$$

so that

$$(d\sigma_{sc}/d\Omega)(\theta)\simeq\lambda\!\!\!^{-2}(l_\theta+\tfrac{1}{2})/\sin\theta|\varphi_-''(l_\theta)|, \quad (40)$$

in which l_θ is a function of the observation angle θ determined by Eqs. (29) and (30). From Eq. (27) we have that

$$(d^2\varphi_-/dl^2)(l_\theta)=2(d^2\eta_l/dl^2)(l_\theta), \quad (41)$$

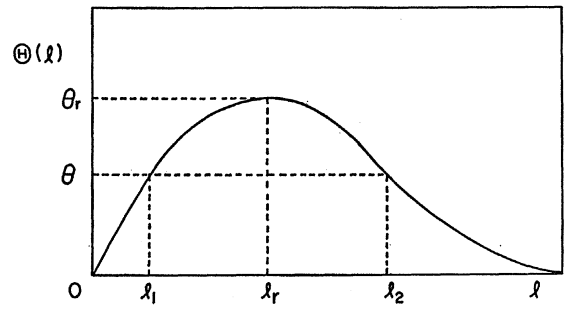

FIG. 25. The classical deflection function $\Theta(l)$ vs angular momentum l for a typical two-branch case. At the scattering angle θ, contributions to the scattering arise from both l_1 and l_2, leading to interference effects in the semiclassical cross section. When l_1 and l_2 coalesce to the value l_r, the phenomenon of rainbow scattering arises at the rainbow angle θ_r.

which can be written, from Eqs. (24) and (35),

$$(d^2\varphi_-/dl^2)(l_\theta)=(d\Theta/dl)(l_\theta)=(d\Theta/dl)|_{\Theta=\theta}. \quad (42)$$

This gives for Eq. (40),

$$(d\sigma_{sc}/d\Omega)(\theta)\simeq\lambda\!\!\!^{-2}(l_\theta+\tfrac{1}{2})/\sin\theta|d\Theta/dl|_{\Theta=\theta}, \quad (43)$$

expressed in terms of the classical deflection function Θ and the angle of observation θ. The same formal result is obtained for an attractive potential, although Θ is negative in that case (see Fig. 24).

The classical formula for the differential scattering cross section is (19, p. 82)

$$d\sigma_{cl}/d\Omega=b/\sin\Theta|d\Theta/db|, \quad (44)$$

in which b is the impact parameter and Θ is the classical deflection function (which is identical to the angle of observation). On making the correspondence

$$b\cong(l_\theta+\tfrac{1}{2})\lambda\!\!\!^{-},$$

we see that the semiclassical result of Eq. (43) is identical to the classical result of Eq. (44).

The conclusion of the equality of the semiclassical and classical cross sections requires a monotonic variation of $\Theta(l)$ with l from $\pm\pi$ (plus for repulsion, minus for attraction) to zero in order that there be only one point of stationary phase. As already remarked, this is a very special behavior which generally does not occur. We turn now to a discussion of the more common circumstance for which the approach is nonuniform, i.e., in a sense there is no approach at all. The various nonuniform features can be grouped into four categories: *inteference*, *rainbow scattering*, *the glory effect*, and *orbiting* (or *spiral scattering*).

If the classical deflection function $\Theta(l)$ is not monotonic (it usually is not), then more than one l value may contribute to the scattering at a given angle. We illustrate this in Fig. 25, following Ford and Wheeler, for two angular momenta l_1 and l_2 contributing to the scattering at one observation angle θ. The classical treatment of such a nonmonotonic deflection function is carried out by splitting $\Theta(l)$ into branches (in the case illustrated in Fig. 25, two branches) and adding up the contributions to the cross section from the separate branches:

$$d\sigma_{cl}/d\Omega=\sum_i(d\sigma_{cl}/d\Omega)_i, =(1/\sin\theta)\sum_i(b_i/|d\Theta/db|_i), \quad (45)$$

in which the subscript i means the ith branch and we have used the form of Eq. (44).

To obtain the semiclassical scattering amplitude in the case of more than one branch in the deflection function, the results of stationary phase calculations of the sort leading to Eq. (39) for each branch can be added together to give the total amplitude, providing the angular momenta at which the phase is stationary are well enough separated. (When they are not well

enough separated, we are led to the so-called *rainbow scattering* which we discuss shortly.)

It is easiest to discuss the interference phenomena by writing the amplitude, Eq. (39), and the analogous result for an attractive potential (φ_- is replaced by φ_+ and there is an additional over-all minus sign) in polar form:

$$f_{sc}(\theta)\simeq\mp\lambda\left[\frac{l_\theta+\frac{1}{2}}{\sin\theta\,|\,\varphi_\pm''(l_\theta)\,|}\right]^{\frac{1}{2}}\times\exp\left\{i\left[\varphi_\pm(l_\theta)+\frac{\pi}{4}\frac{\varphi_\pm''}{|\,\varphi_\pm''|}(l_\theta)\right]\right\}. \quad (46)$$

This can be simplified considerably by introducing the explicit expression (27) for $\varphi_\pm$. The distinction between the two types of stationary phase points is conveniently made in terms of $d\eta_l/dl\equiv\eta'$ since this is positive (equal to $\theta/2$) for repulsive scattering and negative (equal to $-\theta/2$) for attractive scattering. Thus we write from Eq. (27)

$$\varphi_\pm(l_\theta)=[2\eta-2(l+\tfrac{1}{2})\eta'-(\pi/4)\eta'/|\eta'|]_{l=l_\theta}. \quad (47)$$

In addition, the other distinguishing phase factors in Eq. (46) can be written

$$\mp1=\exp[-i(\pi/2)(1-\eta'/|\eta'|)_{l=l_\theta}],$$
$$\exp\left(i\frac{\pi}{4}\frac{\varphi_+''}{|\,\varphi_+''|}\right)=\exp\left[i\left(\frac{\pi}{4}\frac{\eta''}{|\eta''|}\right)_{l=l_\theta}\right]. \quad (48)$$

On combining Eqs. (46)–(48) we can write

$$f_{sc}\simeq\lambda\left(\frac{l_\theta+\frac{1}{2}}{2\sin\theta\,|\eta_{l_\theta}''|}\right)^{\frac{1}{2}}e^{i\beta},$$
$$\simeq(d\sigma_{cl}/d\Omega)^{\frac{1}{2}}e^{i\beta}, \quad (49)$$

where

$$\beta=\left[2\eta-2(l+\tfrac{1}{2})\eta'-\left(2-\frac{\eta''}{|\eta''|}-\frac{\eta'}{|\eta'|}\right)\frac{\pi}{4}\right]_{l=l_\theta}. \quad (50)$$

The expression Eq. (49) for the semiclassical scattering amplitude is valid for a stationary phase approximation for one branch of the classical deflection function. In the case of many branches for which the stationary phase points are well separated, the semiclassical *amplitude* is then in the stationary phase approximation a sum of *amplitudes* from the contributing branches

$$f_{sc}\simeq\sum_j(d\sigma_{cl}/d\Omega)_j^{\frac{1}{2}}e^{i\beta_j}. \quad (51)$$

This expression yields the result of Eq. (45) only in the case that no more than one branch (one term in the summation) is present. Under the circumstance that only two branches are involved, the semiclassical cross section becomes

$$d\sigma_{sc}/d\Omega=|\,(d\sigma_{cl}/d\Omega)_1^{\frac{1}{2}}+(d\sigma_{cl}/d\Omega)_2^{\frac{1}{2}}e^{i(\beta_2-\beta_1)}\,|^2. \quad (52)$$

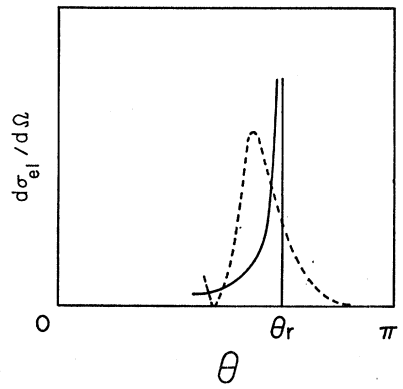

FIG. 26. Classical and semiclassical differential cross sections vs scattering angle θ near the rainbow angle θ_r. The bright and dark regions are clearly delineated by the classical cross section. ———, classical; — — —, semiclassical.

This implies an oscillation of the semiclassical cross section, as a function of angle, between the envelopes

$$(d\sigma_{sc}/d\Omega)_{max}=[(d\sigma_{cl}/d\Omega)_1^{\frac{1}{2}}+(d\sigma_{cl}/d\Omega)_2^{\frac{1}{2}}]^2, \quad (53)$$

and

$$(d\sigma_{sc}/d\Omega)_{min}=[(d\sigma_{cl}/d\Omega)_1^{\frac{1}{2}}-(d\sigma_{cl}/d\Omega)_2^{\frac{1}{2}}]^2. \quad (54)$$

The angular variation required to go through a full oscillation (maximum to minimum and back to maximum) is seen from Eq. (50) to be (since $2\eta'=\theta'$)

$$\delta\theta=2\pi/|\,l_2-l_1\,|, \quad (55)$$

with l_1 and l_2 the points of stationary phase. This assumes that $|l_2-l_1|\gg2\pi$, which is essentially an expression of the original assumption that the stationary phase points in the two branches are well separated.

This analysis shows that it is possible in principle to extract, from experimental cross section data, information regarding the separate branches of the deflection function, and to combine this information to construct the classical deflection function $\Theta(l)$. From this deflection function, it is then possible to determine the interaction potential according to unpublished work of J. A. Wheeler. The analysis so far, however, does not allow for absorption.

The phenomenon known as *rainbow scattering* occurs under the circumstance that there are at least two branches of the classical deflection function $\Theta(l)$ (e.g., as in Fig. 25), and $\Theta(l)$ is not singular. This means $\Theta(l)$ has at least one smooth maximum or minimum at which $d\Theta/dl$ vanishes. The value of Θ at the zero-slope point is known as the rainbow angle θ_r (e.g., as shown in Fig. 25). In a sense the semiclassical treatment of rainbow scattering represents an interference between two branches which are not well separated. Near the rainbow angle, it is possible to express Θ as

$$\Theta(l)=\pm\theta_r+q(l-l_r)^2 \quad (56)$$

(the $\pm\theta_r$ allows for both repulsive and attractive scat-

tering), assuming $q \neq 0$. This leads to

$$d\Theta/dl = 2q(l-l_r) = 2q[(\Theta \mp \theta_r)/q]^{\frac{1}{2}}. \quad (57)$$

Thus we write for the classical differential cross section on the *bright* side of the rainbow angle [(see Eq. (44)]

$$(d\sigma_{\rm cl}/d\Omega)(\theta) = (l_r+\tfrac{1}{2})\lambda\!\!\!^{-2}/\sin\theta_r 2|q(\theta-\theta_r)|^{\frac{1}{2}}. \quad (58)$$

On the *dark* side of the rainbow angle, the classical differential cross section vanishes—the rainbow angle represents a limiting angle for classical scattering. A qualitative sketch of this behavior is given in Fig. 26 for a repulsive potential. (The sketch indicates a drop to zero intensity on the dark side, but this is not realistic since other contributions are usually present.)

In order to carry out a semiclassical calculation of rainbow scattering, we use Eq. (56) and the connections (41) and (42) between the phase shift η_l and the classical deflection function:

$$d\eta_l/dl = \tfrac{1}{2}\Theta(l) = \pm\tfrac{1}{2}\theta_r + (q/2)(l-l_r)^2. \quad (59)$$

Integration yields

$$\eta_l = \eta_r \pm \tfrac{1}{2}\theta_r(l-l_r) + (q/6)(l-l_r)^3. \quad (60)$$

For repulsive scattering, we choose the plus sign in Eq. (60), and note also that it is the phase φ_- which is stationary in Eq. (26). This yields for the semiclassical scattering amplitude from Eq. (26)

$$f_{\rm sc} \simeq \lambda\!\!\!^{-}\left(\frac{l_r+\frac{1}{2}}{2\pi\sin\theta}\right)^{\frac{1}{2}}\int_0^\infty e^{i\varphi_-(l)}dl, \quad (61)$$

but we have from Eqs. (27) and (60)

$$\varphi_-(l) = 2\eta_l - (l+\tfrac{1}{2})\theta - \pi/4, = 2\eta_r + \theta_r(l-l_r) + (q/3)(l-l_r)^3 - (l+\tfrac{1}{2})\theta - \pi/4. \quad (62)$$

On combining Eqs. (61) and (62),

$$f_{\rm sc}(\theta) \simeq \lambda\!\!\!^{-}\left(\frac{l_r+\frac{1}{2}}{2\pi\sin\theta}\right)^{\frac{1}{2}} \exp\{i[2\eta_r - (l_r+\tfrac{1}{2})\theta_r - (\pi/4) + (l_r+\tfrac{1}{2})(\theta_r-\theta)]\}\int_{-\infty}^{+\infty} d(l-l_r) \times \exp\{i[(\theta_r-\theta)(l-l_r) + (q/3)(l-l_r)^3]\}, \quad (63)$$

in which the lower limit of the indicated integration has been set equal to $-\infty$ on the assumption that l_r is large. Equation (63) can be expressed in terms of the Airy integral

$$\mathrm{Ai}(x) = \frac{1}{2\pi}\int_{-\infty}^{+\infty} \exp[i(xu+\tfrac{1}{3}u^3)]du, \quad (64)$$

where x is defined as

$$x = (\theta_r-\theta)/q^{\frac{1}{3}}. \quad (65)$$

We have

$$f_{\rm sc}(\theta) \simeq \lambda\!\!\!^{-}[2\pi(l_r+\tfrac{1}{2})/\sin\theta]^{\frac{1}{2}} \exp\{i[2\eta_r - (l_r+\tfrac{1}{2})\theta_r + (l_r+\tfrac{1}{2})(\theta_r-\theta)]\}(1/q^{\frac{1}{3}})\,\mathrm{Ai}(x). \quad (66)$$

This yields for the semiclassical angular distribution near the rainbow angle

$$(d\sigma_{\rm sc}/d\Omega)(\theta) \simeq \lambda\!\!\!^{-2}(l_r+\tfrac{1}{2})(2\pi/\sin\theta|q|^{\frac{2}{3}})\,\mathrm{Ai}^2(x). \quad (67)$$

In order to learn the qualitative behavior of the semiclassical cross section, it is convenient to express the Airy integral in terms of Bessel functions and to use well-known properties of them:

$$\mathrm{Ai}(x) = \begin{cases} (1/3^{5/6}\pi)x^{\frac{1}{2}}K_{\frac{1}{3}}(2x^{\frac{3}{2}}/3), & x>0 \\ (1/3^{\frac{1}{3}})(-x)^{\frac{1}{2}}\{J_{\frac{1}{3}}[2(-x)^{\frac{3}{2}}/3] + J_{-\frac{1}{3}}[2(-x)^{\frac{3}{2}}/3]\}, & x<0. \end{cases} \quad (68)$$

For large and small $|x|$, the proper limiting formulas for $\mathrm{Ai}(x)$ are

$$\mathrm{Ai}(x) \underset{|x|\to 0}{\to} \frac{\Gamma(\frac{4}{3})}{3^{5/6}(2\pi)} - \frac{\Gamma(\frac{2}{3})}{3^{1/6}(2\pi)}x + \cdots,$$

$$\mathrm{Ai}(x) \underset{x\to-\infty}{\to} \frac{\cos[\frac{2}{3}(-x)^{\frac{3}{2}} - \pi/4]}{\pi^{\frac{1}{2}}(-x)^{\frac{1}{4}}}, \quad (69)$$

$$\mathrm{Ai}(x) \underset{x\to+\infty}{\to} \frac{\exp(-2x^{\frac{3}{2}}/3)}{2\pi^{\frac{1}{2}}x^{\frac{1}{4}}}.$$

The dashed curve in Fig. 26, indicates the behavior of the semiclassical approximation. On the dark side of the rainbow angle, there is an exponential decrease in the cross section following Eq. (69) for $x \to +\infty$, while on the bright side, the semiclassical expression oscillates about the classical value. In fact, since the average value of cosine squared is one-half, we have from Eq. (65)

$$\langle \mathrm{Ai}^2(x)\rangle \underset{x\to-\infty}{\to} [1/2\pi^{\frac{1}{2}}(-x)^{\frac{1}{4}}]^2, \quad (70)$$

so that on the bright side of the rainbow angle

$$\left\langle \frac{d\sigma_{\rm sc}}{d\Omega}(\theta)\right\rangle \simeq \lambda\!\!\!^{-2}(l_r+\tfrac{1}{2})\frac{2\pi}{\sin\theta|q|^{\frac{2}{3}}}\frac{1}{4\pi|(\theta-\theta_r)/q^{\frac{1}{3}}|^{\frac{1}{2}}}, \simeq \frac{(l_r+\frac{1}{2})\lambda\!\!\!^{-2}}{\sin\theta 2|q(\theta-\theta_r)|^{\frac{1}{2}}}, \quad (71)$$

in agreement with Eq. (58). [It is important to note that q, which first enters in Eq. (56), may be negative so that the phases in the argument of the Airy function come out properly.] The behavior here is reminiscent of the diffraction of light by a half-space. Both the rapid decrease on the dark side and the oscillation about the classical result on the bright side are characteristic features.

The contribution to the total elastic cross section arising from rainbow scattering is finite both classically and semiclassically since the scattering angle is at most π. The maximum classical contribution from the rainbow effect is

$$\begin{aligned}\sigma_{\mathrm{cl}}{}^{\max}&=4\pi\lambda\!\!\!^{-}_r{}^2|q\theta_r|^{\frac{1}{2}},\\ &\leqslant 4\pi\lambda\!\!\!^{-}_r{}^2|q_\pi|^{\frac{1}{2}},\end{aligned}\tag{72}$$

and the maximum semiclassical contribution does not differ from this very markedly.

The *glory effect*[2] is intimately associated with the dimensionality of the scattering and does not occur in two-dimensional scattering. This effect arises from the possibility that $\sin\Theta$, coming from the three-dimensional solid angle, which enters in Eq. (44), vanishes. This can occur for forward ($\Theta=0,\ \pm2\pi$, etc.) or backward ($\Theta=\pm\pi,\ \pm3\pi$, etc.) scattering: Following Ford and Wheeler, we consider for definiteness a backward glory ($\Theta=\pi$). In the neighborhood of π, we write for Θ

$$\Theta(l)=\pi+a(l-l_g),\tag{73}$$

where l_g is the glory angular momentum. Contributions to the classical cross section arise from values of Θ on both sides of π, i.e., since

$$|d\Theta/dl|_{l=l_g}=|a|,\tag{74}$$

and

$$\sin\Theta\simeq\pi-\Theta,\tag{75}$$

as $\theta\longrightarrow\pi-\epsilon$,

$$(d\sigma_{\mathrm{cl}}/d\Omega)(\theta)=2[\lambda\!\!\!^{-}{}^2 l_g/|a|(\pi-\theta)].\tag{76}$$

To obtain the semiclassical expression for the backward glory, we first determine the phase shift as a function of angular momentum l for l near l_g by integrating Eq. (73). This gives

$$\eta(l)=\eta_g+(\pi/2)(l-l_g)+(a/4)(l-l_g)^2.\tag{77}$$

Since we are now dealing with angles near π, it is no longer appropriate to use the approximation (25) for the Legendre function. Instead we use (58, p. 157)

$$P_l(\cos\theta)\simeq(\cos\theta)^l J_0[(l+\tfrac{1}{2})\theta].\tag{78}$$

On omitting the forward delta function, the semiclassical scattering amplitude, Eq. (21), is expressed as

$$f_{\mathrm{sc}}(\theta)\simeq\frac{\lambda\!\!\!^{-}}{2i}\exp[i(2\eta_g-\pi l_g)]\int_0^\infty dl(2l+1)\times\exp\left[\frac{a}{i2}(l-l_g)^2\right]J_0(l\sin\theta),\tag{79}$$

in which we have replaced θ by $\sin\theta$ in the Bessel function. The major contribution to the integral in Eq. (79) comes from $l\simeq l_g$. We change variables to

$$q=(|a|/2)^{\frac{1}{2}}(l-l_g)$$

so that

$$\begin{aligned}&\int^\infty dl(2l+1)\exp\left[\frac{a}{i2}(l-l_g)^2\right]J_0(l\sin\theta)\\ &=\left(\frac{2}{|a|}\right)^{\frac{1}{2}}\int_{-l_g(|a|/2)^{\frac{1}{2}}}^\infty dq\left\{2\left[\left(\frac{2}{|a|}\right)^{\frac{1}{2}}q+l_g\right]+1\right\}\\ &\quad\times\exp\left(iq^2\frac{a}{|a|}\right)J_0\left\{\left[\left(\frac{2}{|a|}\right)^{\frac{1}{2}}q+l_g\right]\sin\theta\right\}.\end{aligned}\tag{80}$$

For large $l_g(|a|/2)^{\frac{1}{2}}$, this becomes approximately

$$\begin{aligned}&\int_0^\infty dl(2l+1)\exp\left[\frac{a}{i2}(l-l_g)^2\right]J_0(l\sin\theta)\\ &\simeq\left(\frac{2}{|a|}\right)^{\frac{1}{2}}(2l_g+1)J_0(l_g\sin\theta)\int_{-\infty}^{+\infty}dq\exp\left(iq^2\frac{a}{|a|}\right),\\ &\simeq\left(\frac{2}{|a|}\right)^{\frac{1}{2}}(2l_g+1)J_0(l_g\sin\theta)\pi^{\frac{1}{2}}\exp\left(\frac{\pi}{i4}\frac{a}{|a|}\right),\end{aligned}\tag{81}$$

in which the sign $a/|a|$ of a is explicitly indicated. This gives finally for the semiclassical scattering amplitude

$$f_{\mathrm{sc}}\simeq\lambda\!\!\!^{-}\exp\left[i\left(2\eta_g-\pi l_g+\frac{\pi}{4}\frac{a}{|a|}-\frac{\pi}{2}\right)\right]\times(2\pi/|a|)^{\frac{1}{2}}(l_g+\tfrac{1}{2})J_0(l_g\sin\theta).\tag{82}$$

From this approximation to the amplitude, the resulting semiclassical cross section is

$$\begin{aligned}\frac{d\sigma_{\mathrm{sc}}}{d\Omega}(\theta)&\simeq\lambda\!\!\!^{-}{}^2(l_g+\tfrac{1}{2})^2\frac{2\pi}{|a|}J_0{}^2(l_g\sin\theta),\\ &\underset{\theta\to\pi}{\longrightarrow}\lambda\!\!\!^{-}{}^2(l_g+\tfrac{1}{2})\frac{2\pi}{|a|}.\end{aligned}\tag{83}$$

Thus the classical singularity is replaced by a finite peak. In addition, since asymptotically

$$\langle J_0{}^2(z)\rangle=1/\pi z,\tag{84}$$

we find

$$\left\langle\frac{d\sigma_{\mathrm{sc}}}{d\Omega}(\theta)\right\rangle\simeq\lambda\!\!\!^{-}{}^2 l_g\frac{2}{|a|}\frac{1}{\pi-\theta},\tag{85}$$

which is identical to the classical result, Eq. (76). A qualitative sketch is given in Fig. 27.

The maximum contribution of the glory effect to the total elastic cross section is most easily estimated from Eq. (76). We have

$$\sigma_{\mathrm{el}}{}^{\max}\simeq4\pi\lambda\!\!\!^{-}{}^2\frac{l_g}{|a|}\int_{\theta_1}^\pi\frac{\sin\theta d\theta}{\pi-\theta},\tag{86}$$

[2] *Note added in proof.* The proper description of glory scattering is still a matter of debate (S. I. Rubinow, private communication). Although we have followed the Ford-Wheeler treatment because of its ready availability, we do not wish to mislead the reader in this respect.

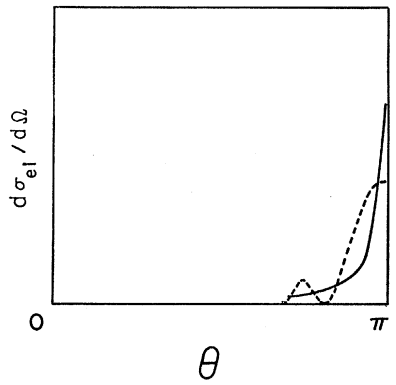

FIG. 27. Classical and semiclassical differential cross sections vs scattering angle θ near $\theta=\pi$ for a backward glory. ———, classical; — — —, semiclassical.

where θ_1 is the angle beginning at which the differential cross section is primarily the result of the backward glory. [A natural choice for θ_1 might be the first zero of $J_0(l_g \sin\theta)$ so that θ_1 depends upon l_g.] We find from Eq. (86)

$$\sigma_{el}{}^{max} \simeq 4\pi\chi^2 \frac{l_g}{|a|} \int_0^{\pi-\theta_1} \frac{\sin\gamma}{\gamma} d\gamma, \qquad (87)$$
$$\simeq 4\pi\chi^2 (l_g/|a|)(\pi-\theta_1).$$

We have assumed here that θ_1 is close to π.

So far we have considered only nonsingular classical deflection functions $\Theta(l)$. *Spiral scattering* or *orbiting* involves a singularity of $\Theta(l)$. Recalling from Eq. (31) that the coordinate angle χ and radial position r of a particle are related via

$$\chi(r)-\chi_0 = \int_{r_0}^{r} \frac{l dr'}{r'^2[k^2-U_{eff}(r',l)]^{\frac{1}{2}}}, \qquad (88)$$

where

$$k^2 = 2mE/\hbar^2$$
$$U_{eff}(r,l) = [2mV(r)/\hbar^2] + (l^2/r^2), \qquad (89)$$
$$= U(r) + (l^2/r^2).$$

In Eqs. (88) and (89), although the replacement of L by $l\hbar$ has been made, the expressions are purely classical. If $U_{eff}(r,l)$ is such that for some value r_1 of r and some value l_1 of l

$$(dU_{eff}/dr)(r_1,l_1)=0, \quad U_{eff}(r_1,l_1)=k^2, \qquad (90)$$

then the phenomenon of *orbiting* appears. It is clear that special care is needed under these conditions. Following the sketches in Fig. 24, we can also sketch χ as a function of r, as in Fig. 28. The deflection function $\Theta(l)$ is obtained according to Eq. (35).

We consider a potential such that $U_{eff}(r,l)$ has the qualitative structure indicated in Fig. 29. The classical turning points (coordinate r_0) are indicated as black spots in Fig. 29 and satisfy

$$U_{eff}(r_0,l)=k^2, \qquad (91)$$

so that r_0 depends on l. For $l \simeq l_1$, the phenomenon of spiral scattering occurs and is associated with the appearance of two turning points. To obtain the deflection function from Eq. (35), we need

$$\chi_\infty - \chi_0 = \int_{r_0(l)}^{\infty} \frac{l dr'}{r'^2[k^2-U_{eff}(r',l)]^{\frac{1}{2}}}. \qquad (92)$$

At an ordinary classical turning point, the integrand is singular, but the singularity is integrable; however, when a turning point falls into the category of Eq. (90), then even the integral is singular. For this reason, we argue that the behavior of Eq. (92) for l near l_1 can be determined by picking up the singular contributions. We expand the integrand about the turning point $r_0(l)$, examining carefully the behavior of $r_0(l)$ to see how to make the desired expansions. From Eq. (91),

$$k^2 - U(r_0) - l^2/r_0^2 = 0. \qquad (93)$$

If we consider the inverse function $l(r_0)$ instead of $r_0(l)$, we have

$$l(r_0) = r_0[k^2-U(r_0)]^{\frac{1}{2}}. \qquad (94)$$

Differentiating this function gives

$$\frac{dl}{dr_0} = \frac{k^2-U(r_0)-\frac{1}{2}r_0U'(r_0)}{[k^2-U(r_0)]^{\frac{1}{2}}}. \qquad (95)$$

But from Eq. (90),

$$U'(r_1)-(2l_1^2/r_1^3)=0, \quad k^2-U(r_1)-(l^2/r_1^2)=0, \qquad (96)$$

or

$$k^2-U(r_1)-\tfrac{1}{2}r_1U'(r_1)=0. \qquad (97)$$

Hence from Eqs. (95) and (97),

$$(dl/dr_0)(r_0=r_1)=0. \qquad (98)$$

At $r_0=r_2$, there is not a similar special type of behavior. We are thus led to sketch $r_0(l)$ as in Fig. 30. We can therefore expand about $r_0=r_1$ for $l>l_1$ and about $r_0=r_2$ for $l<l_1$, but the discontinuous region is ruled out.

On considering first $l>l_1$, we have

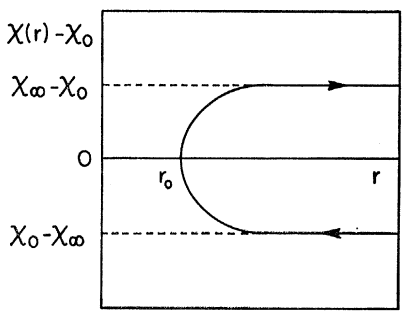

FIG. 28. Coordinate angle $\chi(r)-\chi_0$ as a function of radial position r along the orbit as indicated in Fig. 24.

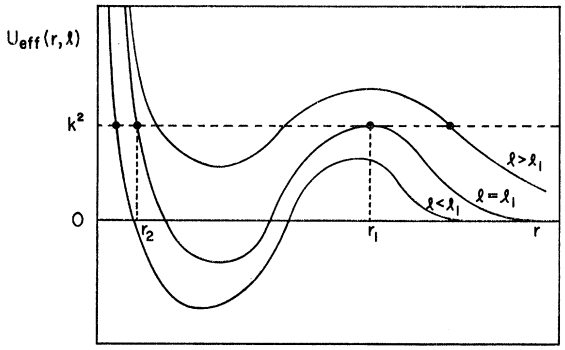

FIG. 29. Effective potential $U_{\text{eff}}(r,l)$ as a function of radius r for various values of the angular momentum l. The angular momentum l_1 characteristic of spiral scattering is indicated along with the corresponding turning points r_1 and r_2. Other turning points for "energy" k^2 are indicated by solid dots.

$$l(r_0)=l_1+\frac{dl}{dr_0}(r_1)(r_0-r_1)+\frac{d^2l}{dr_0^2}(r_1)\frac{(r_0-r_1)^2}{2}+\cdots$$
$$=l_1+l''(r_1)\frac{(r_0-r_1)^2}{2}+\cdots. \tag{99}$$

Therefore, if we reverse this expansion,

$$r_0(l)=r_1+[2(l-l_1)/|l''(r_1)|]^{\frac{1}{2}}+\cdots. \tag{100}$$

The branch point is important; it gives the infinite slope.

To see that there is nothing additionally peculiar, we can calculate $l''(r)$ from Eq. (95):

$$l''(r_1)=-\tfrac{1}{2}[r_1U'(r_1)]^{\frac{1}{2}}[3U'(r_1)+r_1U''(r')]. \tag{101}$$

Most likely this is not zero or infinity. From Figs. 29 and 30, we see that for $l\rightarrow l_1^-$, we have to integrate in Eq. (92) from r_2 to infinity; in this case because of the corner at the point (r_2,l_1) in Fig. 30, the major contribution to the singular part of the integral does not come from $r\simeq r_2$, but rather from $r\simeq r_1$. In this case, contributions arise for $r<r_1$ and $r>r_1$. We therefore must consider two cases separately, that for which $l\rightarrow l_1^+$ and the singular contribution arises near the turning point r_1 and only for $r>r_1$, and that for which $l\rightarrow l_1^-$ and the singular contribution does not arise near the turning point r_2 but near the point r_1 (which is in the "middle" of the region of integration) and for which both the regions $r<r_1$ and $r>r_1$ contribute.

In the case $l\rightarrow l_1^+$, we expand near the singular region $(r\simeq r_1)$ in the integrand:

$$k^2-U_{\text{eff}}(r,l)=k^2-U_{\text{eff}}(r_1,l)-U_{\text{eff}}'(r_1,l)(r-r_1)$$
$$-U_{\text{eff}}''(r_1,l)\tfrac{1}{2}(r-r_1)^2+\cdots, \tag{102}$$
$$\underset{l\rightarrow l_1^+}{\simeq}-U_{\text{eff}}''(r_1,l_1)\tfrac{1}{2}(r-r_1)^2+\cdots,$$

where we have used Eq. (90). From Eq. (92) we find

$$\chi_\infty-\chi_0\simeq\int_{r_0}^{\infty}\frac{l\,dr'}{r'^2[-U_{\text{eff}}''(r_1,l_1)\tfrac{1}{2}(r-r_1)^2]^{\frac{1}{2}}},$$
$$\simeq\frac{l}{[-\tfrac{1}{2}U_{\text{eff}}''(r_1,l_1)]^{\frac{1}{2}}}$$
$$\times\int_{r_1+[2(l-l_1)/|l''(r_1)|]^{\frac{1}{2}}}^{\infty}\frac{dr'}{r'^2}\frac{1}{r'-r_1}. \tag{103}$$

On letting $y=r'/r_1$, we have

$$\chi_\infty-\chi_0\simeq\frac{l}{[-\tfrac{1}{2}r_1''U_{\text{eff}}''(r_1,l_1)]^{\frac{1}{2}}}$$
$$\times\int_{1+[2(l-l_1)/r_1^2|l''(r_1)|]^{\frac{1}{2}}}^{\infty}\frac{dy}{y^2(y-1)}. \tag{104}$$

This becomes

$$\chi_\infty-\chi_0\simeq\frac{l}{[-\tfrac{1}{2}r_1^4U_{\text{eff}}''(r_1,l_1)]^{\frac{1}{2}}}\left[\frac{-1}{1+\xi}-\log\frac{\xi}{1+\xi}\right], \tag{105}$$

with

$$\xi=[2(l-l_1)/r_1^2|l''(r_1)|]^{\frac{1}{2}}. \tag{106}$$

For $l\rightarrow l_1^+(\xi\rightarrow 0)$, we find

$$\chi_\infty-\chi_0\underset{l\rightarrow l_1^+}{\rightarrow}\frac{l_1}{[-\tfrac{1}{2}r_1^4U_{\text{eff}}''(r_1,l_1)]^{\frac{1}{2}}}[-1-\log\xi],$$
$$\underset{l\rightarrow l_1^+}{\rightarrow}\frac{l_1}{[-\tfrac{1}{2}r_1^4U_{\text{eff}}''(r_1,l_1)]^{\frac{1}{2}}}$$
$$\times\left[-1-\tfrac{1}{2}\log\frac{2l_1}{r_1^2|l''(r_1)|}+\tfrac{1}{2}\log\frac{l_1}{l-l_1}\right]\cdots. \tag{107}$$

The deflection function $\Theta(l)$ is from the first of Eqs. (34) (the potential is repulsive for $l>l_1$):

$$\Theta(l)=\pi-2(\chi_\infty-\chi_0),\ \underset{l\rightarrow l_1^+}{\rightarrow}-\Theta_1-b\log\frac{l_1}{l-l_1}, \tag{108}$$

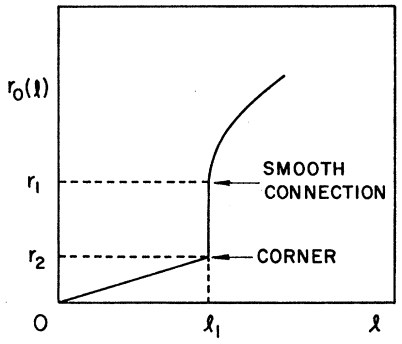

FIG. 30. The classical turning point as a function of angular momentum l.

with

$$\Theta_1=-\pi+\left[\frac{2l_1^2}{-r_1^4U_{\text{eff}}''(r_1,l_1)}\right]^{\frac{1}{2}}\left[\log\frac{r_1^2|l_1''(r_1)|}{l_1}-2\right],$$

$$b=[2Ul_1(r_1)/-r_1^2U_{\text{eff}}''(r_1,l_1)]^{\frac{1}{2}}, \tag{109}$$

and $Ul_1(r_1)=l_1^2/r_1^2$ is the centripetal potential. From Eq. (108) we see clearly the logarithmic singularity.

In the case $l\to l_1^-$, we proceed similarly, but must now integrate over both sides of r_1. We have

$$k^2-U_{\text{eff}}(r,l)=k^2-U_{\text{eff}}(r_1,l_1)-U_{\text{eff}}'(r_1,l)(r-r_1)-U_{\text{eff}}''(r_1,l)\tfrac{1}{2}(r-r_1)^2+\cdots. \tag{110}$$

We need the dependence of the coefficients on l for $l\to l_1^-$. Since

$$k^2-U_{\text{eff}}(r_1,l)=k^2-U(r_1)-l^2/r_1^2, \tag{111}$$

we have

$$\frac{\partial U_{\text{eff}}}{\partial l}(r_1,l)\underset{l\to l_1}{\to}\frac{2l_1}{r_1^2},$$

$$\frac{\partial U_{\text{eff}}'}{\partial l}(r_1,l)\underset{l\to l_1}{\to}-\frac{4l_1}{r_1^3}, \tag{112}$$

$$\frac{\partial U_{\text{eff}}''}{\partial l}(r_1,l)\underset{l\to l_1}{\to}+\frac{12l_1}{r_1^4}.$$

Hence we find

$$k^2-U_{\text{eff}}(r,l)\simeq-\frac{2l_1}{r_1^2}(l-l_1)+\frac{4l_1}{r_1^3}(l-l_1)(r-r_1)-U_{\text{eff}}''(r_1,l_1)\tfrac{1}{2}(r-r_1)^2+\cdots. \tag{113}$$

This result holds for l on either side of l_1. Inserting this expression into $\chi_\infty-\chi_0$ yields

$$\chi_\infty-\chi_0=\int_{r_0}^{\infty}\frac{ldr'}{r'^2[k^2-U_{\text{eff}}(r',l)]^{\frac{1}{2}}}$$

$$\simeq\int_{r_2}^{\infty}ldr'\Big/r'^2\left[-\frac{2l_1}{r_1^2}(l-l_1)+\frac{4l_1}{r_1^3}(l-l_1)(r'-r_1)-U_{\text{eff}}''(r_1,l_1)\tfrac{1}{2}(r'-r_1)^2\right]^{\frac{1}{2}}. \tag{114}$$

If we introduce the variable $y=r'/r_1$, then

$$\chi_\infty-\chi_0\simeq\frac{l}{[-\frac{1}{2}r_1^4U_{\text{eff}}''(r_1,l_1)]^{\frac{1}{2}}}\int_{r_2/r_1}^{\infty}\frac{dy}{y^2}\left[\frac{4l_1(l-l_1)}{r_1^4U_{\text{eff}}''(r_1,l_1)}-\frac{8l_1(l_1-l)}{r_1^4U_{\text{eff}}''(r_1,l_1)}(y-1)+(y-1)^2\right]^{-\frac{1}{2}}. \tag{115}$$

If we let

$$\eta=4l_1(l_1-l)/[-r_1^4U_{\text{eff}}''(r_1,l_1)],$$

then

$$\chi_\infty-\chi_0\simeq\frac{l}{[-\frac{1}{2}r_1^4U_{\text{eff}}''(r_1,l_1)]^{\frac{1}{2}}}\times\int_{r_2/r_1}^{\infty}\frac{dy}{y^2}\frac{1}{[(y-1)^2-2\eta(y-1)+\eta]^{\frac{1}{2}}}. \tag{116}$$

We need, therefore,

$$\int_{r_2/r_1}^{\infty}\frac{dy}{y^2}\frac{1}{[y^2-2(1+\eta)y+1+3\eta]^{\frac{1}{2}}}=-\frac{1}{1+3\eta}-\frac{1+\eta}{(1+3\eta)^{\frac{3}{2}}}\log\left[1-\frac{1+\eta}{(1+3\eta)^{\frac{1}{2}}}\right] \tag{117}$$

plus nonsingular terms in η and r_2/r_1. As $\eta\to0$ ($l\to l_1^-$), this becomes

$$\int_{r_2/r_1}^{\infty}\frac{dy}{y^2}\frac{1}{[y^2-2(1+\eta)y+1+3\eta]^{\frac{1}{2}}}\underset{\eta\to0}{\to}-\log\frac{\eta}{2}+\text{const}, \tag{118}$$

or the deflection function is

$$\Theta(l)\underset{l\to l_1^-}{\to}\Theta_2-2b\log\frac{l_1}{l_1-l}, \tag{119}$$

with

$$b=\{2Ul_1(r_1)/[-r_1^2U_{\text{eff}}''(r_1,l_1)]\}, \tag{120}$$

as in (109), and Θ_2 dependent upon r_2/r_1 (the potential inside of the barrier) as indicated in Eq. (117).

We have therefore exhibited the nature of the singularity in the classical deflection function in the case of *orbiting*. This behavior is sketched in Fig. 31, for a potential such that $\Theta(0)=\pi$, i.e., a net repulsion. The phase shift η_l near l_1, has infinite slope and undergoes a discontinuity of less than π at $l=l_1$. The presence of the barrier means that the possibility of virtual levels exists, so that η_l may have discontinuities of π at other l's corresponding to passing through such levels (or resonances).

To obtain the classical cross section arising from orbiting, it is necessary to note that it consists of a number of contributions arising from the intervals $\Theta=0$ to $-\pi$, $\Theta=-\pi$ to -2π, etc. These contributions become progressively smaller so we shall be content

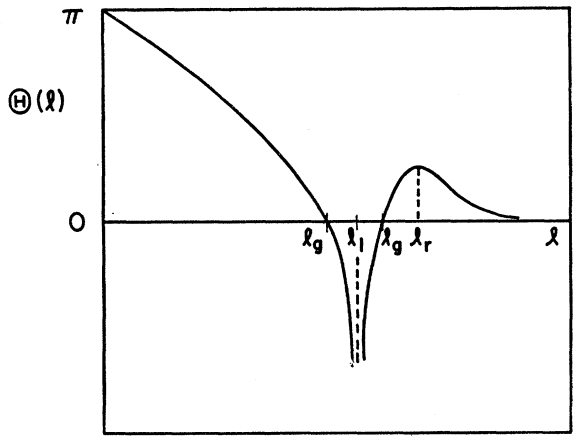

FIG. 31. Classical deflection function $\Theta(l)$ as a function of angular momentum l for a repulsive potential. The rainbow angular momentum l_r, the orbiting angular momentum l_1, and the glory angular momentum l_g are indicated.

with only the first interval. Here we find

$$\frac{d\Theta}{dl}=\begin{cases}-2b/(l_1-l), & l<l_1\\ +b/(l-l_1) & l>l_1,\end{cases}$$
$$=\begin{cases}-(2b/l_1)\exp[-(\Theta+\Theta_2)/2b], & l<l_1\\ (b/l_1)\exp[-(\Theta+\Theta_1)/b], & l>l_1.\end{cases} \quad (121)$$

For the angle of observation in this case,

$$\Theta=-\theta, \quad \Theta_1=-\theta_1, \quad \Theta_2=-\theta_2, \quad (122)$$

so that

$$\frac{d\sigma_{\rm cl}}{d\Omega}=\lambda\!\!\!^{-2}(l_1+\tfrac{1}{2})^2\frac{1}{b\sin\theta}$$
$$\times\left\{\exp\left[-\frac{(\theta+\theta_1)}{b}\right]+\tfrac{1}{2}\exp\left[-\frac{(\theta+\theta_2)}{2b}\right]\right\}$$
$$+\text{terms from }\Theta=-\pi\text{ to }-2\pi,\text{ etc.} \quad (123)$$

There is no simple general semiclassical discussion of spiral scattering analogous to the preceding discussions. Under certain special cases, some additional comments can be made (13).

Following their paper concerning the general semiclassical analysis of scattering, Ford and Wheeler make application of these results to a number of problems (13).

The point of view taken by them is that, despite the large alpha-particle absorption indicated for orbits which pass through any appreciable thickness of nuclear matter, for orbits in the weakly absorbing surface of the nucleus, which are assumed to be most directly associated with the rapid departure from Coulomb scattering, the semiclassical no-absorption rainbow scattering analysis represents a valid starting point.

Ford and Wheeler represent the target nucleus by a real potential indicated qualitatively in Fig. 32. This potential is assumed to have a Coulomb tail $2Ze^2/r$ and an attractive central region. The classical deflection function for such a potential is also indicated in Fig. 32. The classical behavior of $\Theta(l)$ may be described by saying that as the collision becomes closer ($l\to l_r^+$) the rainbow phenomenon appears and for even closer collisions ($l\to l_1^+$), spiral scattering occurs until finally for head-on collisions ($l\to 0$), there is no deflection at all. Since spiral scattering occurs near the surface of the strictly nuclear potential, it is clear that the rainbow orbit only grazes the edge of the nucleus since it is further out ($l_r>l_1$). Thus it seems reasonable to say that absorption may begin to be important only for those orbits $l\lesssim l_1$, since they pass through a large thickness of nuclear matter.

The treatment of the rainbow scattering is identical to that following Eq. (56). The deflection function is written in parabolic approximation near l_r as

$$\Theta=\theta_r-q(l-l_r)^2. \quad (124)$$

The explicit minus sign in front of q is helpful here. Near the rainbow angle, we have from Eq. (67)

$$\frac{d\sigma_{\rm sc}}{d\Omega}(\theta)\simeq\lambda\!\!\!^{-2}(l_r+\tfrac{1}{2})\frac{2\pi}{\sin\theta}\frac{1}{q^{\frac{2}{3}}}\mathrm{Ai}^2\left(\frac{\theta-\theta_r}{q^{\frac{1}{3}}}\right). \quad (125)$$

Ford and Wheeler next make what may be a questionable argument. The small angle scattering arises from head-on collisions ($l\to 0$), from large impact parameter collisions ($l\to\infty$), and also from the glory scattering ($l_1<l_g<l_r$). They argue that most of the small angle scattering arises from the $l=0$ orbits and that since these orbits are strongly absorbed in actuality [absorp-

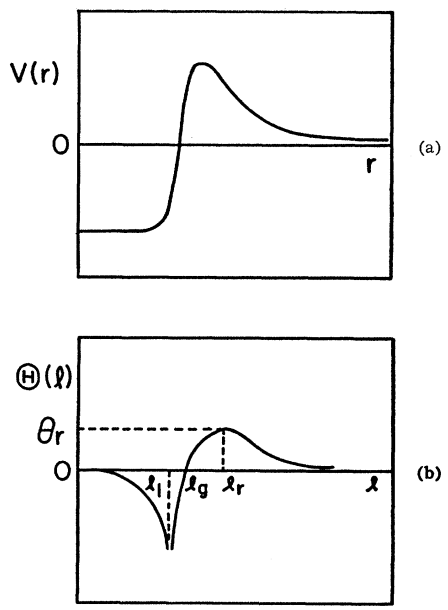

FIG. 32. (a) An attractive potential $V(r)$ containing a barrier and (b) the corresponding classical deflection function $\Theta(l)$. This is the type of real potential used by Ford and Wheeler for alpha-particle scattering.

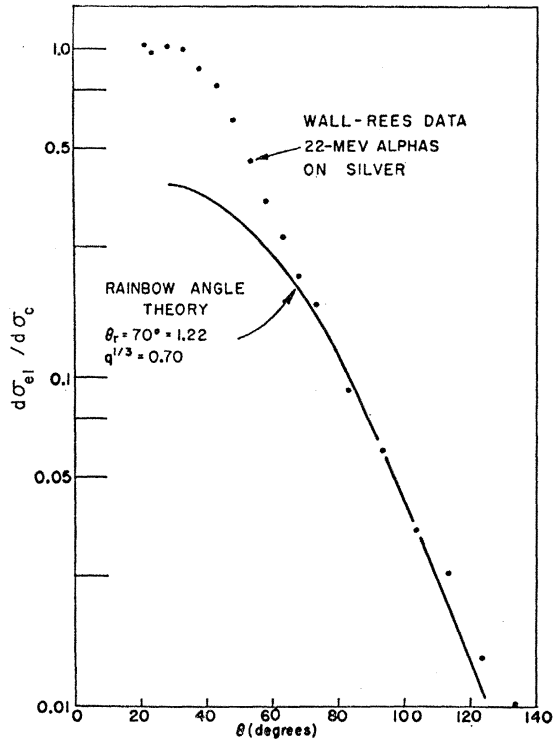

FIG. 33. Ratio of the elastic scattering cross section to the Coulomb cross section as a function of scattering angle. Points show experimental data for 22-Mev alpha particles incident on Ag. Solid curve is the prediction of the rainbow angle theory for a rainbow angle θ_r of 70° and a surface thickness parameter q such that $q^{\frac{1}{3}}=0.70$.

tion is neglected in Eq. (125)] it is natural to conclude that Eq. (125) is more valid for large angles ($\theta>\theta_r$) than for small angles ($\theta<\theta_r$). Thus they do not expect the oscillating behavior on the bright side of the rainbow angle to match with Eq. (125) since it is expected to be strongly damped. The net result is to avoid the standard procedure of normalizing the average intensity on the bright side of the rainbow angle. This seems to be open to question.

In order to obtain the ratio to the Coulomb cross section, we divide Eq. (125) by the standard formula for point Coulomb scattering of alpha particles. From the relation between the impact parameter $b\simeq(l+\frac{1}{2})\lambda\!\!\!^{-}$ and the angle for Coulomb scattering (19, p. 84):

$$(l+\tfrac{1}{2})\lambda\!\!\!^{-}\simeq(2Ze^2/mv^2)\cot(\theta/2), \tag{126}$$

or

$$(l_r+\tfrac{1}{2})\tan(\theta_r/2)\simeq n, \tag{127}$$

with $n=2Ze^2/\hbar v$. Thus the ratio to Coulomb near the rainbow angle is

$$\frac{d\sigma_{sc}}{d\sigma_c}=\frac{l_r+\frac{1}{2}}{\sin\theta_r}\frac{4\sin^4(\theta_r/2)}{n^2}\frac{2\pi}{q^{\frac{2}{3}}}\mathrm{Ai}^2\left(\frac{\theta-\theta_r}{q^{\frac{1}{3}}}\right),$$

$$=\frac{2\sin^2(\theta_r/2)}{nq^{\frac{2}{3}}}2\pi\,\mathrm{Ai}^2\left(\frac{\theta-\theta_r}{q^{\frac{1}{3}}}\right). \tag{128}$$

TABLE I.

E, Mev	Element	θ_r, deg	l_r	q	$\Delta R(10^{-13}$ cm)
22	$_{47}$Ag	70	9.0	0.34	0.93
40	$_{73}$Ta	43	18.5	0.0425	1.5
40	$_{90}$Th	53	17.9	0.0494	1.6

On the dark side of the rainbow angle, this ratio falls off exponentially. From Eq. (69), we have

$$\frac{d\sigma_{sc}}{d\sigma_c}\underset{\theta\gg\theta_r}{\longrightarrow}\frac{\sin^2(\theta_r/2)}{nq^{\frac{1}{2}}}\frac{\exp[-(4/3q^{\frac{1}{2}})(\theta-\theta_r)^{\frac{3}{2}}}{(\theta-\theta_r)^{\frac{1}{2}}}. \tag{129}$$

This yields a simple formula appropriate to the logarithmic plot for $(\theta-\theta_r)/q^{\frac{1}{2}}>1$:

$$\frac{d}{d\theta}\left[\log\left(\frac{d\sigma_{sc}}{d\sigma_c}\right)\right]\simeq-\tfrac{1}{2}(\theta-\theta_r)-2\left(\frac{\theta-\theta_r}{q^{\frac{1}{2}}}\right)^{\frac{1}{2}}. \tag{130}$$

The Ford-Wheeler model for alpha scattering thus contains two parameters, the rainbow angle θ_r and the curvature q. The parameter q is interpreted by them as a measure of the thickness ΔR of the surface transition region via the arbitrary connection

$$\begin{aligned} q&=\theta_r/(\Delta l)^2,\\ &=\theta_r(\lambda\!\!\!^{-}/\Delta R)^2. \end{aligned} \tag{131}$$

A typical reconciliation of the rainbow angle theory and experimental data is shown in Fig. 33 for 22-Mev alpha particles incident on Ag (59). The rainbow angle in this case turns out to be 70° (1.22 rad) and the curvature parameter is such that $q^{\frac{1}{3}}=0.70$. From (131), this implies a transition width in l units of $\Delta l\simeq 2$. This figure is an example of the emphasis on fitting the dark ($d\sigma_{sc}/d\sigma_c<0.1$) rather than the bright side of the rainbow angle. If the theoretical curve were adjusted to match the cross section in the region $(d\sigma_{sc}/d\sigma_c)\simeq 1$, then the falloff at the rainbow angle would be nearly vertical. Ford and Wheeler prefer to write off this difficulty on the bright side as arising from the absorption of small angle scattering, which is admittedly omitted from the zeroth-order rainbow model. Similar fits to other elements yield results given in Table I reproduced from the Ford-Wheeler paper.

The authors are careful to point out that these parameters are intended to be interpreted only qualitatively, since the theoretical curves tend to drop a little more rapidly than the data in some cases.

In order to provide a more severe test of the rainbow approximation, Ford and Wheeler consider the scattering of 48-Mev alpha particles by Pb (11). They take for the potential at the edge of the nucleus four times the nucleon-nucleus potential (38). Thus they chose

$$V(r)=\frac{160}{1+\exp[(r-R)/d]}\text{ Mev}, \tag{132}$$

with $R=1.33A^{\frac{1}{3}}\times10^{-13}$ cm and $d=0.5\times10^{-13}$ cm. The classical deflection function for this potential plus the Coulomb potential is shown in Fig. 34. Only deflections for $l>l_1$ are included in keeping with the no-absorption features of the potential. The rainbow angle is 30° and occurs at $l_r=25.5$ The angular momentum l_1, characteristic of the orbiting phenomenon is $l_1=22.5$. The orbiting region is very narrow and, because of the flat character of the deflection function near the rainbow angle, a parabolic fit to the curve is not very good.

In Fig. 35 the classical cross section corresponding to the deflection function of Fig. 34 is shown along with several other curves. Among these curves is the parabolic rainbow approximation based on the parameters associated with the deflection function of Fig. 34: $l_r=25.5$, $\theta_r=30.6°$, and $q=0.00680$. The rapid failure of this approximation as l deviates from l_r is at best partly responsible for the poor fit to the experimental data in Fig. 35. A modification of the rainbow approximation based on a better empirical curve fit to the deflection function of Fig. 34 is also shown in Fig. 35. The sharp angular momentum cutoff at $l\simeq l_1$ leads to too high a predicted cross section at backward angles much like the (expected) failure of the Blair calculations.

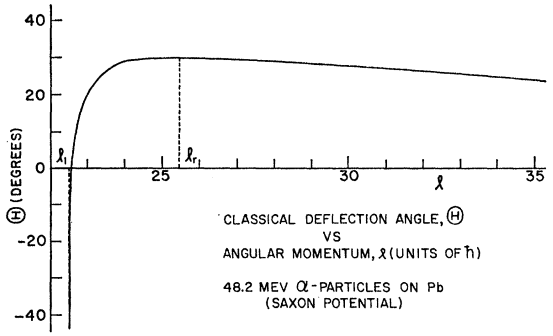

FIG. 34. Classical deflection function Θ against angular momentum l for angular momenta greater than the orbiting angular momentum l_1. The curve corresponds to the Saxon potential plus the Coulomb potential as used by Ford and Wheeler to obtain the classical angular distribution shown in Fig. 35.

In addition, two curves labeled "gradual absorption" are also presented in Fig. 35. These curves arise from an empirical introduction of damping into the phase shift η_l and are seen to improve qualitatively the agreement with experiment.

Ford and Wheeler conclude with reference to 48-Mev alpha-particle scattering by Pb that the rainbow angle is about 30°, the absorption is very strong for small impact parameters, and from the empirical adjustment of the gradual absorption curve in Fig. 35 that the transition from small to large absorption occurs over a range of angular momenta $\Delta l\simeq3$.

IX. CLASSICAL STRONG ABSORPTION MODEL

When the results of the 40-Mev angular distribution experiments were included in the apsidal distance plots

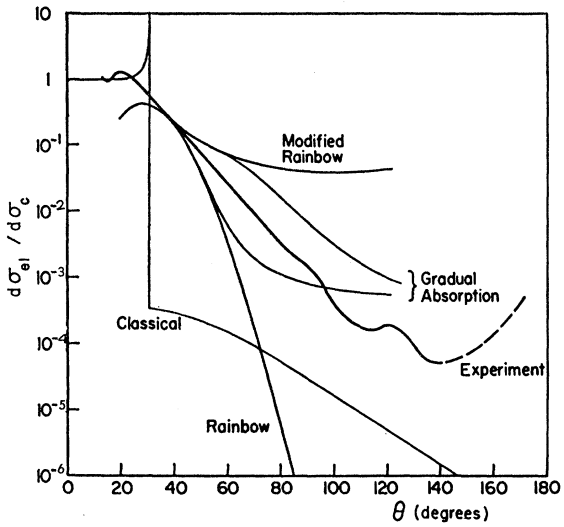

FIG. 35. Ratio of differential elastic scattering cross section to the Coulomb cross section, showing both the 48-Mev Pb experimental data and a number of theoretical curves. The classical curve based on the deflection function of Fig. 34 is shown. The simple quadratic approximation to the maximum in the curve of Fig. 34 leads to the rainbow curve while a better empirical fit to the curve of Fig. 34 leads to the modified rainbow curve. Two other curves obtained by introducing an empirical gradual absorption are also shown.

discussed in Sec. V, $d\sigma_{el}/d\sigma_c$ was found to depend approximately only on the classical apsidal distance D for all apsidal distances investigated. This is shown in Fig. 38. The data points in this figure were obtained from four separate experiments on the elastic scattering of alpha particles from Au: the energy dependence in the range 13 to 44 Mev of the cross section for scattering at 60° (12), the same for a scattering angle of 95° (12), the angular dependence in the range 20° to 60° of the cross section for scattering at 22 Mev (59), and the angular dependence in the range 21° to 100° of the cross section for scattering at 40 Mev (62). Plots of the various data for elastic alpha-particle scattering from Th, Pb, and Ta also show that $d\sigma_{el}/d\sigma_c$ depends approximately only upon the classical apsidal distance over the range investigated.

These results could not be easily understood on the basis of either the APB model or the Ford-Wheeler model. This situation motivated the proposal of a third

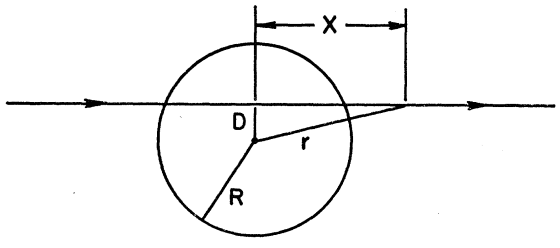

FIG. 36. Orbit geometry for a straight line orbit indicating the spherical interaction region of radius R, the apsidal distance D, and the orbit coordinates x and r.

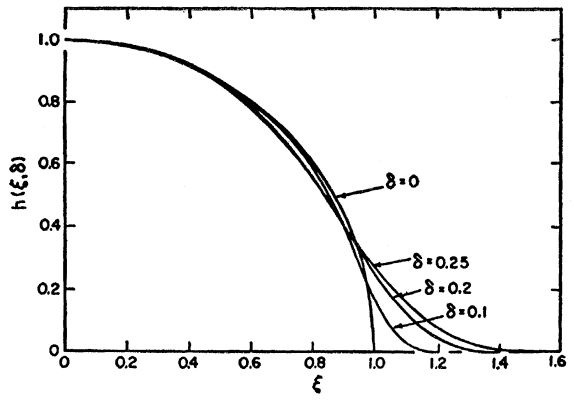

FIG. 37. The function $h(\xi,\delta)$ as a function of ξ for various values of δ.

model (43), in which it is assumed that absorption is the main feature that lowers the cross section from the Coulomb rule. This is expressed by writing the cross section as equal to the Coulomb cross section times a transmission factor T:

$$d\sigma_{el}/d\Omega=(d\sigma_c/d\Omega)T, \tag{133}$$

where T gives the fraction of the incident beam that emerges from the nucleus. T has the form

$$T=\exp\left(-\int\frac{dx}{l(x)}\right), \tag{134}$$

in which x is the coordinate of the alpha particle along its classical path and $l(x)$ is the mean free path as a function of position. A sketch of the path geometry is given in Fig. 36 in which a straightline path has been assumed. For this oversimplified straight-line-path model, it is rather easy to determine the exponent in Eq. (134):

$$\int\frac{dx}{l(x)}=2\int_{r=D}^{r=\infty}dr\frac{dx}{dr}\frac{1}{l(r)}, \tag{135}$$

where r is the radial coordinate of the orbit as shown in Fig. 36. An integration by parts yields

$$\int\frac{dx}{l(x)}=2\int_D^\infty drx(r)\frac{d}{dr}\left(\frac{-1}{l(r)}\right), \tag{136}$$

since

$$\begin{aligned} &x=0 \quad \text{for } r=D,\\ &(1/l)\to 0 \quad \text{for } r\to\infty. \end{aligned} \tag{137}$$

Now $l(r)$ is proportional to the reciprocal of the particle density ρ. Assuming the widely used form

$$\rho(r)=\rho_0\tfrac{1}{2}\{1-\tanh[(r-R)/d]\}, \tag{138}$$

where d is a measure of the thickness of the diffuse edge and R is the interaction radius, we have

$$l^{-1}=(l_0)^{-1}\tfrac{1}{2}\{1-\tanh[(r-R)/d]\}, \tag{139}$$

in which l_0 is the mean-free path near the center of the nucleus. For a sharp-edged interaction region,

$$\frac{d}{dr}\left(\frac{-1}{l(r)}\right)\underset{d\to 0}{\to}\frac{1}{l_0}\delta(r-R), \tag{140}$$

which supplies the motivation for the partial integration performed on (135).

For straight line paths (see Fig. 36),

$$x(r)=(r^2-D^2)^{\frac{1}{2}}, \tag{141}$$

so that (136) becomes (46)

$$\int\frac{dx}{l(x)}=\frac{R}{l_0\delta}\int_\xi^\infty dv(v^2-\xi^2)^{\frac{1}{2}}\operatorname{sech}^2\left(\frac{v-1}{\delta}\right),$$

$$\equiv(R/l_0\delta)h(\xi,\delta), \tag{142}$$

in which

$$\xi=D/R, \quad v=r/R, \quad \delta=d/R. \tag{143}$$

Here d is *twice* the value of the density fall-off distance, i.e.,

$$\rho(r)\underset{r\to\infty}{\to}\exp\left[-\frac{2(r-R)}{d}\right]. \tag{144}$$

Plots of the function $h(\xi,\delta)$ are shown in Fig. 37.

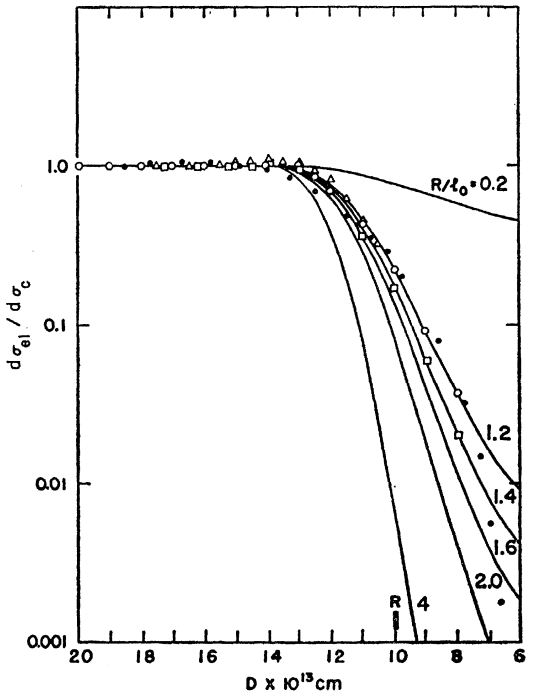

FIG. 38. Comparison of the classical strong absorption model calculations to the experimental data for Au. The ratio of the differential elastic scattering cross section to the Coulomb differential cross section is plotted against apsidal distance D. A number of theoretical curves are shown for various values of R/l_0. Experiment: $_{79}Au^{197}$— ●, 40 Mev (21°–100°), Brookhaven; △, 22 Mev (20°–160°), Indiana University; ○, 13–44 Mev (60°), University of Washington; □, of 13–44 Mev (95°), University of Washington. Theory: $R=R_{Au}+R_\alpha=10\times10^{-13}$ cm; $d=2\times10^{-13}$ cm.

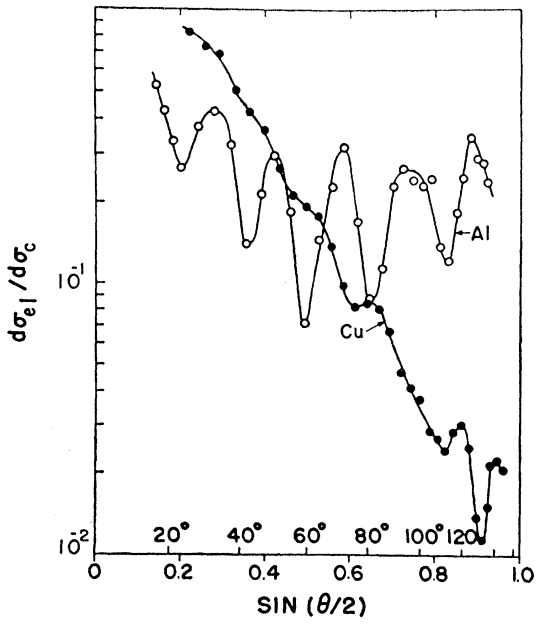

FIG. 39. Ratio of the differential scattering cross section to the Coulomb differential cross section for 19-Mev alpha particles incident on Al and Cu against $\sin(\theta/2)$. This shows the almost equal spacing of the maxima in the Al data when plotted against $\sin(\theta/2)$.

In Fig. 38 we reproduce a comparison of the theory to the experimental data on Au. The best-fit value of R/l_0 is roughly $R/l_0 \simeq 2$. This, together with the not-too-small diffuseness distance $d \simeq 2\times10^{-13}$ cm (the density fall-off distance is $\simeq 1\times10^{-13}$ cm), does not make an appealing set of parameters when compared to exact optical model results. Similar problems have arisen in heavy ion work in which, despite detailed numerical discrepancies, exact optical model phase shift comparison to path integrals similar to (142) indicates a qualitative correctness to the simple picture presented by this model (44). We explore this a little more fully in connection with the discussion of the exact optical model calculations for alpha particles. Until the semi-classical formulation of the optical model with absorption has been analyzed with a completeness comparable to the Ford-Wheeler discussion for a real potential, it will be difficult to assess the approximations inherent in (133).

X. SCATTERING FROM LIGHT ELEMENTS

The extension of these experiments to light elements was initiated by Bleuler and Tendam, at Purdue, who scattered 19-Mev alphas from Al and Cu; and also by Eisberg, Igo, and Wegner at Brookhaven, who investigated the scattering from Al to 40 Mev. The angular distributions for the scattering of alpha particles from light elements were found to show strong diffraction oscillations, in contrast to the essentially monotonic behavior of the heavy element angular distributions.

Figure 39 shows the data of Bleuler and Tendam (5). These data were measured using a NaI detector with an average angular resolution of $\pm3°$. The authors state that the indicated depth of the minima are probably more than their true values because of the poor angular resolution. The Al angular distribution of Eisberg, Igo, and Wegner (19), which was measured with an angular resolution of $\pm1°$, shows a more pronounced variation between maxima and minima (the measurements are not directly comparable since the energies are different). The 40-Mev Al angular distribution is presented in the composite plot of Fig. 43.

The angular distribution for the elastic scattering of 48-Mev alpha particles from Ag is also of an oscillatory nature. This was observed by Ellis and Schecter (11) at the Berkeley 60-in. cyclotron. They also found smooth angular distributions for the elastic scattering of alphas of the same energy from Au and Pb. In Fig. 40 the Ag data are presented.[3] Recently Yntema, Zeidman, and Raz (65) have measured angular distributions for the scattering of 43-Mev alpha particles scattered from Zn, Ag, Rh, and Au, and find oscillatory angular distributions in all cases except that of Au.

An intensive investigation of the scattering from light elements was performed at Brookhaven by Igo, Wegner, and Eisberg (30) who scattered 40-Mev alpha particles from C, Al, Ti, Cu, Nb, Mo, and Ag. Their experimental technique was similar to that used in the Brookhaven work on heavy elements, except for certain improvements. The detector used in the light element experiment consisted of a counter telescope which measured both the specific ionization and the energy of the detected particle. This provided a unique separation of alpha particles from other particles and also displayed the entire energy distribution of the detected alphas in one run. The detector had an energy resolution which

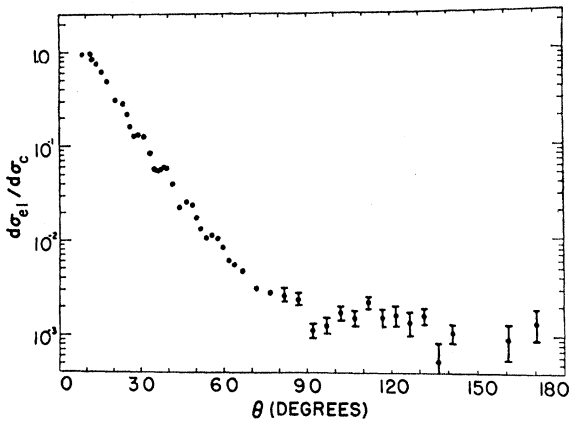

FIG. 40. Ratio of the differential scattering cross section to the Coulomb differential cross section for 48-Mev alpha particles incident on Ag. The oscillatory character is evident.

[3] Although it is not completely clear from the article by Ellis and Schecter, there is some question concerning the validity of their experimental technique for scattering angles in the backward hemisphere where the cross section is very small. The error, if present, would yield too large a cross section at large angles.

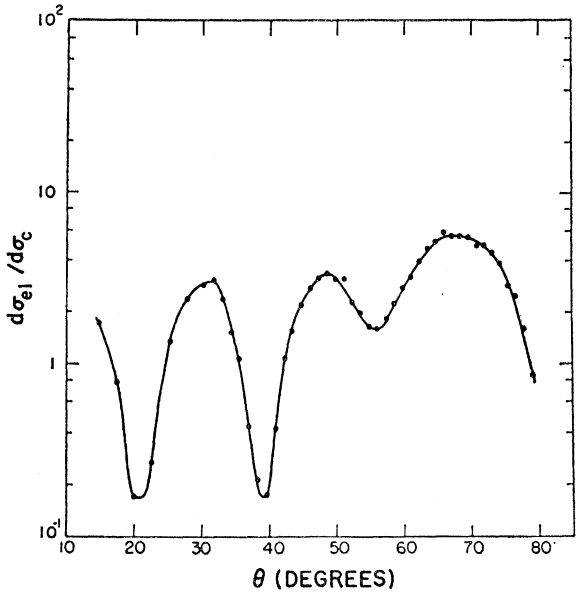

FIG. 41. Ratio of the differential scattering cross section to the Coulomb cross section for 40-Mev alpha particles incident on C. C(α,α)C.

was adequate to reject all inelastically scattered alpha particles, with the possible exception of a fraction of those inelastically scattered from the first excited state of Mo or Ag. Absolute cross sections were quoted to an accuracy of ±10%.[4] Measurements were made with an angular resolution of ±1.0°.

Some typical data are shown in Figs. 41 and 42, which give the angular distributions for the scattering of

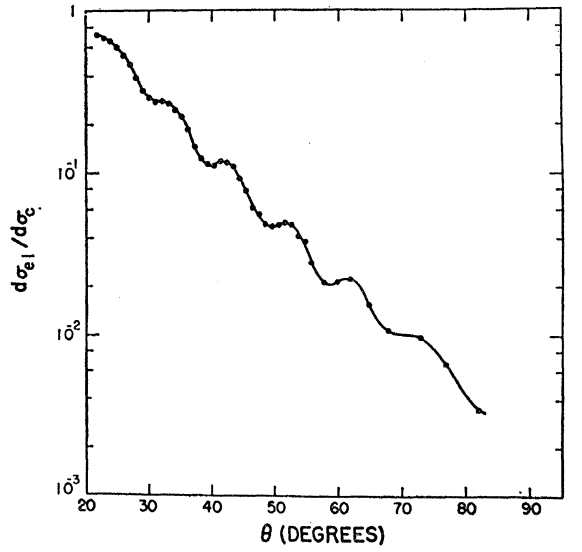

FIG. 42. Ratio of the differential scattering cross section to the Coulomb cross section for 40-Mev alpha particles incident on Ag. Ag(α,α)Ag.

[4] Checks made in the recent experiments of Yntema, Zeidman, and Raz indicate that the absolute values of $d\sigma_{el}/d\sigma_c$ measured by Igo, Wegner, and Eisberg might be low by as much as 20% (65).

40-Mev alpha particles from C and Ag. Figure 43 shows a composite plot of the 40-Mev data for the seven light elements investigated. Also included is the angular distribution for Ta which is typical of the heavy elements. The ordinate has been broken in order to display all the curves without overlapping.

Several features should be noted: (a) The oscillatory nature of the angular distributions slowly dies out in going from the light elements to the heavier elements; (b) the location of the strongest oscillations shifts from the small angles to the large angles; (c) the average

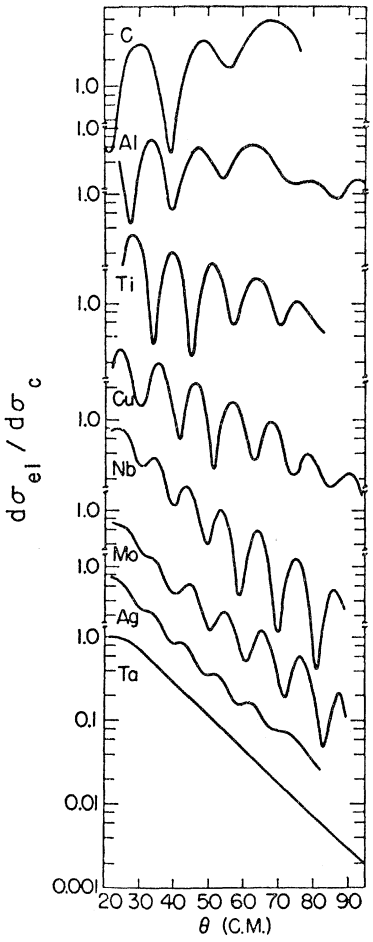

FIG. 43. Composite plot of the 40-Mev data on light elements along with those for one heavy element, Ta. The disappearance, as well as the increasing frequency of the oscillations in the differential cross section, along with the change from a positive mean slope to a negative mean slope as atomic number is increased, are easily noted.

slope of the angular distributions (i.e., of the ratio of the observed cross section to the Coulomb cross section) changes from positive to negative with increasing atomic weight; (d) the spacing of adjacent maxima gradually decreases with increasing atomic weight.

In connection with item (a), a similar effect occurs for a constant atomic weight on considering successively smaller alpha-particle energies. Figure 44 shows angular distributions for Ag measured at alpha-particle energies of 22, 40, and 48 Mev.

A large amount of data on elastic scattering of alpha particles from light elements now exists. Vaughn (55),

at the Berkeley 60-in. cyclotron, has measured angular distributions for the scattering of 48-Mev alpha particles from C and Mg. At the same laboratory, the angular distribution for elastic scattering of 48-Mev alpha particles from Be has been measured by Summers-Gill (52). At the University of Washington, Gugelot and Rickey (22) have investigated the angular distribution for the scattering from Mg of 42-Mev alphas. At M.I.T. angular distributions for the scattering of 31-Mev alpha particles have been measured by Watters (60) for Li, C, and Mg, and by Swenson, Schindewolf, and Wall (53) for Ni, Cu, and Au. All of these data are consistent with the general features described in the last paragraph. Kerlee, Blair, and Farwell (34) at the University of Washington have continued the measurements of the cross sections for elastic scattering at fixed angle as a function of the energy of the alpha particles. For

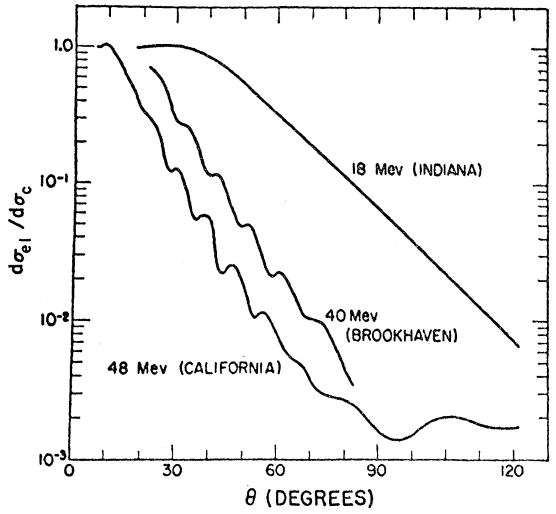

FIG. 44. Demonstration of features similar to those of Fig. 43 as the incident energy is decreased from 48 to 18 Mev for alpha particles incident on Ag.

the light elements, they find that $(d\sigma_{el}/d\Omega)(E)$ begins to exhibit oscillations. Figure 45 shows the cross section for the scattering of alpha particles at 60° from Al for energies between 15 and 40 Mev. In this case, which is the lightest element they investigated, the oscillations are very pronounced. Yavin and Farwell (63) measured the angular distributions for the scattering of 40-Mev alpha particles from C, N, O, and Ar. Also at Washington, Shook (51) has measured angular distributions for 43-Mev alpha particles scattered from C, Mg, and Ca. Angular distributions recently measured at Purdue are particularly interesting because the data extend to almost 180°. Seidlitz, Bleuler, and Tendam (50), using nuclear emulsions to detect the alpha particles, investigated the scattering of 18-Mev alphas from Ne and Ar; using the same technique, Corelli, Bleuler, and Tendam (7) studied the scattering at this energy of alpha particles from C, Mg, and Ca; using counters, Gailar,

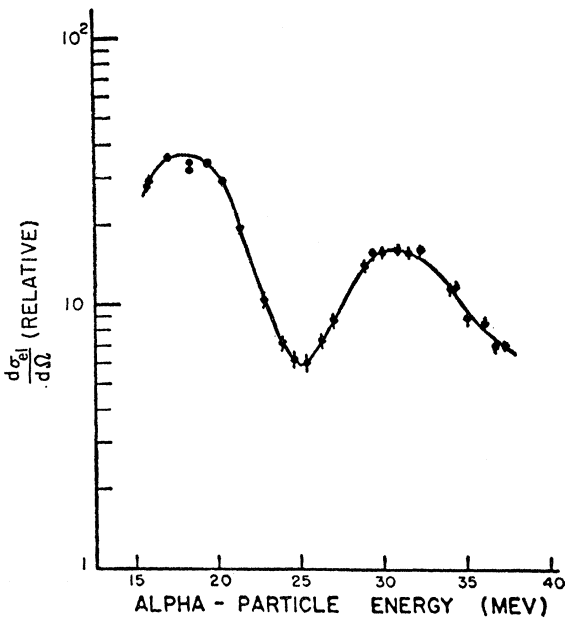

FIG. 45. Relative experimental differential cross section for Al at an angle of 60° as a function of alpha-particle energy.

Bleuler, and Tendam (16) have measured angular distributions for the scattering of 18.7-Mev alphas from Al, Cu, and Ag. Figures 46 and 47 show data for Ne and Cu at 18 and 18.7 Mev. At Saclay, Beurtey, Catillon, Chaminode, Fraggi, Papineau, and Thirion (66) have made measurements on the scattering of 44-Mev alpha

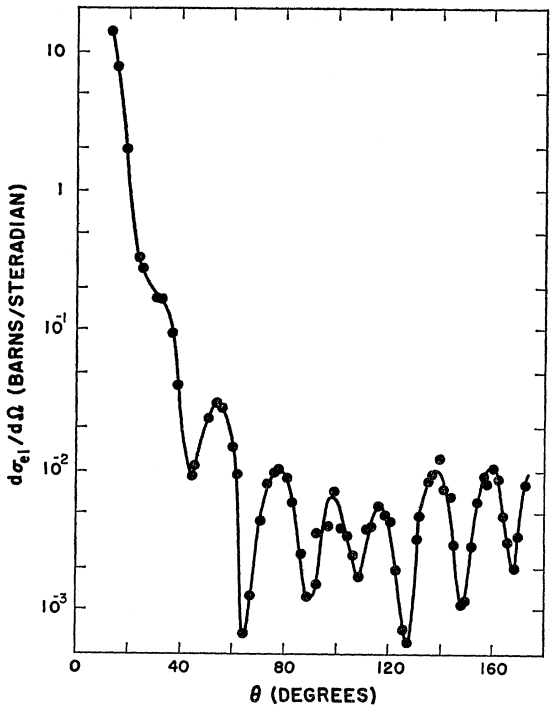

FIG. 46. Differential cross section against scattering angle for 18-Mev alpha particles incident on Ne.

particles from Zn. Fulbright, Lassen, and Poulsen (15) at Copenhagen have used an ionization chamber to measure with quite good energy resolution the scattering angular distributions for 20-Mev alphas incident on C, O, Mg, Al, Ni, Cu, Zn, Ag, In, Au, Pb, and Bi. At Tokyo, Hu, Kato, Oda, and Takeda (29) made measurements of the scattering of 22-Mev alpha particles from C, Mg, and Si. And finally (as of August,

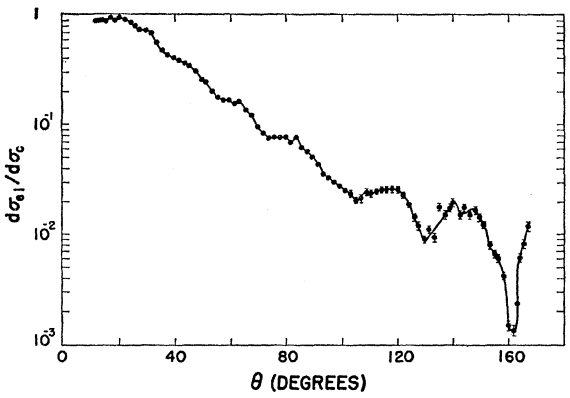

FIG. 47. Ratio of the differential cross section to the Coulomb cross section for 18.7-Mev alpha particles incident on Cu.

1960) Van Heerden and Prowse at Birmingham have measured the angular distribution for the scattering of 38-Mev alpha particles from C and from I (57).

XI. "SIMPLE" DIFFRACTION ANALYSIS

The first attempt to analyze the light element elastic scattering involved fitting the spacings between adjacent maxima in the oscillatory distributions using a formula

$$2kR\Delta[\sin(\theta/2)]=\pi, \tag{145}$$

in which k is the wave number as usual, R is the "wiggle" radius, and $\Delta[\sin(\theta/2)]$ is the difference in $\sin(\theta/2)$ between the values corresponding to adjacent maxima of the diffraction pattern.

In the measurements of the scattering of 19-Mev alpha particles from Al (5) and 40-Mev alpha particles from Al (19, p. 1606), it was found that to within experimental error, $\Delta[\sin(\theta/2)]$ is in fact constant for a large number of adjacent sets of maxima in the cross section for a particular energy and element. In these measurements, the values obtained were, for Al, $R\simeq 2.0A^{\frac{1}{3}}\times 10^{-13}$ cm for 19-Mev alpha particles and $1.8A^{\frac{1}{3}}\times 10^{-13}$ cm for 40-Mev alpha particles. The rather large numerical values can be reduced somewhat by considering the finite size of the alpha particle arising from both "intrinsic" size and the de Broglie wavelength. These values for R have reasonable magnitudes and exhibit a reasonable energy dependence.

Equation (145) can be developed by considering scattering of waves from a black disk. The scattering amplitude is

$$f(\theta)=\frac{\lambda\!\!\!^{-}}{2i}\sum_{l=0}^{\infty}(2l+1)(e^{2i\eta l}-1)P_l(\cos\theta). \tag{146}$$

The "black disk" approximation (neglecting Coulomb scattering) is obtained by arguing that $e^{2i\eta l}$ is zero in the shadow region behind the disk ($l\leqslant kR$) and 1 in the bright region. Thus (146) can be written

$$f(\theta)\simeq-\frac{\lambda\!\!\!^{-}}{2i}\sum_{l=0}^{kR}(2l+1)P_l(\cos\theta). \tag{147}$$

To obtain an approximation for small angles, $P_l(\cos\theta)$ is replaced by the small-angle Bessel function approximation. This gives for $f(\theta)$

$$f(\theta)\simeq-\frac{\lambda\!\!\!^{-}}{2i}\int_{l=0}^{kR}dl(2l+1)J_0[(l+\tfrac{1}{2})\theta]. \tag{148}$$

This becomes

$$\begin{aligned} f(\theta)&\simeq\frac{i\lambda\!\!\!^{-}}{\theta^2}\int_0^{(kR+\frac{1}{2})\theta}dz\frac{d}{dz}[zJ_1(z)],\\ &\simeq\frac{i\lambda\!\!\!^{-}}{\theta^2}[(kR+\tfrac{1}{2})\theta]J_1[(kR+\tfrac{1}{2})\theta]. \end{aligned} \tag{149}$$

For large $R/\lambda\!\!\!^{-}$, this is

$$f(\theta)\simeq iR[J_1(kR\theta)/\theta]. \tag{150}$$

This yields for the differential cross section

$$(d\sigma_{el}/d\Omega)(\theta)\simeq R^2[J_1^2(kR\theta)/\theta^2]. \tag{151}$$

The standard uncertainty in treatment of diffraction theory approximations leads alternatively to (151) with θ replaced by $2\sin(\theta/2)$, i.e., we could have derived (151) in a "reasonable" way (taking

$$P_l(\cos\theta)\simeq J_0[(2l+1)\sin(\theta/2)]$$

instead of $J_0[(l+\frac{1}{2})\theta]$) to yield

$$d\sigma_{el}/d\Omega\simeq R^2\{J_1^2[2kR\sin(\theta/2)]/4\sin^2(\theta/2)\}. \tag{152}$$

The spacing between adjacent peaks is approximately π so that from (152) the result of (145) is obtained directly.

This general approach was taken one step further by Gugelot and Rickey (22) who fitted 42-Mev Mg data with the Born approximation for a real, attractive square well. The significance of this is not clear in the light of what has been learned since that time by optical model computations.

XII. OPTICAL MODEL ANALYSIS

Exact numerical fitting of the parameters of a complex potential model to the alpha-particle elastic scattering data has been carried out in some detail at Los Alamos Scientific Laboratory (31–33). The specific

form of the model involves an electrical potential arising from the charge distribution of the target nucleus assuming the alpha particle to be a point charge (however, recent computations for heavy ion scattering have indicated that introducing the finite size of the charge distribution of both incident and target particles into the model can make an appreciable change in the numerical results) (23), and in addition a complex nuclear potential. The electrical potential is derived from a charge distribution which has been used in fitting electron scattering data (27) and is expressed as

$$V_{\text{coul}}=\begin{cases}\dfrac{Z_1Z_2e^2}{r_0}\left\{\dfrac{\dfrac{1}{n^2}+\dfrac{1}{2}-\dfrac{x^2}{6}+\dfrac{e^{-n}}{n^2}\left(\dfrac{1-e^{-nx}}{nx}+\dfrac{e^{nx}}{2}\right)}{\dfrac{1}{3}+\dfrac{2}{n^2}+\dfrac{e^{-n}}{n^3}}\right\}, & x\leqslant 1\\[2ex] \dfrac{Z_1Z_2e^2}{r_0}\left\{\dfrac{1}{x}-\dfrac{e^{n-nx}\left(\dfrac{1}{x}+\dfrac{n}{2}\right)}{e^{-n}+2n+\dfrac{n^3}{3}}\right\}, & x\geqslant 1,\end{cases} \tag{153}$$

in which $x=r/r_0$ with r_0 interpreted as the radius of the charge distribution and r_0/n as the distance in which the charge distribution drops off at the nuclear surface. The parameters are chosen to be $r_0=1.30A^{\frac{1}{3}}\times10^{-13}$ cm for the heavy elements and $r_0=1.22A^{\frac{1}{3}}\times10^{-13}$cm for the light elements. These are somewhat larger than the electron scattering results (64) with the view that such a choice may compensate partly for the finite size of the alpha particle. The computations are insensitive to the choice of n; however, the explicit value used by Igo and Thaler is not given in their paper (31).

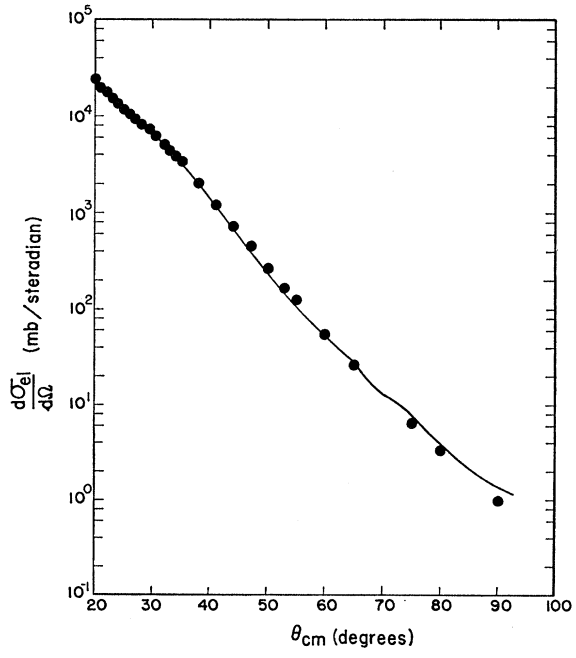

FIG. 48. Experimental differential cross section for 40.2-Mev alpha particles incident on Th (points) along with a solid curve computed using an optical model, $V=50$ Mev; $W=7.5$ Mev. This is an example of the typical fit that can be obtained for a heavy element using an optical model.

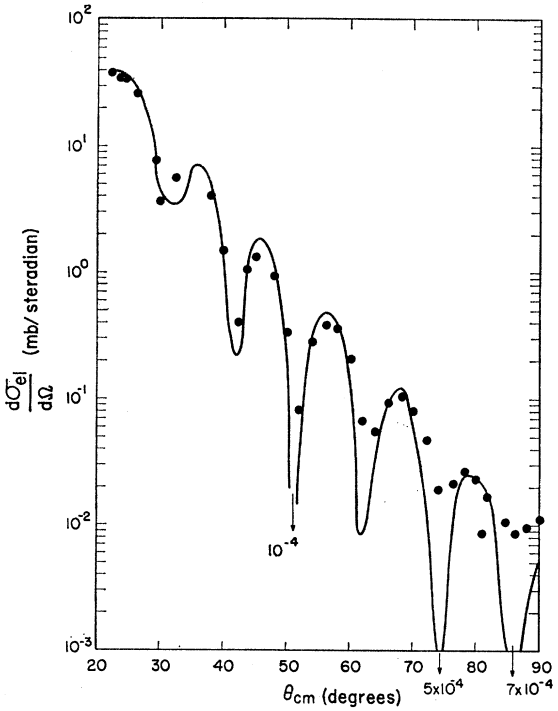

FIG. 49. Experimental differential cross section for 40.2-Mev alpha particles incident on Cu (points) along with a solid curve computed using an optical model. $V=49.5$ Mev; $W=11$ Mev. This is an example of a typical fit for a relatively light element.

The nuclear potential used in the fitting is taken to be

$$V_{\text{nuc}}=-\frac{V+iW}{1+\exp[(r-R)/d]}, \tag{154}$$

in which R is the nuclear potential radius and d is the familiar diffuseness distance.

With these potentials, a numerical integration of the radial Schrödinger equation was carried out for as many as 30 partial waves, yielding the relevant scattering amplitude which is squared to give the differential cross section:

$$\frac{d\sigma_{\text{el}}}{d\Omega}=\lambda^2\left|\frac{-n\exp\{in\log[\sin^2(\theta/2)]\}}{\sin^2(\theta/2)}+\frac{1}{2i}\sum_{l=0}^{\infty}(2l+1)e^{2i(\sigma_l-\sigma_0)}(e^{2i\eta_l}-1)P_l(\cos\theta)\right|^2, \tag{155}$$

where as usual

$$n=Z_1Z_2e^2/\hbar v, \quad \sigma_l=\arg\Gamma(l+1+in). \tag{156}$$

Although there is no total cross section for charged

particles, the compound formation cross section is given in terms of the phase shifts as

$$\sigma_c=\pi\lambda^2\sum_{l=0}^{\infty}(2l+1)(1-|e^{2i\eta l}|^2). \tag{157}$$

Typical of the results achieved in fitting heavy element data are the 40.2-Mev Th data, shown in Fig. 48. This fit is the result of an incomplete exploration of the space of the four nuclear parameters R, d, V, and W. [Details of the exploration are given by Igo and Thaler (31).] The parameters R and d were not varied widely. The resulting parameters are

$$\begin{aligned}&R=9.6\times10^{-13}\text{ cm}=(1.35A^{\frac{1}{3}}+1.3)\times10^{-13}\text{ cm},\\&d=0.5\times10^{-13}\text{ cm},\\&V=50\text{ Mev},\\&W=7.5\text{ Mev}.\end{aligned} \tag{158}$$

A typical result of similar fitting for light element data (Cu) is shown in Fig. 49 for Cu at 40.2 Mev. The resulting parameters are

$$\begin{aligned}&R=6.7\times10^{-13}\text{ cm}=(1.35A^{\frac{1}{3}}+1.3)\times10^{-13}\text{ cm},\\&d=0.5\times10^{-13}\text{ cm},\\&V=49.5\text{ Mev},\\&W=11\text{ Mev}.\end{aligned} \tag{159}$$

After similarly fitting the entire set of 40-Mev data (the elements Cu, Nb, Mo, Ag, Ta, Au, Pb, and Th), Igo and Thaler conclude that the best values of the parameters are

$$\begin{aligned}&R=(1.35A^{\frac{1}{3}}+1.3)\times10^{-13}\text{ cm},\\&d=0.5\times10^{-13}\text{ cm},\\&V=45_{-7}{}^{+6}\text{ Mev},\\&W=10_{-3.5}{}^{+1.5}\text{ Mev}.\end{aligned} \tag{160}$$

The three lightest elements studied (C, Al, and Ti) required $V=30$ Mev. Igo and Thaler suggest that the explanation of this discrepancy may be the known charge shape function (14), at least for C which has a Gaussian rather than an exponential tail [the latter arises from (154)]. It may also be that V is energy dependent enough that the center-of-mass correction is

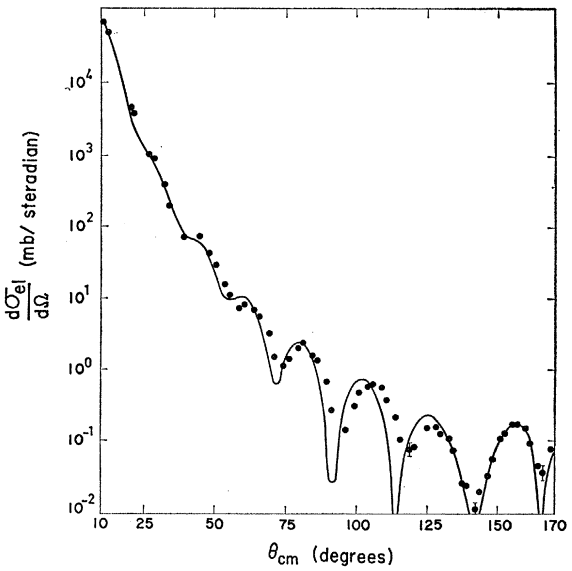

FIG. 50. Experimental differential cross section for 18-Mev alpha particles incident on Ar (points) along with a curve computed as a result of a detailed optical model analysis: $R=(1.17A^{\frac{1}{3}}+1.36)\times10^{-13}$ cm; $d=0.6\times10^{-13}$ cm; $V=100$ Mev; $W=15$ Mev.

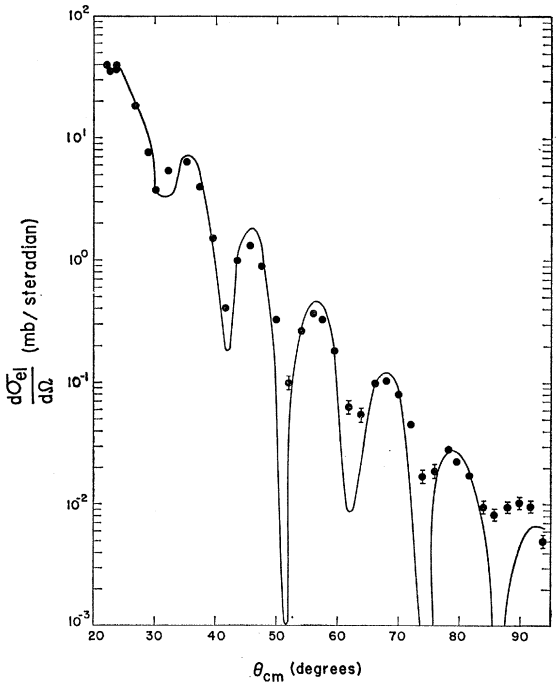

FIG. 51. Experimental differential cross section for 40-Mev alpha particles incident on Cu (points) along with a curve computed as a result of a detailed optical model analysis: $R=(1.14A^{\frac{1}{3}}+2.24)\times10^{-13}$ cm; $d=0.5\times10^{-13}$ cm; $V=49.3$ Mev; $W=11$ Mev.

TABLE II.

E, Mev	Element	V, Mev	W, Mev
40.2	C	30	10
40.2	Al	30	12
40.2	Ti	30	14
40.2	Cu	46.8	13
40.2	Nb	45	13.5
40.2	Mo	42	9.5
40.2	Ag	37	10
40.2	Ta	51	9
40.2	Au	44	10
40.2	Pb	43	7.6
40.2	Th	50	7.5
20	Ag	35	7.5
20	Au	30	9.5
20	Pb	30	16

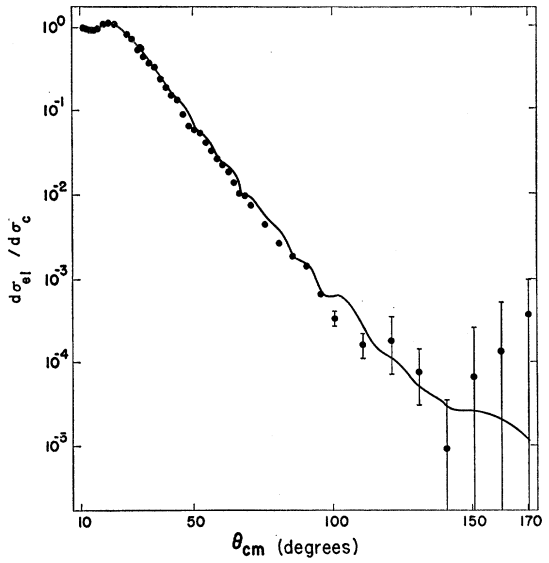

FIG. 52. Ratio of the experimental differential cross section to the Coulomb cross section for 48-Mev alpha particles incident on Pb (points) along with a curve computed as a result of a detailed optical model analysis: $R=(1.13A^{\frac{1}{3}}+2.00)\times10^{-13}$ cm; $d=0.6\times10^{-13}$ cm; $V=25$ Mev; $W=15$ Mev.

significant for light nuclei. The results (Table II) of fitting the 20-Mev data give some basis for this statement, since V is consistently lower at that energy.

In Table II, the detailed listing of the best parameters (V and W) for each element is given to indicate the extent to which the values spread from the over-all conclusion of (160).

After completing the search for best-fit values of V and W with only minor variations in R and d, Igo made

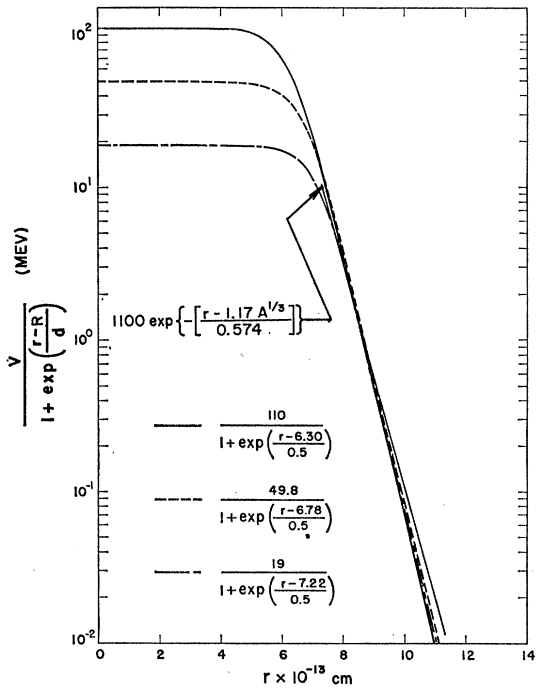

FIG. 54. The real parts of the best-fit optical model potentials for Cu at 40 Mev as a function of r as indicated in the figure. A tail-only potential is plotted where the fitting is unambiguous.

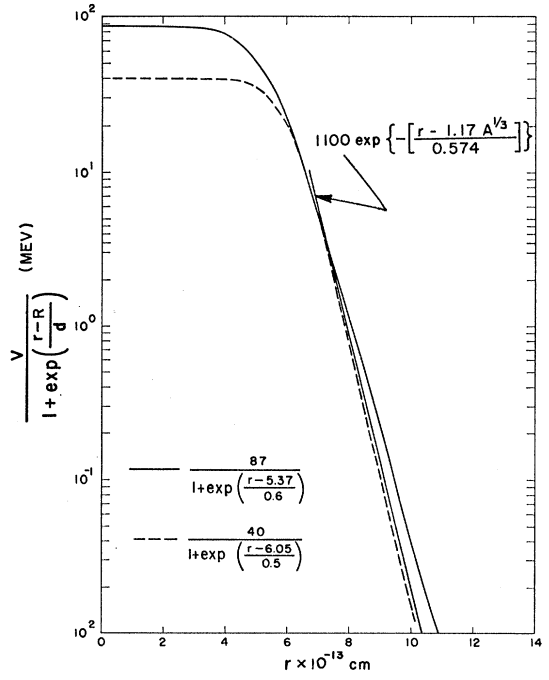

FIG. 53. The real parts of the best-fit optical model potentials for Ar at 18 Mev as a function of r as indicated in the figure. A tail-only potential is plotted where the fitting is unambiguous.

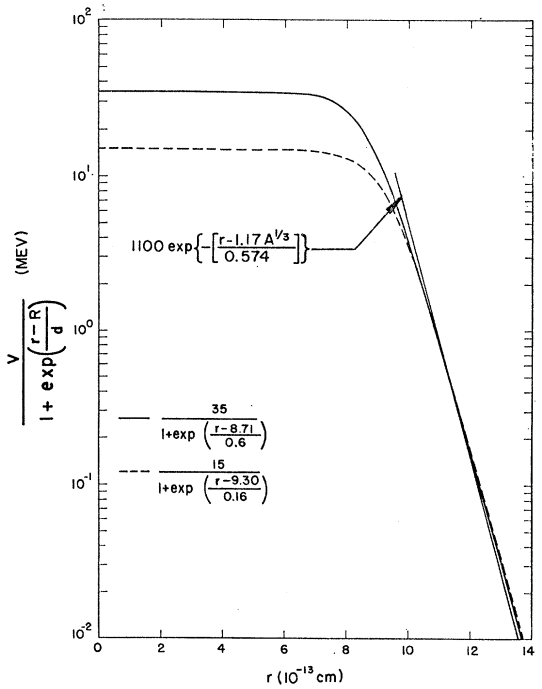

FIG. 55. The real parts of the best-fit optical model potentials for Pb at 48 Mev as a function of r. A tail-only potential is plotted where the fitting is unambiguous.

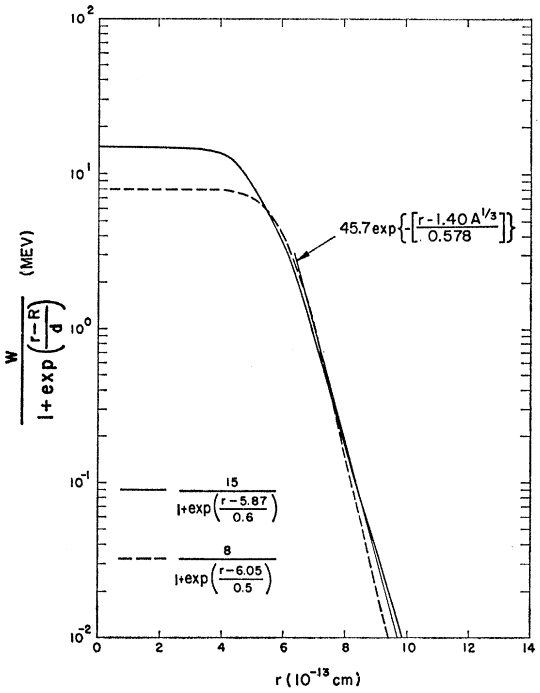

FIG. 56. The imaginary parts of the best-fit optical model potentials for Ar at 18 Mev as a function of r. A tail-only potential is plotted where the fitting is unambiguous.

more careful and complete studies of a few selected elements (33). These studies were motivated, at least in part, by the view that the best-fit parameter values resulting from extensive variation of R and d as well as

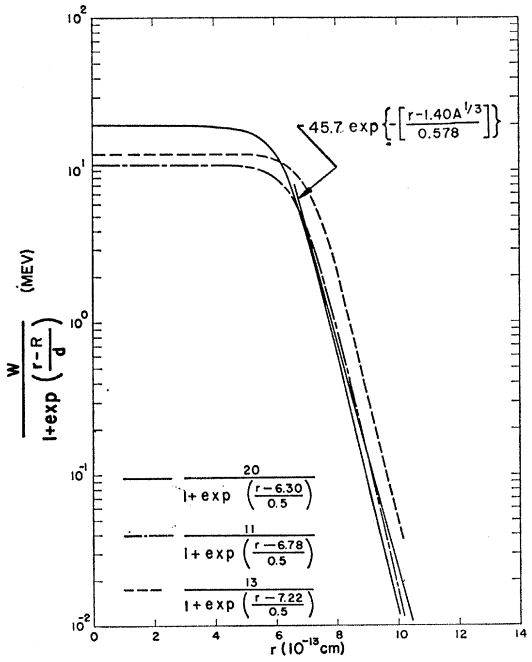

FIG. 57. The imaginary parts of the best-fit optical model potentials for Cu at 40 Mev as a function of r. A tail-only potential is plotted where the fitting is unambiguous.

V and W would lead to a nonuniqueness of fit (6). Not only was this conjecture confirmed, but Igo was able to show that, essentially because of the strong absorption occurring for orbits in the nuclear interior, the alpha particle, to use a Wheelerism, can only "taste" the features of the nuclear surface and not explore in any detail the interior region beyond indicating a very strong interaction.

Igo's detailed studies were confined to the elements elements Ar, Cu, and Pb. The best fits for these data [argon: (50); copper: (30); lead: (11)] are shown in Figs. 50–52. Figures 53–55 show the real parts of equivalent best fit potentials along with part of the curve

$$1100 \exp[-(r-1.17A^{\frac{1}{3}})/0.574] \text{ Mev},$$

which is found to represent the common features of these equivalent fits out in the tail region. Thus the

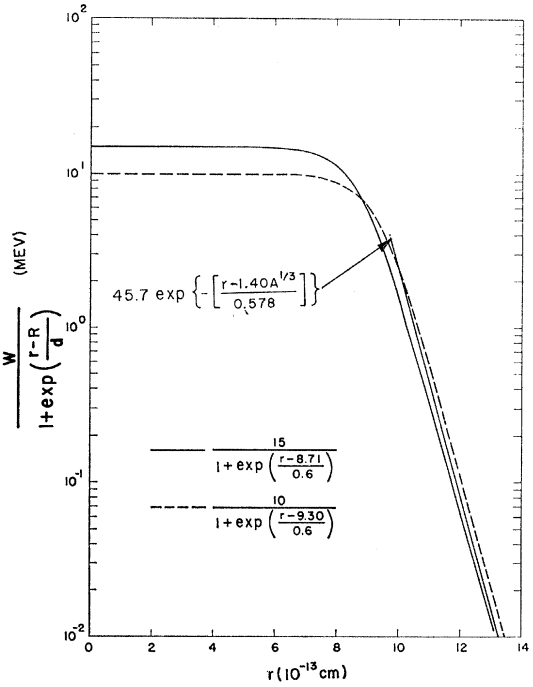

FIG. 58. The imaginary parts of the best-fit optical model potentials for Pb at 48 Mev as a function of r. A tail-only potential is plotted where the fitting is unambiguous.

conclusion drawn from this analysis is that only the tail region is of consequence in determining the scattering under conditions of strong absorption.

It is natural to ask whether the imaginary part of the optical potential can be similarly determined only in the tail. The empirical answer to this is yes, as indicated in Figs. 56–58. In addition to the equivalent best-fit potentials, part of the curve

$$45.7 \exp[-(r-1.40A^{\frac{1}{3}})/0.578] \text{ Mev}$$

is plotted in the figures. The Cu fits (both the real and the imaginary part of theoretical potential) show more

exception than either Ar or Pb. This can be attributed to the poorer character of the angular distribution fits to Cu in general, so that it is not necessary to weight the Cu results as heavily as those for Ar and Pb. Igo thus concludes that the effective complex nuclear potential for alpha particles in the region where the

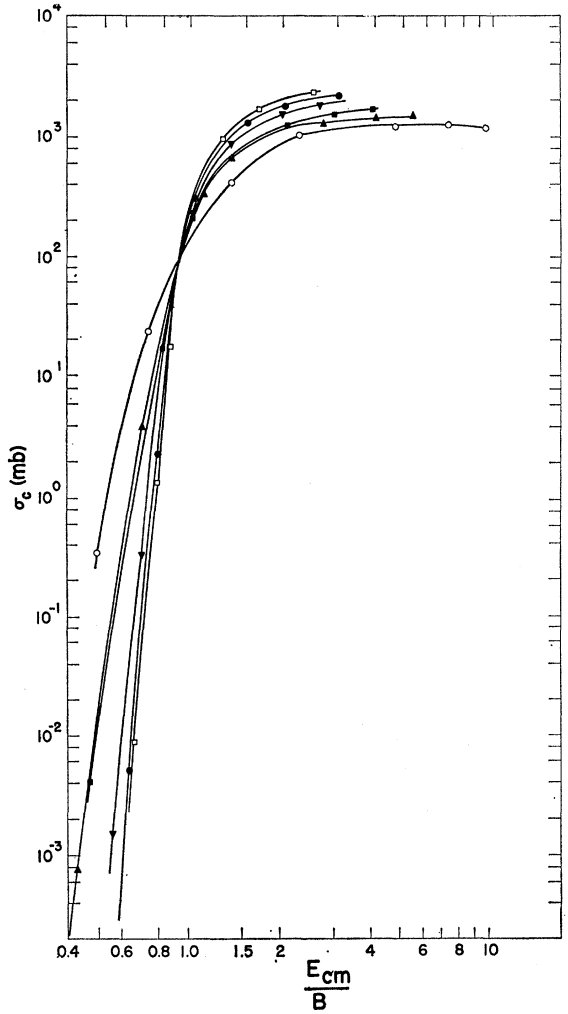

FIG. 59. Compound formation cross section σ_c (or equivalently the reaction cross section σ_r since compound elastic scattering is presumably negligible over most of the energy range shown) as a function of the energy of the incident alpha particle in the center-of-mass system, divided by the barrier energy as obtained according to Fig. 60 for various values of nuclear charge Z. ○, $Z=10$; ▲, $Z=20$; ■, $Z=30$; ▼, $Z=50$; ●, $Z=70$; □, $Z=90$.

magnitude of the real part is less than 10 Mev is given by

$$-1100\exp[-(r-1.17A^{\frac{1}{3}})/0.574]$$
$$-i\,45.7\exp-[(r-1.40A^{\frac{1}{3}})/0.578]\ \text{Mev}$$

with r in units of 10^{-13} cm. Poor fits to the experimental data show marked deviation from this form in the tail, thus indicating a certain sensitivity of the measurements.

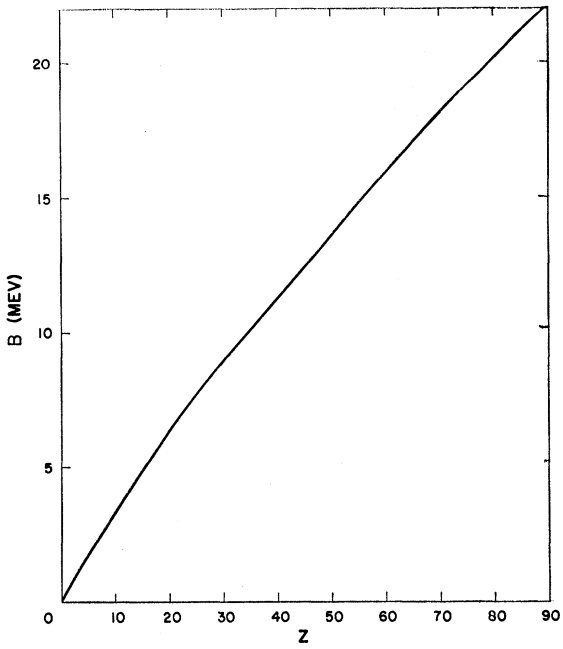

FIG. 60. Barrier height B as a function of nuclear charge Z.

Using this potential (actually *one* of the equivalent potentials is used), it is possible to compute the cross section for compound formation, σ_c. Results of such a calculation are shown in Fig. 59, plotted against the ratio of the center of mass kinetic energy $E_{c.m.}$ to the barrier height B for various values of the atomic number Z of the target nucleus. A plot of the barrier height B against Z is shown in Fig. 60. These calculations of σ_c can be checked against measured excitation functions. Figure 61 shows such a comparison for a

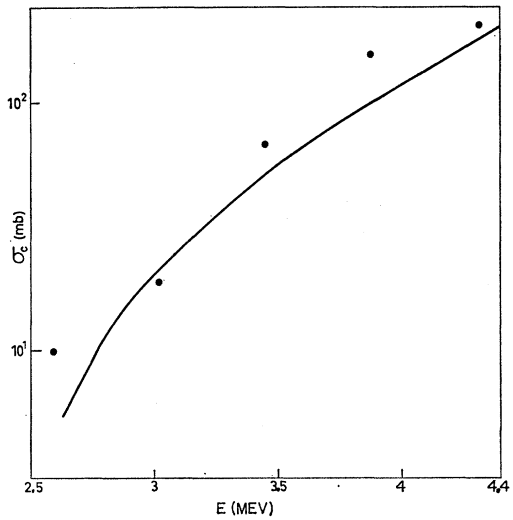

FIG. 61. Comparison of the (α,n) reaction cross section of Mg with the appropriate computed curve for σ_c from Fig. 59. Igo argues that the (α,n) reaction makes up most of σ_c in this energy range. The potential resulting from fitting the elastic scattering data leads also to good agreement for the reaction data.

light element, Mg^{25}, using data (25) from the (α,n) reaction. Typical heavy element results are shown in Fig. 62. The data are shown for the

$$(\alpha,f)+\sum_{i=1}^{5}(\alpha,in)+\sum_{i=0}^{3}(\alpha,pin)$$

excitation function on U^{233}, the

$$(\alpha,f)+\sum_{i=1}^{5}(\alpha,in)+(\alpha,p)+(\alpha,p2n)$$

excitation function on U^{235}, and the

$$(\alpha,f)+\sum_{i=1}^{3}(\alpha,pin)+(\alpha,\alpha n)$$

excitation function on U^{238} (56). The fits are clearly very adequate.

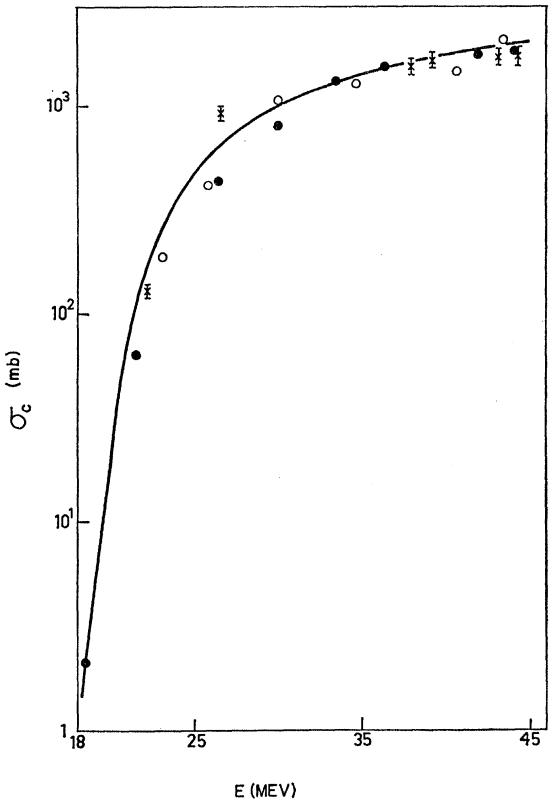

FIG. 62. Comparison of U excitation function data with the computed curve for σ_c from Fig. 59, providing an example of a typical fit for a heavy element, using a potential derived from analysis of elastic scattering data. ○, U^{233}; ●, U^{235}; ×, U^{238}.

In order to make contact with work on α decay, Igo uses the plots shown in Fig. 63. Curves a and b are the form factor for the charge distribution of uranium as measured by electron scattering (the vertical scale of curve b is expanded) (26). Curve c is the Coulomb

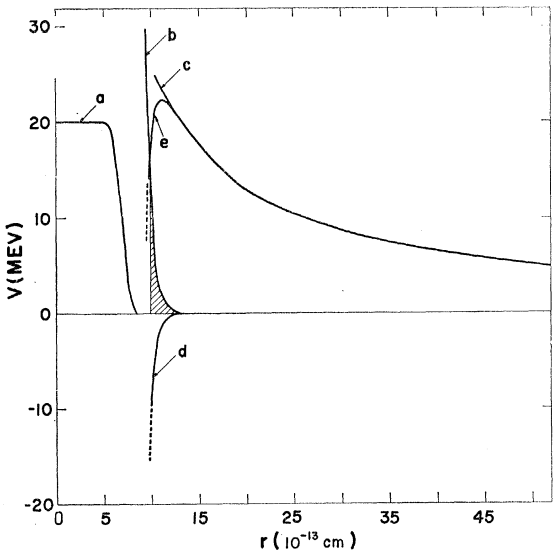

FIG. 63. Nuclear charge density (curves a and b—the latter expanded) of U obtained in electron scattering experiments along with the Coulomb potential curve (curve c) and the nuclear potential tail (curve d) as well as the nuclear plus Coulomb potential (curve e) in the tail region.

potential for $Z=92$, and curves d and e (expanded scale) are the real part of the alpha-particle nuclear potential. Igo's analysis indicates that elastically scattered alpha particles do not probe the potentials significantly beyond the distance corresponding to the nuclear potential equal in magnitude to 10 Mev. The part of the charge distribution outside of this distance is shaded in Fig. 63. If the neutron distribution is roughly similar to the proton distribution, then this shaded region is an indication of the extent of the surface region which is significant in the alpha particle

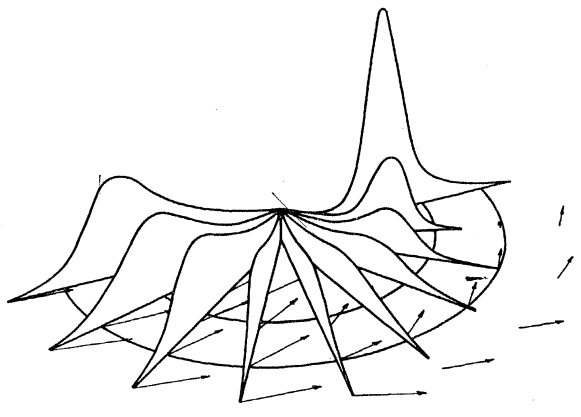

FIG. 64. Perspective spatial plot of the alpha particle current vector $\mathbf{j}$ (the arrow-lengths are proportional to $\log|\mathbf{j}|$) and its divergence $\nabla\cdot\mathbf{j}$ in one azimuthal plane (all azimuthal planes are equivalent since there is no spin-orbit coupling) for 18-Mev alpha particles incident on Ar. Parameters correspond to a best fit of Figs. 53 and 56 (the dashed curve). The two semicircular curves indicate the 90% and 10% strength positions for the real part of the potential. A spherical lens effect is indicated in the large peak in $\nabla\cdot\mathbf{j}$ near the focal point.

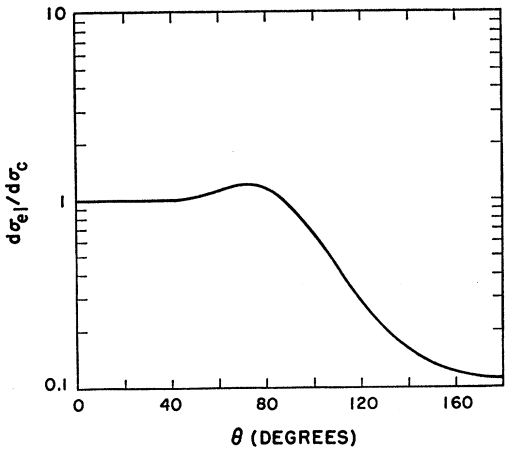

FIG. 65. Ratio of the differential scattering cross section to the point charge Coulomb scattering cross section in the absence of a nuclear potential. $V=W=0$.

elastic scattering interaction. The probability of finding two neutrons and two protons in this region is about 0.02%. Igo argues that alpha clusters formed very far inside of this region would dissolve before emerging from the Coulomb barrier.

Although only the surface region is effective in returning alpha particles to the elastic channel, this does *not* mean that they do not penetrate into the interior. In Fig. 64, a perspective plot of the alpha-particle current **j** and its divergence $\nabla\cdot\mathbf{j}$ is shown in one azimuthal plane (the plots are the same for all azimuthal angles since the scattering is cylindrically symmetric) [(35, p. 24); for similar calculations for protons see (10) and (36)]. The parameters correspond to 18-Mev alpha particles on argon with $R=6.05\times10^{-13}$ cm, $d=0.5\times10^{-13}$ cm, $V=40$ Mev, and $W=8$ Mev.

The arrows showing the current vector **j** are on a logarithmic scale, and two semicircles indicating the 90% and 10% nuclear potential levels are also shown

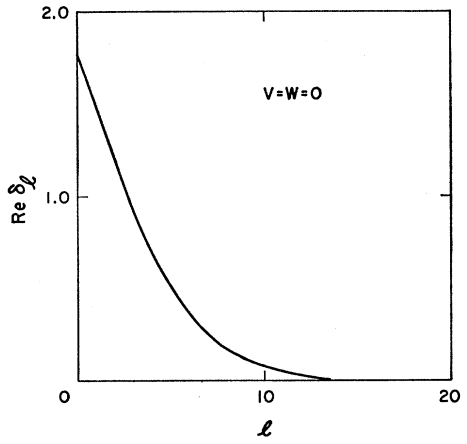

FIG. 66. Real part of the "nuclear" (total minus *point* Coulomb) phase shift as a function of angular momentum for the potential used in Fig. 65. $V=W=0$.

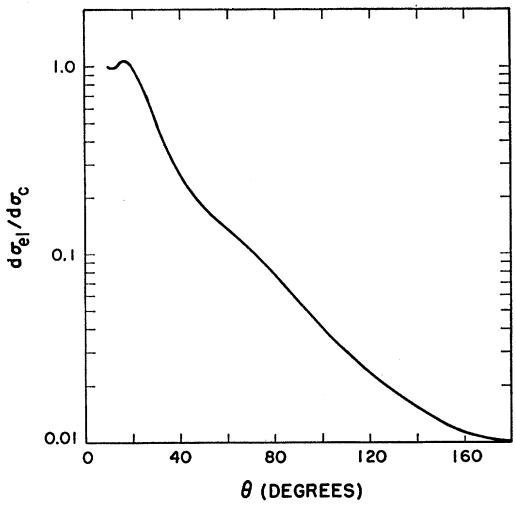

FIG. 67. A typical angular distribution (ratio to Coulomb) for a potential with a large imaginary part. The back scattering drops only two orders of magnitude, indicating that the imaginary part causes considerable back reflection. $V=0$; $W=200$ Mev; $d=0.5\times10^{-13}$ cm.

(i.e., the surface region for the potential). The beam is incident from the left leading to a focal region (large $\nabla\cdot j$) on the right. Perhaps the most important point here is that there is a significant fraction (probably around 50%) of the divergence of the current within the 90% semicircle. Thus, in the empirical view, the alpha particles do get into the internal region although

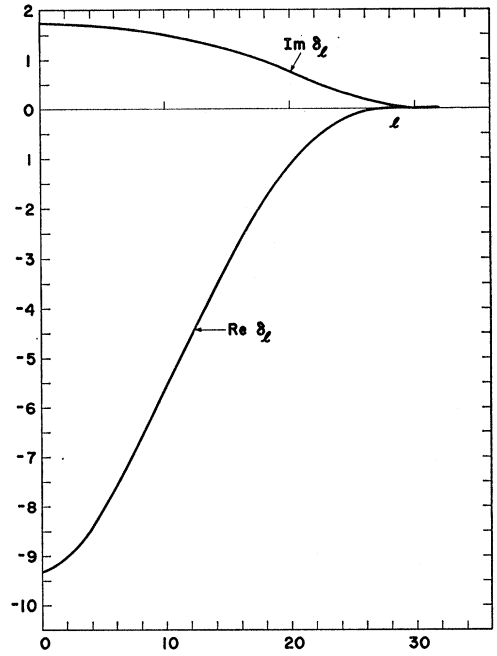

FIG. 68. Real and imaginary parts of the nuclear phase shift δ_l as a function of angular momentum l for the potential used in Fig. 67. The large negative value of Re δ_l indicates the repulsive behavior introduced by the absorption. $V=0$; $W=200$ Mev; $d=0.5\times10^{-13}$ cm.

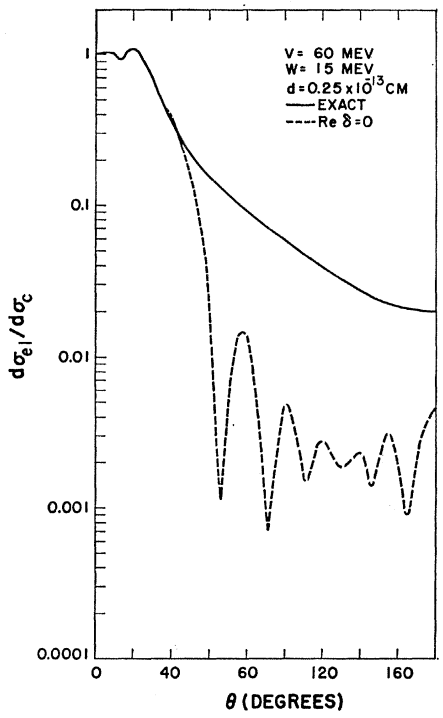

FIG. 69. Comparison of an angular distribution computed with $\mathrm{Re}\,\delta_l=0$ to an exact computation for a rather sharp surface ($d=0.25\times10^{-13}$ cm). The "approximate" ($\mathrm{Re}\,\delta=0$) calculation lies *below* the exact calculation in contrast to the back scattering features in the APB model. $V=60$ Mev; $W=15$ Mev; ———, exact; — — —, $\mathrm{Re}\,\delta=0$.

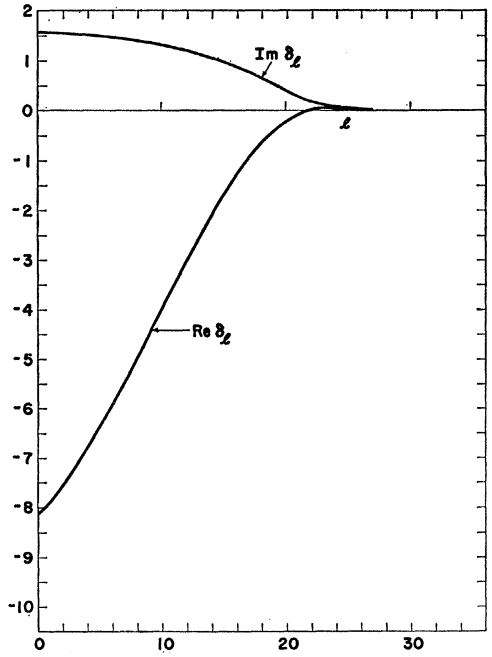

FIG. 70. Real and imaginary parts of the phase shift as a function of angular momentum corresponding to the exact calculation of Fig. 69. $V=60$ Mev; $W=15$ Mev; $d=0.25\times10^{-13}$ cm.

the strong absorption apparently rules out their elastic emission. Perhaps the proper phrasing is to say that the observed *elastically* scattered particles only "taste" the surface, but that a large fraction of the incident beam gets into the interior and is absorbed there, leading to other channels.

In order to explore more completely some of the qualitative features in the optical model computations,

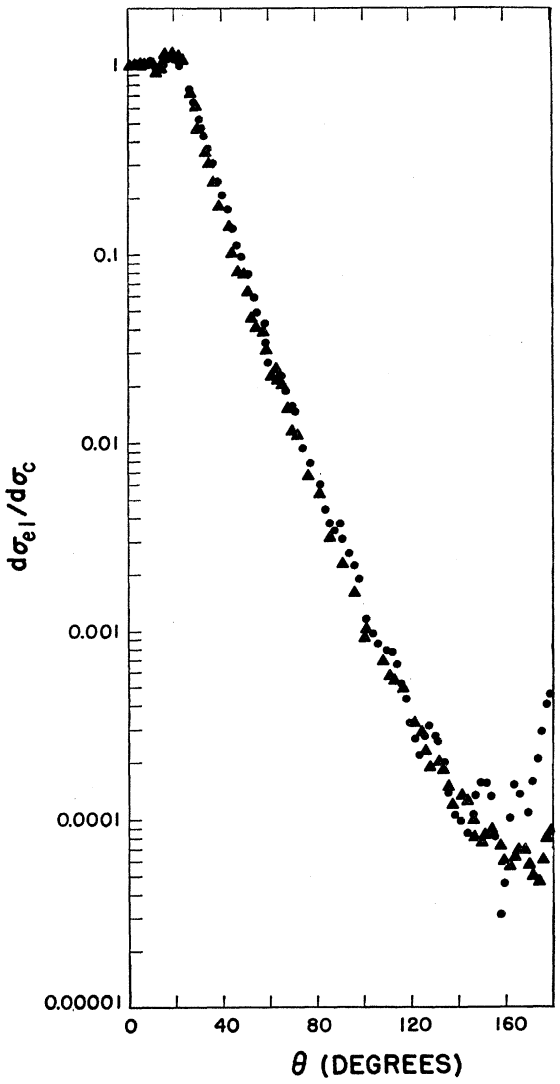

FIG. 71. Plots analogous to those in Fig. 79 for a "realistic" surface ($d=0.5\times10^{-13}$ cm). $V=60$ Mev; $W=15$ Mev; $d=0.5\times10^{-13}$ cm; ▲, exact; ●, $\mathrm{Re}\,\delta=0$.

we present a number of selected graphs. Most of them are nominally for alpha-particle scattering from Pb at an energy of 48 Mev. The parameters are a radius of $1.125A^{\frac{1}{3}}\times10^{-13}$ cm and a surface diffuseness parameter $n=9$. The radius of the nuclear potential distribution is specified as $(1.125A^{\frac{1}{3}}+2.63)\times10^{-13}$ cm.

The effect of the finite size of the charge distribution

is shown in Fig. 65, where the differential cross section divided by the point charge Coulomb cross section for zero nuclear potential ($V=W=0$) is plotted. The effect of the finite size alone is sufficient to depress the back scattering by an order of magnitude. In Fig. 66, the real part of the "nuclear" phase shift (total phase shift minus point charge Coulomb phase shift) is shown under the same conditions. With no nuclear potential, the monotonic character of the phase shift (and hence of the classical deflection function) leads to a uniform approach of the quantum mechanical differential cross section to the corresponding classical differential cross section.

The effect of a large imaginary part for the nuclear potential is shown in Figs. 67 and 68 which present curves analogous to those of Figs. 65 and 66 for $V=0$, $W=200$ Mev, and $d=0.5\times10^{-13}$ cm. The main feature here is the strong "repulsion" introduced by a large W. This is evident both in the not-too-small back scattering and in the negative values for the real part of the nuclear phase shift at small angular momenta.

A sequence of pairs of figures shows the result of setting the real part of the nuclear phase shift equal to zero. The first pair, Figs. 69 and 70, is based on the parameter choice $V=60$ Mev, $W=15$ Mev, and $d=0.25\times10^{-13}$ cm. Here Re $\delta_l=0$ is not a good approximation below a tenth of the point charge Coulomb cross section. In heavy ion scattering (44), for which Re $\delta_l=0$ was found to be a relatively good approximation, the ratio-to-Mott-scattering does not drop below 10%.

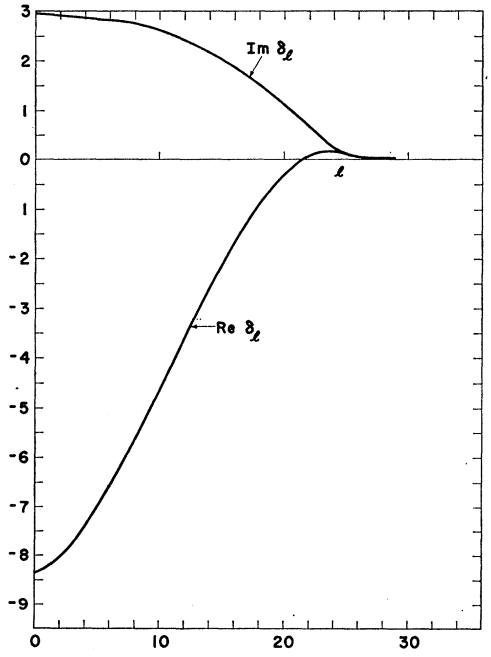

FIG. 72. Real and imaginary parts of the nuclear phase shift as a function of angular momentum, corresponding to the exact calculation of Fig. 71. $V=60$ Mev; $W=15$ Mev; $d=0.5\times10^{-13}$ cm.

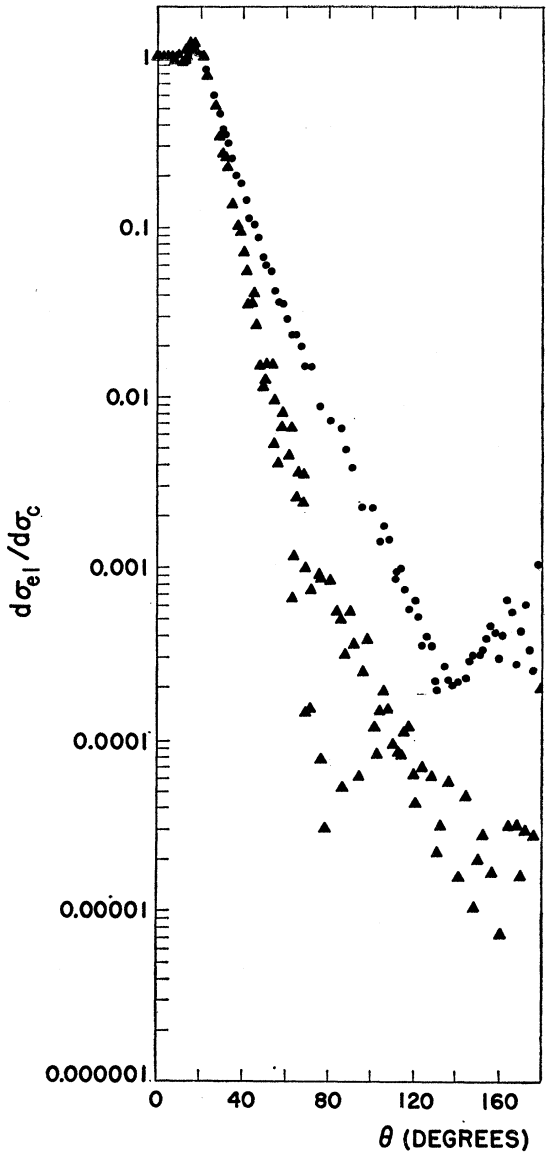

FIG. 73. Plots analogous to those in Figs. 69 and 71 for a diffuse surface ($d=0.75\times10^{-13}$ cm); the tuning effect of surface thickness has here thrown the exact calculations *below* the approximate ones. $V=60$ Mev; $W=15$ Mev; ▲, exact; ●, Re $\delta=0$.

Figures 71 and 72 show results analogous to those of Figs. 69 and 70, but with $d=0.5\times10^{-13}$ cm. In this case Re $\delta_l=0$ is a much better approximation, indicating that the surface diffuseness parameter d has a tuning effect on Re δ_l.

Figures 73 and 74 contain similar results for $d=0.75\times10^{-13}$ cm. The points for Re $\delta_l=0$ still drop almost four orders of magnitude, indicating that if the nuclear potential surface is not too sharp, setting the real part of the nuclear phase shift equal to zero is a fairly good approximation. This lends support to the extreme concept of a classical strong absorption model as opposed to the extreme nonabsorptive rainbow scattering analysis.

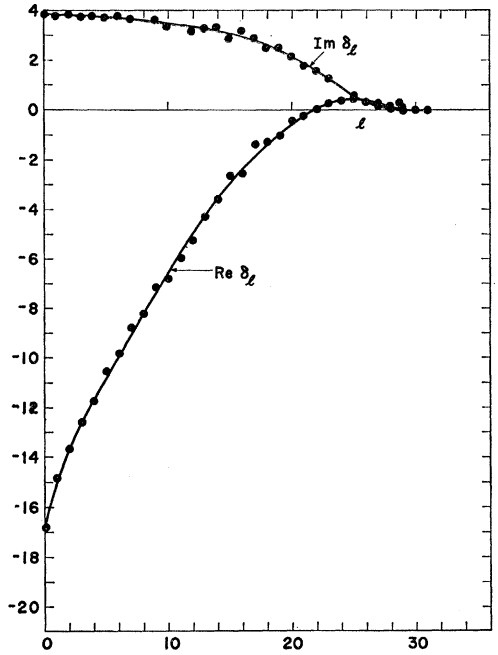

FIG. 74. Real and imaginary parts of the nuclear phase shift as a function of angular momentum, corresponding to exact calculation of Fig. 73. Computed points are indicated explicitly to show the larger fluctuation encountered. There may be some uncertainty in the plot of Re δ_l since the machine computations gave phase shifts only in the range $(-\pi, \pi)$ and the proper addition of multiples of π was made by educated guessing. $V=60$ Mev; $W=15$ Mev; $d=0.75\times10^{-13}$ cm.

To underline a little the tuning effect of the diffuseness distance d even on Im δ_l, Figs. 75 and 76 show Im δ_l as a function of d for first two low angular momenta and secondly two high angular momenta. The nonmonotonic variation for low angular momenta emphasizes this tuning feature.

To further clarify this point, Figs. 77 and 78 show curves for Im δ_l calculated classically for a straight line path (43) (Fig. 77) with parameters adjusted for Pb at 48 Mev and also for a Coulomb orbit intersecting the same density distribution (44) (Fig. 78). The mean free path at the center of the target nucleus is taken to be $l_0=1\times10^{-13}$ cm for both figures, and curves for $d=0$ and 0.5×10^{-13} cm are shown. The distance d as stated here is one-half the corresponding distance used in the references (43, 44) so that the density for *these two figures* falls off as $\exp[-(r-R)/d]$ similar to the nuclear potentials used for Pb at 48 Mev. There is very little variation of Im δ_l as a function of d for small angular momenta indicating that this variation in the quantum-mechanical calculations is probably not a classical effect.

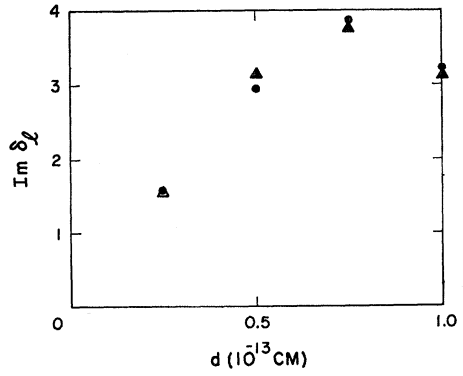

FIG. 75. Imaginary part Im δ_l of the nuclear phase shift as a function of surface diffuseness distance d for two small angular momenta. $V=60$ Mev; $W=15$ Mev; ▲, $l=0$; ●, $l=1$.

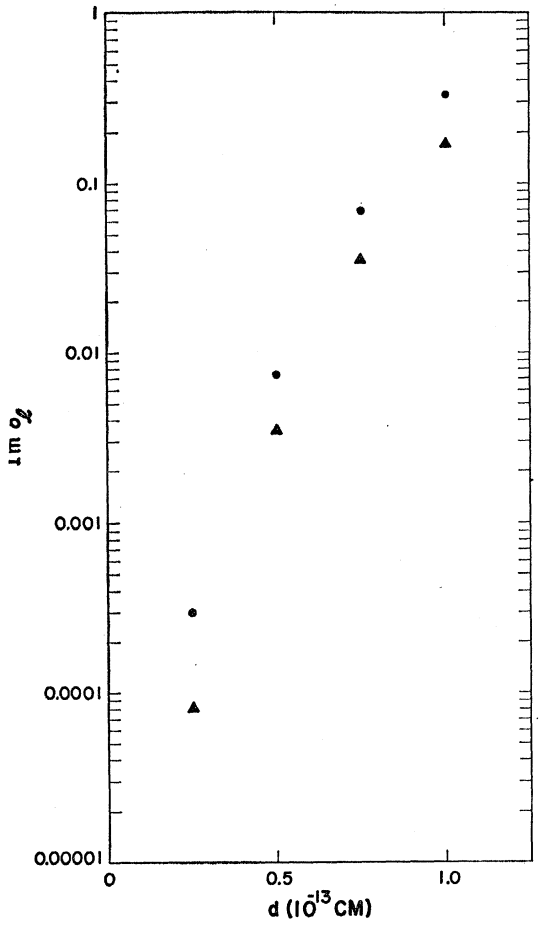

FIG. 76. Plot analogous to Fig. 75 for two large angular momenta. $V=60$ Mev; $W=15$ Mev; ●, $l=28$; ▲, $l=29$.

XIII. CONCLUSIONS

Probably the major conclusion from the work on alpha-particle scattering has been the realization that entrance channel alpha-particle measurements primarily give information about the interaction near the nuclear surface, and the qualitative fact that the alpha particle absorption in the nuclear interior must be strong.

The inability to learn about the nuclear interior for alpha particle scattering may seem at first to be disap-

pointing; however, the existence of strong absorption in the interior tends to minimize the role of the interior in processes involving alpha particles in entrance channel phenomena. It may be, however, that exit channel processes will provide more information about the interior.

With respect to information concerning the presently available models for the scattering process, the most salient feature is the relevance of the optical model. This is closely related to the success of the smoothed APB model although the latter model does not parametrize in terms of potentials. Because of the great importance of absorption, the semiclassical no-absorption approximation is not pertinent to the alpha-particle scattering problem without absorption modification. Although the classical strong absorption viewpoint leads to parameters which seem somewhat unrealistic, the qualitative correctness of the approximation has been born out by further analysis.

There is a marked similarity between alpha particle and heavy ion scattering.

There is room for further experimental work in alpha particle-nucleus interactions. Very little data exist on total reaction cross sections, although these are very helpful in optical model analyses, for example. There is little information available at present concerning energy dependence of the interaction parameters. For this reason any attempt to link high-energy alpha-particle scattering parameters and low-energy alpha decay is still somewhat premature.

On the theoretical side, semiclassical approximation in the presence of strong absorption has so far been understood only roughly; much more work remains to be done here. There is also room for further clarification of the connection between alpha-particle and heavy ion scattering.

ACKNOWLEDGMENTS

One of the authors (R.M.E.) would like to express his appreciation to the Cavendish Laboratory, Cambridge, England, for hospitality and support during an early stage of the writing of this article. The other author (C.E.P.) would like to acknowledge the hospitality and technical assistance of people at the Åbo Academy, and the University of Turku, Turku, Finland, Los Alamos Scientific Laboratory, and the University of Minnesota. Both of us have benefited from numerous conversations with many of our colleagues.

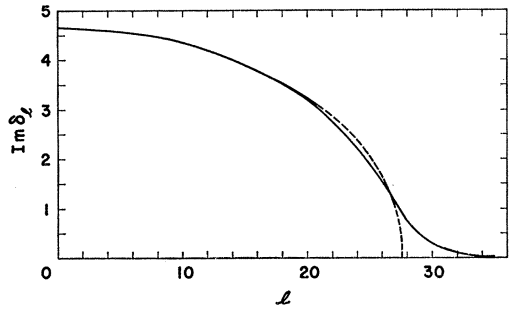

FIG. 77. Im δ_l calculated classically for a straight line orbit intersecting a Saxon density form, as a function of angular momentum. $l_0=1\times10^{-13}$ cm; — — —, $d=0$; ———, $d=0.5\times10^{-13}$ cm.

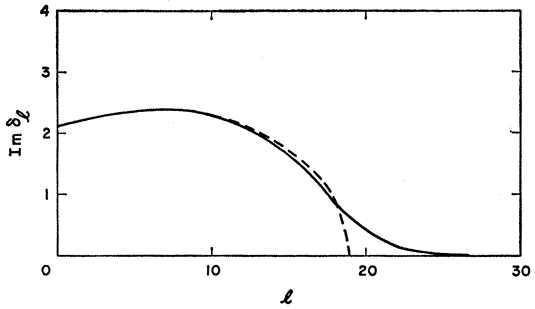

FIG. 78. Plot analogous to that of Fig. 77 for a Coulomb orbit intersecting a Saxon density form. $l_0=1\times10^{-13}$ cm; — — —, $d=0$; ———, $d=0.5\times10^{-13}$ cm.

BIBLIOGRAPHY

1. A. Akhieser and I. Pomeranchuk, J. Phys. (U.S.S.R.) **9**, 471 (1945).
2. E. S. Bieler, Proc. Roy. Soc. (London) **A105**, 434 (1924).
3. J. M. Blatt and V. F. Weisskopf, *Theoretical Nuclear Physics* (John Wiley & Sons, Inc., New York, 1952).
4. J. S. Blair, Phys. Rev. **95**, 1218 (1954).
5. E. Bleuler and D. J. Tendam, Phys. Rev. **99**, 1605 (1955).
6. W. B. Cheston and A. E. Glassgold, Phys. Rev. **106**, 1215 (1957).
7. J. C. Corelli, E. Bleuler, and D. J. Tendam, Phys. Rev. **116**, 1184 (1959).
8. G. Darwin, Phil. Mag. **27**, 499 (1914).
9. R. M. Eisberg, G. Igo, and H. E. Wegner, Phys. Rev. **99**, 1606 (1955).
10. R. M. Eisberg, I. E. McCarthy, and R. A. Spurrier, Nuclear Phys. **10**, 591 (1959).
11. R. E. Ellis and L. Schecter, Phys. Rev. **101**, 636 (1956).
12. G. Farwell and H. E. Wegner, Phys. Rev. **95**, 1212 (1954).
13. K. W. Ford and J. A. Wheeler, Ann. Phys. **7**, 259 (1959).
14. J. H. Fregau, Phys. Rev. **104**, 225 (1956).
15. H. W. Fulbright, N. O. Lassen, and N. O. R. Poulsen, Kgl. Danske Videnskab. Selskab, Mat. fys. Medd. **31**, No. 10 (1959).
16. O. H. Gailar, E. Bleuler, and D. J. Tendam, Phys. Rev. **112**, 1989 (1958).
17. H. Geiger and E. Marsden, Proc. Roy. Soc. (London) **A82**, 495 (1909).
18. H. Geiger and E. Marsden, Phil. Mag. **25**, 604 (1913).
19. H. Goldstein, *Classical Mechanics* (Addison-Wesley Publishing Company, Inc., Reading, Massachusetts, 1950).
20. H. E. Gove, Phys. Rev. **99**, 1353 (1955).
21. K. R. Greider and A. E. Glassgold, Ann. Phys. **10**, 100 (1960).
22. P. C. Gugelot and M. Rickey, Phys. Rev. **101**, 1613 (1956).
23. M. Gursky (private communication, 1960).
24. W. Hardmeier, Physik. Z. **27**, 574 (1926).
25. I. Halpern, Phys. Rev. **76**, 248 (1949).
26. B. Hahn, D. G. Ravenhall, and R. Hofstadter, Phys. Rev. **101**, 1131 (1956).
27. D. L. Hill and K. W. Ford, Phys. Rev. **94**, 1617 (1954).
28. E. W. Hobson, *The Theory of Spherical and Ellipsoidal Harmonics* (Cambridge University Press, New York, 1931).
29. C. Hu, S. Kato, Y. Oda, and M. Takeda, J. Phys. Soc. Japan **14**, 549 (1959).
30. G. Igo, H. E. Wegner, and R. M. Eisberg, Phys. Rev. **101**, 1508 (1956).
31. G. Igo and R. M. Thaler, Phys. Rev. **106**, 126 (1957).
32. G. Igo, Phys. Rev. Letters **1**, 72 (1958).

33. G. Igo, Phys. Rev. **115**, 1665 (1959).
34. D. D. Kerlee, J. S. Blair, and G. W. Farwell, Phys. Rev. **107**, 1343 (1957).
35. I. E. McCarthy, *Proceedings of the International Conference on the Nuclear Optical Model* (Florida State University Press, Florida State University, Tallahassee, Florida, 1959).
36. I. E. McCarthy, Nuclear Phys. **10**, 583 (1959).
37. J. A. McIntyre, K. H. Wang, and L. C. Becker, Phys. Rev. **117**, 1337 (1960).
38. M. A. Melkanoff, S. A. Moszkowski, J. S. Nodvik, and D. S. Saxon, Phys. Rev. **101**, 507 (1956).
39. N. F. Mott and H. S. W. Massey, *The Theory of Atomic Collisons* (Clarendon Press, Oxford, England, 1950).
40. P. M. Morse and H. Feshbach, *Methods of Theoretical Physics* (McGraw-Hill Book Company, Inc., New York, 1953).
41. G. Placzek and H. Bethe, Phys. Rev. **57**, 1075(A) (1940).
42. E. Pollard, Phys. Rev. **47**, 611 (1935).
43. C. E. Porter, Phys. Rev. **99**, 1400 (1955).
44. C. E. Porter, Phys. Rev. **112**, 1722 (1958).
45. J. R. Rees and M. B. Sampson, Phys. Rev. **108**, 1289 (1958).
46. B. A. Robson, Proc. Phys. Soc. (London) **71**, 126 (1958).
47. E. Rutherford, Phil. Mag. **21**, 669 (1911).
48. E. Rutherford, Phil. Mag. **37**, 537 (1919).
49. E. Rutherford and J. Chadwick, Phil. Mag. **4**, 605 (1927).
50. L. Seidlitz, E. Bleuler, and D. J. Tendam, Phys. Rev. **110**, 682 (1958).
51. G. B. Shook, Phys. Rev. **114**, 310 (1959).
52. R. Summers-Gill, Phys. Rev. **109**, 1591 (1958).
53. L. W. Swenson, U. Schindewolf, and N. S. Wall, Nuclear Phys. **6**, 203 (1958).
54. J. J. Thomson, Proc. Cambridge Phil. Soc. **15**, 465 (1910).
55. F. Vaughn, UCRL-3174 (1955) (unpublished).
56. R. Vandenbosch, T. D. Thomas, S. E. Vandenbosch, R. A. Glass, and G. T. Seaborg, Phys. Rev. **111**, 1358 (1958).
57. I. J. Van Heerden and D. J. Prowse, Nuclear Phys. **15**, 356 (1960).
58. G. N. Watson, *A Treatise on the Theory of Bessel Functions* (Cambridge University Press, New York, 1948).
59. N. S. Wall, J. R. Rees, and K. W. Ford, Phys. Rev. **97**, 726 (1955).
60. H. J. Watters, Phys. Rev. **103**, 1763 (1956).
61. H. E. Wegner, Brookhaven Natl. Lab. Rept. BNL 331, (1955) (unpublished).
62. H. E. Wegner, R. M. Eisberg, and G. Igo, Phys. Rev. **99**, 825 (1955).
63. A. I. Yavin and G. W. Farwell, Nuclear Phys. **12**, 1 (1959).
64. D. R. Yennie, D. G. Ravenhall, and R. N. Wilson, Phys. Rev. **95**, 500 (1954).
65. J. L. Yntema, B. Zeidman, and B. J. Raz, Phys. Rev. **117**, 801 (1960).
66. R. Beurtey, P. Catillon, R. Chaminade, H. Faraggi, A. Papineau, and J. Thirion, Compt. rend. **249**, 2189 (1959).